ENGINEERING PERSPECTIVE

CONTENTS

ENGINEERING PERSPECTIVE

An International Journal

ENGINEERING PERSPECTIVE

Research Paper

Advanced Frequency of Thick FGM Spherical Shells with Fully Homogeneous Equation by Using TSDT and Nonlinear Varied Shear Coefficient

Chih-Chiang Hong [1,*] iD

[1] *Department of Mechanical Engineering, Hsiuping University of Science and Technology, Taichung, 412-406, Taiwan*

ABSTRACT

The natural frequency values of free vibrations are generally dependent on properties of materials, boundary conditions, displacement types, vibration matter with respect to axes direction, environment temperature and shear correction in thick composited shells. Advanced natural frequency investigation of thick functionally graded material (FGM) spherical shells is presented by considering the advanced shear correction coefficient. When the more thicker shells are used, it is more necessary to consider the transverse shear effect on the vibrations. It is novel to consider the effects of nonlinear coefficient in third-order shear deformation theory (TSDT) on the advanced shear correction coefficient. The nonlinear coefficient term of TSDT is included the fully homogeneous equation according to the homogeneous matrix under free vibration. The numerical solution can be solved for the five degree polynomial equation derived from zero determinant of the fully coefficient matrix by using the numerical method, then the natural frequency can be obtained. Three effects of nonlinear coefficient term, environment temperature and power law index on the frequency of thick FGM spherical shells with advanced shear correction coefficient are studied. The numerical values of natural frequencies are calculated and investigated. These numerical values of natural frequencies are very important in the designs of structures used to prevent resonance in the vibration of mechanisms.

Keywords: nonlinear; TSDT; FGM; spherical shells; vibration; frequency

1. Introduction

Free vibration frequency investigations with shear deformation effect and experimental studies in the spherical shells were presented. In 2021, Gan et al. [1] presented the free vibration of a shallow spherical shell by using the two-parameter foundation model of shear interaction between the spring elements. In 2021, Bagheri et al. [2] used the first order shear deformation theory (FSDT) of displacements to study the free vibrations of the conical–spherical functionally graded material (FGM) spherical shells. In 2021, Tang et al. [3] used the third-order shear deformation theory (TSDT) of displacements under the hygrothermal effects to obtain the frequency responses for the carbon fiber-reinforced polymer (CFRP) spherical shell panels. In 2022, Guo et al. [4] presented the FSDT of displacements and numerical spectral-Tchebyshev (ST) technique to study the free vibration of the laminated composite conical, cylindrical and spherical shells. In 2021, Gurve and Satankar [5] presented the results of free vibration for the stiffened cylindrical and spherical shells

by using the finite element method. In 2020, Gong et al. [6] presented the free vibration analysis of the FGM spherical torus shells based on the Ritz method with thin FSDT of displacements. In 2020, Du et al. [7] presented the Flügge's thin shell theory and energy method to obtain the vibration solutions for the truncated spherical shells. In 2019, Ghavanloo et al. [8] presented the numerical and experimental results by using the nonlocal spherical shell model for the free vibration of spherical fullerene molecules. In 2017, Okhovat and Boström [9] presented the eigen-frequency results of vibration for an isotropic spherical shell by using the power series method.

Free vibration frequency computational experiences in the composited FGM shells were presented. In 2020, Hong [10] used the thick displacement approach of TSDT to present the results of free vibration frequency for the thick FGM spherical shells with fully homogeneous equation. It is novel further to study the natural frequency in the TSDT of thick FGM spherical shells under free vibration with fully homogeneous equation and more considering the advanced shear correction coefficient. Three effects of nonlinear coefficient term, environment temperature and power law index on

the natural frequency of thick FGM spherical shells with advanced shear correction coefficient are investigated for the angle between the direction of z axis and the direction of radius in the spherical shells.

2. Formulation

Two-material thick FGM spherical shells for $0° \leqq \emptyset \leqq 90°$ in thermal environment is shown in Figure 1 with the axial length L in x direction, inner layer thickness h_1 of FGM material 1 and outer layer thickness h_2 of FGM material 2. A point in the coordinates $(r, \theta, \emptyset)$ correspond to (x, y, z), in which r is the radius, θ denotes the angle of circumferential direction, $\emptyset$ denotes the angle between direction of z axis and direction of r axis. The power-law material property functions of FGM spherical shells with power law index R_n and in functions of environment temperature T are used [11-12].
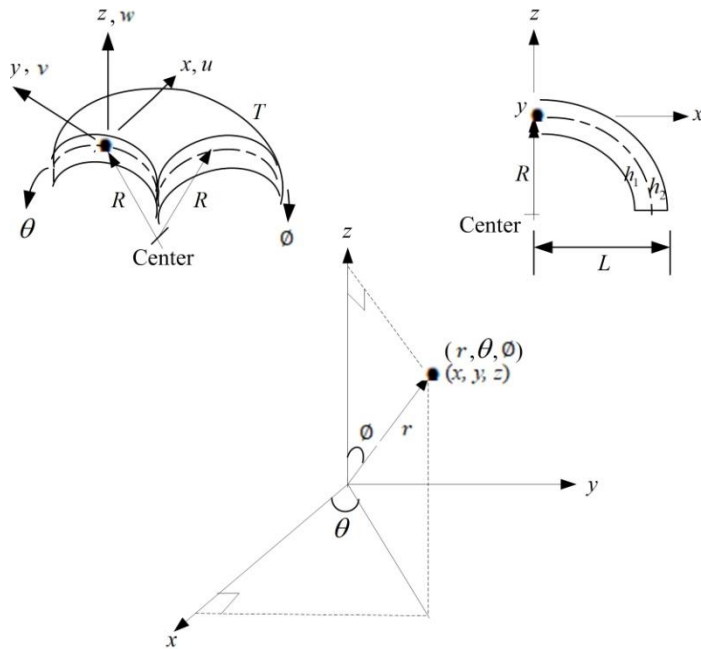
Figure 1. A point $(r, \theta, \emptyset)$ in two-material thick FGM spherical shell for $0° \leqq \emptyset \leqq 90°$ under environment temperature

2.1 Displacement TSDT equations

The time dependent of nonlinear displacements u, v and w of thick FGM spherical shells for a given $\emptyset$ angle are used in c_1 term of TSDT [13] as follows Eq. (1),

$$u = u_0(x, \theta, t) + z\phi_x(x, \theta, t) - c_1 z^3 (\phi_x + \frac{\partial w}{\partial x}),$$

$$v = v_0(x, \theta, t) + z\phi_\theta(x, \theta, t) - c_1 z^3 (\phi_\theta + \frac{\partial w}{R\partial \theta}),$$

$$w = w(x, \theta, t), \tag{1}$$

where u_0 and v_0 are tangential displacements in the in-surface coordinates x and θ axes direction, respectively, w is transverse displacement in the out of surface coordinates z axis direction of the

middle-plane of shells, ϕ_x and ϕ_θ are the shear rotations, R is the middle-surface radius of FGM spherical shells, t is time. Coefficient $c_1 = 4/(3h^{*2})$ is used and $h^* = h_1 + h_2$ is the total thickness of spherical shells for two layers of materials.

2.2 Fully homogeneous equation under free vibration

Fully homogeneous equation with TSDT in the elements of thick FGM spherical shells under free vibration in sinusoidal displacement and shear rotations forms for a given $\emptyset$ angle can be used [14][16]. The zero determinant of the coefficient matrix in equation for obtaining non-trivial solution of amplitudes in the five degree of λ_{mn} polynomial equation can be used [14]. When the root of λ_{mn} found and used $\lambda_{mn} = I_0 \omega_{mn}^2$, in which $I_i = \sum_{k=1}^{N^*} \int_{(k)}^{(k+1)} \rho^{(k)} z^i dz$, $(i = 0,1,2,…,6)$, N^* is total number of layers, $\rho^{(k)}$ is the density of (k) constituent plies. Then the natural frequency ω_{mn} in subscripts mode shape m and n can be got for a given angle $\emptyset \neq 0$ of thick FGM spherical shells under free vibration. In the coefficients of fully homogeneous equation and λ_{mn} polynomial equation are consisting of stiffness integrals ($A_{i^s j^s}, B_{i^s j^s}, D_{i^s j^s}, E_{i^s j^s}, F_{i^s j^s}, H_{i^s j^s}$, $i^s, j^s = 1,2,6$), $(A_{i^* j^*}, B_{i^* j^*}, D_{i^* j^*}, E_{i^* j^*}, F_{i^* j^*}, H_{i^* j^*}, i^*, j^* = 4,5)$ as follows Eq. (2) and c_1 terms [17],

$$(A_{i^s j^s}, B_{i^s j^s}, D_{i^s j^s}, E_{i^s j^s}, F_{i^s j^s}, H_{i^s j^s}) = \int_{-\frac{h^*}{2}}^{\frac{h^*}{2}} \overline{Q}_{i^s j^s}(1, z, z^2, z^3, z^4, z^6)dz$$

$$(A_{i^* j^*}, B_{i^* j^*}, D_{i^* j^*}, E_{i^* j^*}, F_{i^* j^*}, H_{i^* j^*}) = \int_{-\frac{h^*}{2}}^{\frac{h^*}{2}} k_\alpha \overline{Q}_{i^* j^*}(1, z, z^2, z^3, z^4, z^5)dz \tag{2}$$

where k_α is the advanced shear correction coefficient. $\overline{Q}_{i^s j^s}$ and $\overline{Q}_{i^* j^*}$ are the stiffness with z/R terms cannot be neglected are used and assumed in the following simple terms Eq. (3) containing $z/(R \sin\emptyset)$ for thick FGM spherical shells [17],

$$\overline{Q}_{11} = \overline{Q}_{22} = \frac{E_{fgm}}{1 - v_{fgm}^2} \quad , \quad \overline{Q}_{12} = \overline{Q}_{21} = \frac{v_{fgm}E_{fgm}}{(1 + \frac{z}{R\sin\emptyset})(1 - v_{fgm}^2)} \quad ,$$

$$\overline{Q}_{44} = \frac{E_{fgm}}{2(1 + v_{fgm})} \quad , \quad \overline{Q}_{55} = \overline{Q}_{66} = \frac{E_{fgm}}{2(1 + \frac{z}{R\sin\emptyset})(1 + v_{fgm})} \quad ,$$

$$\overline{Q}_{16} = \overline{Q}_{26} = \overline{Q}_{45} = 0, \tag{3}$$

in which $v_{fgm} = \frac{v_1 + v_2}{2}$ is the Poisson's ratios of the FGM spherical shells, $E_{fgm} = (E_2 - E_1)(\frac{z + h^*/2}{h^*})^{R_n} + E_1$ is the Young's modulus of the FGM spherical shells, E_1 and E_2 are the Young's modulus, v_1 and v_2 are the Poisson's ratios of the FGM constituent material 1 and 2, respectively.

2.3 Advanced k_α expression

For the advanced thick FGM spherical shells study, it is interesting to consider the extra effect of c_1 term of TSDT on the calculation of shear correction coefficient. The advanced k_α expression for a given angle $\emptyset$ in the thick FGM spherical shells can be used in a rational expression form as follows Eq. (4) [15],

$$k_\alpha = \frac{1}{h^*} \frac{FGMZSV}{FGMZIV} \qquad (4)$$

in which *FGMZSV* and *FGMZIV* are parameters in functions of E_1, E_2, c_1 and R_n. The values of advanced k_α are in functions of c_1, R_n and T, but not in functions of h^*.

3. Numerical results

In the calculation for choosing and iterating a λ_{mn} into the five degree of λ_{mn} polynomial equation, then the numerical root λ_{mn} can be solved and the numerical ω_{mn} can be got. The composited thick FGM SUS304/Si₃N₄ material is used under *T* and free vibration. The FGM material 1 is SUS304, the FGM material 2 is Si₃N₄. The geometric values are used basically for $L/R = 1$, $h_1 = h_2$ and $h^* = 1.2$ mm. For calculated values of advanced k_α are varied with c_1, *T* and R_n from 0.1 to 10 used by Hong [13].

3.1 Non-dimensional frequency

Firstly, for the non-dimensional frequency parameter $f^* = 4\pi\omega_{11}R\sqrt{I_2/A_{11}}$ values under the effects of c_1 =0.925925/mm² and c_1 =0/mm² for L/h^* =5, 8 and 10, respectively on $\emptyset = 10°, 45°$ and $90°$ are shown in Table 1, Table 2 and Table 3, where ω_{11} is the fundamental first natural frequency with subscripts $m = n = 1$. The f^* values under *T*=1K, 100K, 300K, 600K and 1000K with advanced k_α and c_1 =0.925925/mm² effects are in the values not greater than 82.795173 on $\emptyset = 10°$, not greater than 8.690546 on $\emptyset = 45°$, not greater than 32.68439 on $\emptyset = 90°$. Another non-dimensional frequency parameter $\Omega = (\omega_{11}L^2/h^*)\sqrt{\rho_1/E_1}$ values under the effects of c_1 =0.925925/mm² and c_1 =0/mm² for L/h^* =5, 8 and 10, respectively on $\emptyset = 10°, 45°$ and $90°$ are shown in Table 4, Table 5 and Table 6, ρ_1 is the density of SUS304, the Ω values under *T*=1K, 100K, 300K, 600K and 1000K with advanced k_α and c_1 =0.925925/mm² effects are in the values not greater than 214.34130 on $\emptyset = 10°$, not greater than 14.524525 on $\emptyset = 45°$, not greater than 108.10273 on $\emptyset = 90°$ as shown in Figure 3. It is interesting to compare the present vibration values of frequency with published work as shown in the Table 7 and Table 8. The values of f^* vs. h^* under L/h^* =10 and *T*=300K with advanced k_α and c_1 effects are shown in Table 7. The compared value f^* =3.011103 at c_1 = 0.925925/mm², R_n = 0.5 is smaller than 11.8186 of f^* in three-layer (0°/90°/0°) laminated composite spherical shell, *a/h*=10, *R/a*=10, TSDT presented by Sayyad and Ghugal in 2019 [16], in which *a* is the arc length in the *x* direction, *h* is the thickness in the *z* direction, *R* is the principal radius in the *x* direction. These different f^* values are mainly caused by different material and advanced k_α. The values of Ω vs. h^* under L/h^* =10 and *T*=1000K with advanced k_α and c_1

effects are shown in Table 8. The compared value Ω=40.250442 at c_1 =0.925925/mm², R_n =0.5 is smaller than 69.520 of Ω in composite laminated spherical shell, *h/R*=0.02, *n=m*=1, SS-SS for four sides simply supported, presented by Li et al. 2019 [18]. These different Ω values are mainly caused by different material and advanced k_α.

3.2 Natural frequency

Secondly, the dimensional natural frequency ω_{mn} (1/s) values of free vibration according to two dimensional mode shape of subscripts m and n are calculated. Values of first in $m = n = 1$ fundamental natural frequency ω_{11} vs. R_n, advanced k_α and the effects of c_1 =0.925925/mm² and c_1 =0/mm² for L/h^* = 5, 8 and 10, under *T*=1K, 100K, 300K, 600K and 1000K on $\emptyset = 10°$ are shown in Table 9. The values of ω_{11} are overestimated without the values of c_1, e.g. ω_{11} =0.016143/s with c_1 = 0/mm² is greater than ω_{11} =0.001437/s with c_1 =0.925925/mm² for L/h^*=5, R_n =0.5 under *T*=1K. For the values of natural frequency ω_{mn} vs. subscripts m, n =1,2,...,9 with R_n =0.5, *T*=300K under advanced k_α and the effects of c_1 =0.925925/mm² for L/h^*=5 and 10 on $\emptyset = 10°$ are shown in Table 10. The ω_{mn} values under the effects of advanced k_α and c_1 =0.925925/mm² are in the values not greater than 0.006482/s for L/h^*=5 and not greater than 0.007896/s for L/h^*=10, respectively on $\emptyset = 10°$.

3.3 Compared ω_{mn}

Finally, the dimensional natural frequency ω_{mn} (1/s) values vs. R_n and T of free vibration according to mode shape of subscripts m =1 and n from 1 to 9 are calculated. Figure 2 shows the values of ω_{1n} vs. R_n for thick L/h^* =5, 10 respectively on $\emptyset = 10°$, with the effects of advanced k_α and c_1 =0.925925/mm² under *T*=300K. Generally the values of ω_{1n} are keeping constant firstly then increasing and finally decreasing with values of subscript n from 1 to 9 for L/h^*=5, R_n =1, 0.5 and 10. The greatest value of ω_{14}=0.014334/s is found in Figure 2a for L/h^*=5, R_n =10. The values of ω_{1n} do be affected with R_n for L/h^*=5. The values of ω_{1n} are keeping constant with values of subscript n from 1 to 9 for L/h^*=10, R_n =1; ω_{1n} are almost keeping the lower constant with values of subscript n then increasing and finally decreasing for L/h^*=10, R_n =0.5 and 10, respectively. The greatest value of ω_{17} =0.036801/s is found in Figure 2b for L/h^*=10, R_n =10. The values of ω_{1n} also do be affected with R_n for L/h^*=10.
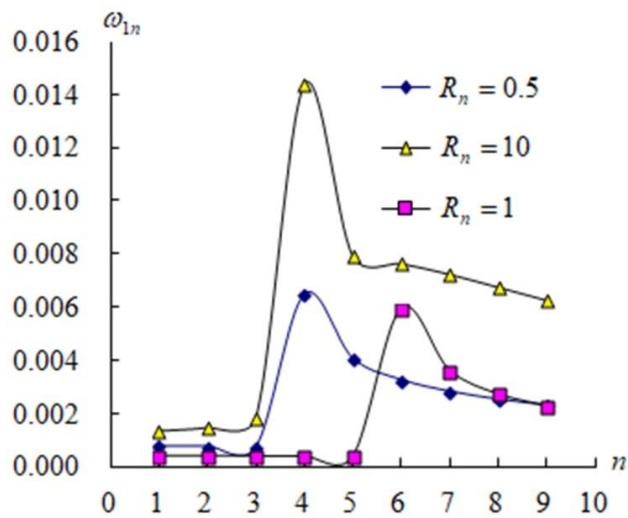
(a) ω_{1n} vs. R_n for $L/h^* = 5$
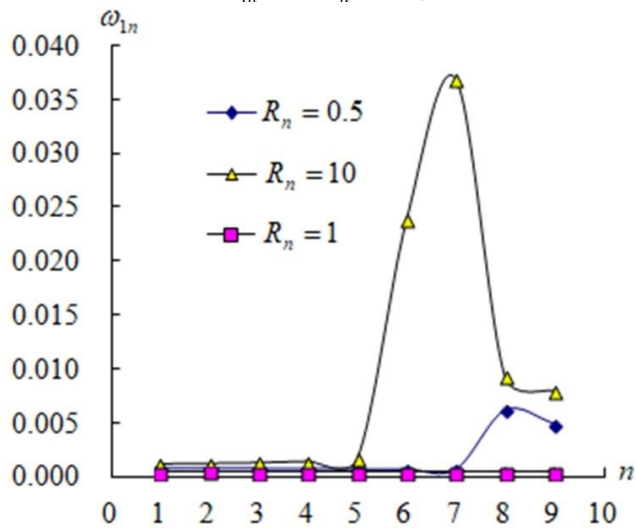
(a) ω_{1n} vs. T for $L/h^* = 5$

(b) ω_{1n} vs. R_n for $L/h^* = 10$

Figure 2. ω_{1n} vs. R_n for $L/h^* = 5$ and 10 on $\emptyset = 10°$ with the effects of advanced k_α and $c_1 = 0.925925/mm^2$ under $T = 300K$.
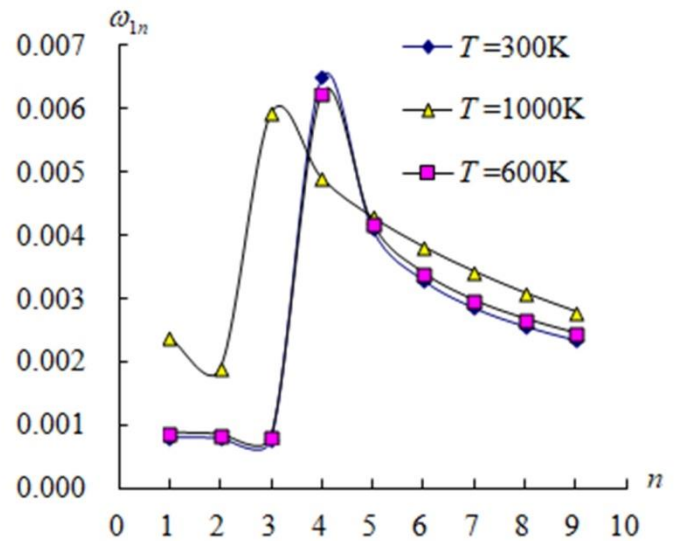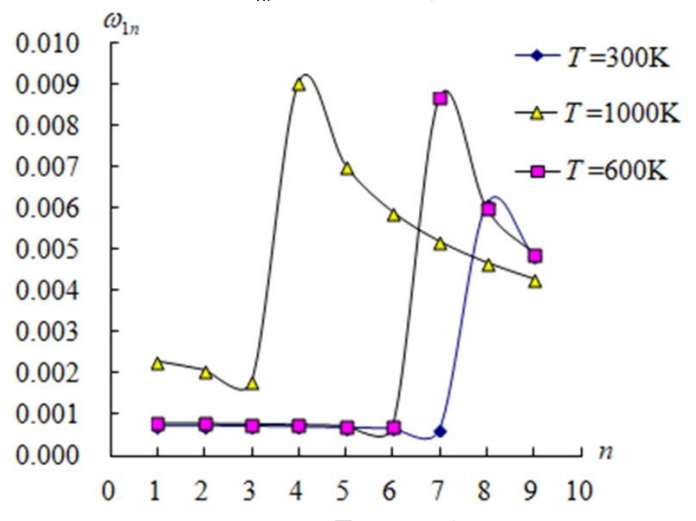
(b) ω_{1n} vs. T for $L/h^* = 10$

Figure 3. ω_{1n} vs. T for $L/h^* = 5$ and 10 on $\emptyset = 10°$ under the effects of advanced k_α, $c_1 = 0.925925/mm^2$ and $R_n = 0.5$

4. Conclusions

The values of natural frequency and frequency parameters respectively on $\emptyset = 10°, 45°$ and $90°$ are calculated and obtained by using the fully homogeneous equation in the free vibration of thick FGM spherical shells. Three important effect items are nonlinear coefficient term c_1, advanced shear correction coefficient and environment temperature that considered in the frequency calculation and investigation. Important results are contributed and found as follows. Numerical data investigated in the non-dimensional frequency parameters under free vibration with and without the c_1 value. The values of dimensional natural frequency ω_{mn} vs. R_n and T in free vibration according to two dimensional mode shape in subscripts m and n for the thick SUS304/Si$_3$N$_4$ FGM spherical shells are calculated under the effects of c_1 value and advanced k_α value.

Conflict of Interest Statement

The author declares that there is no conflict of interest in the study.

References

1. Gan, J., Yuan, H., Li, S., Peng, Q., & Zhang, H. (2021). An analytical method for shallow spherical shell free vibration on two-parameter foundation. Heliyon, 7, e05876.
2. Bagheri, H., Kiani, Y., & Eslami, M. R. (2021). Free vibration of FGM conical–spherical shells. Thin–Walled Structures, 160, 107387.
3. Tang, H., Dai, H. L., & Du, Y. (2021). Effect of hygrothermal load on amplitude frequency response for CFRP spherical shell panel. Composite Structures, 281 (EM6), 114978.
4. Guo, C., Liu, T., Bin, Q., Wang, Q., & Wang, A. (2022). Free vibration analysis of coupled structures of laminated composite conical, cylindrical and spherical shells based on the spectral-Tchebychev technique. Composite Structures, 114965.
5. Gurve, H. K., & Satankar, R. K. (2021). Free vibration analysis of

curved shells using finite element method. Materials Today Proceedings, 50 (1), 2336-2344.

6. Gong, Q., Li, H., Chen, H., Teng, Y., & Wang, N. (2020). Application of Ritz method for vibration analysis of stepped functionally graded spherical torus shell with general boundary conditions. Composite Structures, 243, 112215.

7. Du, Y., Sun, L., Li, S., & Li, Y. (2020). Vibration analysis of truncated spherical shells under various edge constraints. Thin-Walled Structures, 147, 106544.

8. Ghavanloo, E., Rafii-Tabar, H., & Ahmad Fazelzadeh, S. (2019). New insights on nonlocal spherical shell model and its application to free vibration of spherical fullerene molecules. International Journal of Mechanical Sciences, 161–162, 105046.

9. Okhovat, R., & Boström, A. (2017). Dynamic equations for an isotropic spherical shell using the power series method and surface differential operators. Journal of Sound and Vibration, 393, 415–424.

10. Hong, C. C. (2020). Free vibration frequency of thick FGM spherical shells with simply homogeneous equation by using TSDT. Journal of the Brazilian Society of Mechanical Sciences and Engineering, 42, 159, 1–15.

11. Hong, C. C. (2021). Vibration frequency of thick functionally graded material cylindrical shells with fully homogeneous equation and third-order shear deformation theory under thermal environment. Journal of Vibration and Control, 27 (17–18), 2004–2017.

12. Hong, C. C. (2020). Free vibration frequency of thick FGM circular cylindrical shells with simply homogeneous equation by using TSDT. Advances in Technology Innovation, 5 (2), 84–97.

13. Hong, C. C. (2024). Advanced frequency of thick FGM cylindrical shells with fully homogeneous equation. Journal of Structural Engineering & Applied Mechanics, 7 (1), 69–83.

14. Hong, C. C. (2024). Frequency of thick FGM spherical shells with TSDT under thermal environment. Journal of Vibration Engineering & Technologies, online 12 (4), 6619–6633.

15. Hong, C. C. (2023). Advanced frequency study of thick FGM cylindrical shells by using TSDT and nonlinear shear. Materials Plus, 2 (2), 87–97.

16. Sayyad, A. S., & Ghugal, Y. M. (2019). Static and free vibration analysis of laminated composite and sandwich spherical shells using a generalized higher-order shell theory. Composite Structures, 219, 129–146.

17. Hong, C. C. (2021). Thermal vibration of thick FGM spherical shells by using TSDT. International Journal of Mechanics and Materials in Design, 17 (2), 367–380.

18. Li, H., Pang, F., Miao, X., Gao, S., & Liu, F. (2019). A semi analytical method for free vibration analysis of composite laminated cylindrical and spherical shells with complex boundary conditions. Thin-Walled Structures, 136, 200–220.

APPENDIX

Table 1 f^* for SUS304/Si₃N₄ on $\emptyset = 10°$

L/h^*	R_n	c_1 (1/mm²)	f^* Present solution, advanced k_α				
			T=1K	T=100K	T=300K	T=600K	T=1000K
5	0.5	0.925925	2.820784	2.336545	1.620654	1.827490	5.420166
		0	31.672805	32.410423	33.958835	36.729087	42.579944
	1	0.925925	2.431303	1.865989	0.872658	1.057423	5.053874
		0	34.273555	132.53036	36.110019	39.073677	46.864479
	2	0.925925	1.224839	4.740484	15.659271	16.201717	3.756422
		0	37.479995	37.694744	38.649929	41.847938	52.400417
	10	0.925925	2.943557	2.958956	3.025853	3.291728	4.135724
		0	43.679279	43.131305	43.261871	46.893310	63.765880
8	0.5	0.925925	4.384293	3.617833	2.498185	2.818365	8.539231
		0	79.420143	81.302406	85.231727	92.140853	106.42930
	1	0.925925	3.770107	2.881380	1.341674	1.626429	7.958377
		0	86.240333	87.566551	90.857330	98.279922	117.73574
	2	0.925925	1.886321	11.747584	77.90464	82.795173	5.866292
		0	94.477165	329.58828	97.383865	105.41049	131.93212
	10	0.925925	4.429037	4.457534	4.565095	4.961815	6.188531
		0	109.88312	108.54094	108.90417	117.99297	159.63591
10	0.5	0.925925	5.300385	4.367766	3.011103	3.397310	10.34854
		0	122.11304	125.13778	131.29669	141.78059	161.99548
	1	0.925925	4.551788	3.474352	1.615177	1.957854	9.637208
		0	132.52432	134.76289	139.99891	151.25752	178.71736
	2	0.925925	2.271638	34.964645	2.891051	3.058258	7.084141
		0	144.84071	145.97044	149.92569	162.06086	198.96336
	10	0.925925	5.311273	5.344233	5.471844	5.947144	7.422325
		0	166.86840	871.42504	166.83900	180.36746	235.00473

Table 2 f^* for SUS304/Si₃N₄ on $\emptyset = 45°$

L/h^*	R_n	c_1 (1/mm²)	f^* Present solution, advanced k_α				
			T=1K	T=100K	T=300K	T=600K	T=1000K
5	0.5	0.925925	1.591143	1.923344	2.912015	2.954740	1.596829
		0	1.676810	1.839977	2.128164	2.280293	1.946411
	1	0.925925	1.797150	2.311825	8.690546	5.807613	1.726044
		0	1.658154	1.824377	2.116312	2.268444	1.914986
	2	0.925925	3.028405	5.893948	0.607843	0.640845	2.030289
		0	1.702577	1.870286	2.163931	2.320475	1.973235
	10	0.925925	4.431287	4.677474	5.118327	5.449218	5.400196
		0	2.008263	2.163172	2.443043	2.622124	2.432328
8	0.5	0.925925	1.118790	1.311380	1.806936	1.863120	1.156286
		0	0.712809	0.779661	0.894395	0.962980	0.842842
	1	0.925925	1.235278	1.505425	2.763189	2.666691	1.243545
		0	0.698829	0.766372	0.883941	0.951626	0.818396
	2	0.925925	1.766531	0.266276	1.958618	2.068104	1.425871
		0	0.718106	0.786101	0.904854	0.974335	0.841676
	10	0.925925	2.291216	2.416438	2.640617	2.814449	2.796801
		0	0.868164	0.931939	1.044738	1.126561	1.069076
10	0.5	0.925925	1.198938	1.359829	1.752298	1.822630	1.306651
		0	0.487702	0.531283	0.610783	0.657518	0.577413
	1	0.925925	1.292613	1.506000	2.416618	2.389040	1.389970
		0	0.478278	0.522153	0.603453	0.491572	0.560983
	2	0.925925	1.669677	0.318171	1.235356	1.306177	1.534058
		0	0.491173	0.535504	0.617843	0.664538	0.576723
	10	0.925925	1.488171	1.567301	1.708185	1.822322	1.823202
		0	0.594491	0.637972	0.714416	0.770527	0.733014

Table 3　f^*　for SUS304/Si$_3$N$_4$ on　$\phi = 90°$

L/h^*	R_n	c_1 (1/mm^2)	f^*				
			Present solution, advanced　k_α				
			T=1K	T=100K	T=300K	T=600K	T=1000K
5	0.5	0.925925	0.502130	0.570210	0.745849	0.773258	0.549213
		0	0.590006	0.643852	0.738035	0.792276	0.693156
	1	0.925925	0.542049	0.635356	1.088972	1.061970	0.583895
		0	0.584454	0.639541	0.735365	0.789534	0.682771
	2	0.925925	0.720395	0.147456	1.749742	1.857381	0.643730
		0	0.601933	0.657577	0.754101	0.809998	0.705449
	10	0.925925	0.439585	0.432449	1.912712	2.034272	0.575911
		0	0.714064	0.765051	0.856587	0.920757	0.874146
8	0.5	0.925925	0.384405	0.432271	0.549680	0.572973	0.417923
		0	0.275399	0.300743	0.345240	0.371763	0.325808
	1	0.925925	0.412331	0.475557	0.734396	0.732705	0.444527
		0	0.270439	0.296031	0.341274	0.367443	0.316992
	2	0.925925	0.520187	0.256231	0.966141	1.024323	0.492228
		0	0.278029	0.303717	0.349439	0.376290	0.326585
	10	0.925925	6.133640	0.966218	1.064178	1.131785	1.103627
		0	0.333380	0.359943	0.403599	0.435239	0.415926
10	0.5	0.925925	0.444867	0.489384	0.591412	0.618544	0.501530
		0	0.193089	0.209523	0.242446	0.259834	0.229385
	1	0.925925	0.468606	0.523140	32.68439	0.734637	0.529650
		0	0.184350	0.206358	0.239394	0.257086	0.215634
	2	0.925925	2.502079	0.307402	0.638958	0.678791	0.569559
		0	0.186246	0.211788	0.244852	0.263350	0.215261
	10	0.925925	0.481267	0.507236	0.551137	0.587717	0.588011
		0	0.236454	0.250857	0.283276	0.304129	0.291925

Table 4　Ω　for SUS304/Si$_3$N$_4$ on　$\phi = 10°$

L/h^*	R_n	c_1 (1/mm^2)	Ω				
			Present solution, advanced　k_α				
			T=1K	T=100K	T=300K	T=600K	T=1000K
5	0.5	0.925925	5.130447	4.151097	2.800106	3.170027	10.540805
		0	57.606563	57.580242	58.672813	63.711536	82.806861
	1	0.925925	4.236908	3.189765	1.458476	1.773653	9.323061
		0	59.726772	226.55050	60.350742	65.539665	86.452575
	2	0.925925	2.036923	7.772025	25.256298	26.214517	6.532387
		0	62.329700	61.800544	62.337131	67.710319	91.123886
	10	0.925925	4.532616	4.533440	4.611013	5.028469	6.503587
		0	67.259231	66.081817	65.925560	71.634582	100.27433
8	0.5	0.925925	12.758659	10.283887	6.906034	7.822132	26.570516
		0	231.11923	231.10652	235.61633	255.72911	331.16351
	1	0.925925	10.511957	7.880797	3.587748	4.364908	23.489767
		0	240.45861	239.50131	242.96005	263.75744	347.50613
	2	0.925925	5.019161	30.816268	201.03955	214.34130	16.322294
		0	251.38674	864.57617	251.30732	272.88812	367.08621
	10	0.925925	10.912035	10.927077	11.130595	12.127532	15.570733
		0	270.72439	266.07431	265.52966	288.39517	401.65393
10	0.5	0.925925	19.280702	15.519516	10.404945	11.786184	40.250442
		0	444.19888	444.63870	453.69909	491.87496	630.07775
	1	0.925925	15.864337	11.878280	5.398899	6.567957	35.55620
		0	461.88674	460.73370	467.96090	507.41922	659.37255
	2	0.925925	7.555527	114.64908	9.325755	9.896577	24.638525
		0	481.74383	478.63714	483.61996	524.43176	691.99127
	10	0.925925	16.357053	16.375883	16.676782	18.169807	23.343793
		0	513.90222	2670.2343	508.48257	551.06146	739.10821

Table 5 Ω for SUS304/Si3N4 on $\emptyset = 45°$

L/h^*	R_n	c_1 (1/mm²)	Ω Present solution, advanced k_α				
			T=1K	T=100K	T=300K	T=600K	T=1000K
5	0.5	0.925925	2.893975	3.417006	5.031271	5.125394	3.105416
		0	3.049786	3.268897	3.676963	3.955475	3.785260
	1	0.925925	3.131803	3.951888	14.524525	9.741315	3.184095
		0	2.889580	3.118633	3.536997	3.804941	3.532644
	2	0.925925	5.036276	9.663129	0.980370	1.036893	3.530656
		0	2.831408	3.066335	3.490129	3.754549	3.431440
	10	0.925925	6.823486	7.166394	7.799675	8.324268	8.492018
		0	3.092409	3.314214	3.722885	4.005577	3.824931
8	0.5	0.925925	3.255774	3.727669	4.995132	5.170932	3.597878
		0	2.074334	2.216230	2.472485	2.672671	2.622572
	1	0.925925	3.444252	4.117455	7.388997	7.156696	3.670421
		0	1.948502	2.096088	2.363733	2.553913	2.415561
	2	0.925925	4.700423	0.698495	5.054381	5.353939	3.967326
		0	1.910751	2.062102	2.335054	2.522374	2.341868
	10	0.925925	5.644982	5.923592	6.438341	6.878999	7.036926
		0	2.138940	2.284530	2.547276	2.753511	2.689863
10	0.5	0.925925	4.361263	4.831735	6.055112	6.323195	5.082191
		0	1.774068	1.887752	2.110576	2.281108	2.245835
	1	0.925925	4.505143	5.148783	8.077796	8.014444	5.128254
		0	1.666944	1.785161	2.017106	1.978877	2.069731
	2	0.925925	5.553389	1.043285	3.984929	4.226814	5.335431
		0	1.633654	1.755920	1.992995	2.150459	2.005833
	10	0.925925	4.583100	4.802551	5.206111	5.567587	5.734112
		0	1.830847	1.954885	2.177357	2.354128	2.305386

Table 6 Ω for SUS304/Si3N4 on $\emptyset = 90°$

L/h^*	R_n	c_1 (1/mm²)	Ω Present solution, advanced k_α				
			T=1K	T=100K	T=300K	T=600K	T=1000K
5	0.5	0.925925	0.913275	1.013033	1.288651	1.341320	1.068076
		0	1.073105	1.143866	1.275150	1.374310	1.348008
	1	0.925925	0.944602	1.086094	1.820001	1.781280	1.077132
		0	1.018498	1.093247	1.229017	1.324313	1.259533
	2	0.925925	1.198026	0.241754	2.822099	3.005259	1.119442
		0	1.001023	1.078098	1.216264	1.310585	1.226770
	10	0.925925	0.676893	0.662559	2.914729	3.107570	0.905644
		0	1.099547	1.172142	1.305329	1.406556	1.374629
8	0.5	0.925925	1.118652	1.228756	1.519547	1.590239	1.300403
		0	0.801435	0.854879	0.954389	1.031797	1.013780
	1	0.925925	1.149677	1.300685	1.963837	1.966387	1.312058
		0	0.754050	0.809668	0.912595	0.986122	0.935628
	2	0.925925	1.384125	0.672145	2.493210	2.651783	1.369569
		0	0.739785	0.796712	0.901757	0.974145	0.908687
	10	0.925925	15.111748	2.368561	2.594676	2.766279	2.776796
		0	0.821366	0.882354	0.984053	1.063799	1.046497
10	0.5	0.925925	1.618253	1.738877	2.043641	2.145896	1.950690
		0	0.702381	0.744476	0.837780	0.901436	0.892191
	1	0.925925	1.633234	1.788537	109.2509	2.464468	1.954131
		0	0.642515	0.705509	0.800200	0.862442	0.795578
	2	0.925925	108.10273	1.007971	2.061109	2.196582	1.980920
		0	0.619460	0.694453	0.789826	0.852205	0.748676
	10	0.925925	1.482151	1.554282	1.679727	1.795602	1.849342
		0	0.728204	0.768680	0.863353	0.929181	0.918128

Table 7 Comparison of frequency f^* for SUS304/Si$_3$N$_4$ on $\emptyset = 10°$

c_1 (1/mm²)	h^* (mm)	Present method, L/h^*=10, T=300K, advanced k_α, SUS304/Si₃N₄			Sayyad and Ghugal [16], a/h=10, R/a=10
		$R_n = 0.5$	$R_n = 1$	$R_n = 2$	
0.925925	1.2	3.011103	1.615177	2.891051	11.8186
0.333333	2	23.323301	15.971736	9.100513	-
0.000033	200	15716.966	11534.686	9898.7031	-
0.000014	300	28897.183	21148.072	18228.677	-
0.000003	600	82492.976	60802.226	49333.960	-
0.000001	900	154100.14	110533.68	93945.585	-

Table 8 Comparison of frequency Ω for SUS304/Si$_3$N$_4$ on $\emptyset = 10°$

c_1 (1/mm²)	h^* (mm)	Present method, L/h^*=10, T=1000K, advanced k_α, SUS304/Si₃N₄			Li et al. [18], h/R=0.02,
		$R_n = 0.5$	$R_n = 1$	$R_n = 2$	
0.925925	1.2	40.250442	35.556209	24.638525	69.520
0.333333	2	2474.4003	1039.7077	70.613998	-
0.000033	200	-	-	-	-
0.000014	300	-	-	-	-
0.000003	600	-	-	-	-
0.000001	900	-	-	-	-

Table 9 ω_{11} for advanced k_α on $\emptyset = 10°$

L/h^*	R_n	c_1 (1/mm²)	ω_{11}				
			T=1K	T=100K	T=300K	T=600K	T=1000K
5	0.5	0.925925	0.001437	0.001177	0.000797	0.000865	0.002389
		0	0.016143	0.016328	0.016713	0.017395	0.018770
	1	0.925925	0.001187	0.000904	0.000415	0.000484	0.002113
		0	0.016737	0.064243	0.017191	0.017894	0.019597
	2	0.925925	0.000570	0.002203	0.007194	0.007157	0.001480
		0	0.017467	0.017524	0.017757	0.018486	0.020655
	10	0.925925	0.001270	0.001285	0.001313	0.001372	0.001474
		0	0.018848	0.018738	0.018779	0.019558	0.022730
8	0.5	0.925925	0.001396	0.001139	0.000768	0.000834	0.002352
		0	0.025299	0.025599	0.026217	0.027274	0.029323
	1	0.925925	0.001150	0.000872	0.000399	0.000465	0.002079
		0	0.026322	0.026529	0.027034	0.028130	0.030770
	2	0.925925	0.000549	0.003413	0.022370	0.022859	0.001445
		0	0.027518	0.095769	0.027963	0.029104	0.032504
	10	0.925925	0.001194	0.001210	0.001238	0.001293	0.001378
		0	0.029635	0.029473	0.029546	0.030757	0.035565
10	0.5	0.925925	0.001350	0.001100	0.000740	0.000804	0.002280
		0	0.031120	0.031521	0.032309	0.033574	0.035706
	1	0.925925	0.001111	0.000842	0.000384	0.000448	0.002014
		0	0.032359	0.032662	0.033325	0.034635	0.037366
	2	0.925925	0.000529	0.008127	0.000664	0.000675	0.001396
		0	0.033750	0.033931	0.034440	0.035796	0.039215
	10	0.925925	0.001145	0.001160	0.001187	0.001240	0.001322
		0	0.036003	0.189300	0.036211	0.037613	0.041885

Table 10 ω_{mn} vs. m and n for advanced k_α, c_1, $R_n = 0.5$ and T=300K on $\emptyset = 10°$

c_1 (1/mm²)	L/h^*	ω_{1n}								
		$n=1$	$n=2$	$n=3$	$n=4$	$n=5$	$n=6$	$n=7$	$n=8$	$n=9$
0.925925	5	0.000797	0.000783	0.000752	0.006482	0.004085	0.003281	0.002841	0.002548	0.002328
	10	0.000740	0.000738	0.000729	0.000714	0.000694	0.000670	0.000643	0.006078	0.004855

L/h^*	ω_{2n}								
	$n=1$	$n=2$	$n=3$	$n=4$	$n=5$	$n=6$	$n=7$	$n=8$	$n=9$
5	0.000572	0.000556	0.000529	0.005008	0.003541	0.002924	0.002574	0.002343	0.002176
10	0.000457	0.000453	0.000444	0.000433	0.000419	0.000403	0.006604	0.004884	0.004041

L/h^*	ω_{3n}								
	$n=1$	$n=2$	$n=3$	$n=4$	$n=5$	$n=6$	$n=7$	$n=8$	$n=9$
5	0.000524	0.000508	0.007423	0.003973	0.003031	0.002572	0.002299	0.002117	0.001984
10	0.000366	0.000362	0.000354	0.000344	0.000333	0.007896	0.005026	0.003960	0.003366

L/h^*	ω_{4n}								
	$n=1$	$n=2$	$n=3$	$n=4$	$n=5$	$n=6$	$n=7$	$n=8$	$n=9$
5	0.000517	0.000500	0.004858	0.003212	0.002576	0.002237	0.002028	0.001886	0.001782
10	0.000326	0.000322	0.000315	0.000306	0.000296	0.005535	0.003978	0.003264	0.002833

L/h^*	ω_{5n}								
	$n=1$	$n=2$	$n=3$	$n=4$	$n=5$	$n=6$	$n=7$	$n=8$	$n=9$
5	0.000528	0.007756	0.003626	0.002636	0.002188	0.001937	0.001778	0.001668	0.001588
10	0.000306	0.000302	0.000296	0.000287	0.007862	0.004218	0.003251	0.002744	0.002420

L/h^*	ω_{6n}								
	$n=1$	$n=2$	$n=3$	$n=4$	$n=5$	$n=6$	$n=7$	$n=8$	$n=9$
5	0.000552	0.004778	0.002844	0.002185	0.001860	0.001673	0.001554	0.001471	0.001411
10	0.000295	0.000291	0.000285	0.000277	0.005087	0.003386	0.002729	0.002350	0.002098

L/h^*	ω_{7n}								
	$n=1$	$n=2$	$n=3$	$n=4$	$n=5$	$n=6$	$n=7$	$n=8$	$n=9$
5	0.000593	0.003436	0.002277	0.001814	0.001578	0.001442	0.001355	0.001295	0.001252
10	0.000288	0.000285	0.000279	0.000271	0.003827	0.002821	0.002341	0.002046	0.001844

L/h^*	ω_{8n}								
	$n=1$	$n=2$	$n=3$	$n=4$	$n=5$	$n=6$	$n=7$	$n=8$	$n=9$
5	0.005514	0.002590	0.001818	0.001491	0.001326	0.001233	0.001176	0.001137	0.001109
10	0.000285	0.000281	0.000275	0.006030	0.003103	0.002414	0.002043	0.001805	0.001639

L/h^*	ω_{9n}								
	$n=1$	$n=2$	$n=3$	$n=4$	$n=5$	$n=6$	$n=7$	$n=8$	$n=9$
5	0.003625	0.001917	0.001388	0.001176	0.001084	0.001037	0.001010	0.000992	0.000978
10	0.000283	0.000279	0.000273	0.003911	0.002623	0.002107	0.001808	0.001611	0.001471

ENGINEERING PERSPECTIVE

Research Paper
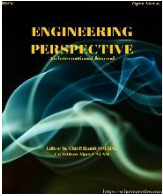
Investigation of the Effects of CNC Tool Runout on Machining of 1.2379 Steel and Tool Life

M. Kubilay Askerden [1,*] (iD) Mustafa Yazar [2,*] (iD) Şükrü Talaş [3,*] (iD)

[1] *Mechanical Engineering Departmant, Uludag University, Bursa, Turkey*
[2] *Şahinkul Machinery and Spare Parts Industry. Trade A.S, Bursa, Turkey*
[3] *Metallurgical and Materials Engineering Departmant, Afyon Kocatepe University, Afyon, Turkey*

ABSTRACT

In the study, the effects of tool run-out caused by the CNC spindle mechanism on surface roughness, measurement accuracy, consumable expenses, maintenance costs and cutting tool life that may occur during the cutting process were investigated based on metal die manufacturing. Before starting the experimental studies, the machine spindle health was measured. Here, tool pulling force, 300 mm test bar run-out, inner conical run-out and spindle vibration values were examined and evaluated. According to the results obtained, the m3/life relationship was compared with the surface milling operation by eliminating the factors causing tool run-out before and after machine tool maintenance for cutting tool life. In order to examine the effect of run-out on surface roughness and measurement accuracy, the effect of run-out was examined and compared by applying outer contour and inner contour operations before and after maintenance with experimental studies. These operations were examined with 1.2379 steel, which is the most commonly used steel type in the metal die sector in terms of mechanical properties. The results showed that run-out has serious negative effects on the cutting process and cutting tool life, measurement accuracy and surface roughness. In operations performed with a healthy spindle after maintenance, the cutting tool life increased by an average of 40%, surface roughness and dimensional accuracy reached the desired levels. The stress during the machine operation decreased by an average of 15%.

Keywords: Tool Runout, Tool Life, Spindle, Periodic Maintenance, CNC Machine Tool

1. Introduction

Milling operations are one of the most commonly used cutting operations in machining. In operations performed with multi-flute tools in milling, cutting tool runout affects chip removal performance, cutting tool performance, chip load and cutting parameters [1, 2]. In milling operations with multi-flute tools, the tool is never completely symmetrical. There is always a deviation along the axis of rotation of the spindle and the axis of the tool geometry. Tool runout greatly affects the actual cutting radius of the tool. It has been determined that affecting the tool radius negatively affects the quality and efficiency in cutting operations. There are many simulation modelling and studies on this subject, which enable cutting processes that lead to better surface precision, higher productivity, and longer tool life [3].

Tool runout is triggered by the lack of periodic maintenance of the conical, spindle bearings and drawbar springs to which the tool is attached on the spindle. These structures can be seen in Figure 1. Periodic maintenance brings many effects such as increased production efficiency and longer use of the machine in a better way [4].

Zhang et al. considering the spindle speed-dependent effect of cutter runout, an effective non-contact calibration method was proposed by [6], and the effect of cutter runout on milling mechanics and dynamics was discussed. The proposed models have been successfully validated through a series of experiments. It shows that the cutter runout has spindle speed-dependent properties due to the change of vibration response of the spindle system under different spindle speeds. An approach is presented to model the milling process geometry together with the cutter runout based on the actual tooth trajectory of the cutter in the milling process. The mathematical relationship between the trajectories produced by successive incisors

and runout was analyzed. It has been observed that the change in the cutter radius for a tooth compared to the previous one causes variable metal removal loads and variable wear on the teeth in evaluating the effects of cutter runout [7]. Soshi et al. According to the studies of [8], there are software and studies that compensate for the dynamic conditions that will change depending on the cutting parameters. It is observed that the variability of spindle dynamic properties affects the run-out rotation of the tool, tool life and cutting parameters. With these studies, improvements in cutting tool life and spindle runout were observed [8]. It is also possible for cutting tool runouts to occur as a result of incorrect attachment of tools in milling operations. Accordingly, it has been observed that unequal cutting forces loaded on the cutting edges cause different wear rates on the cutting tool and, as a result, shorten the tool life [12].
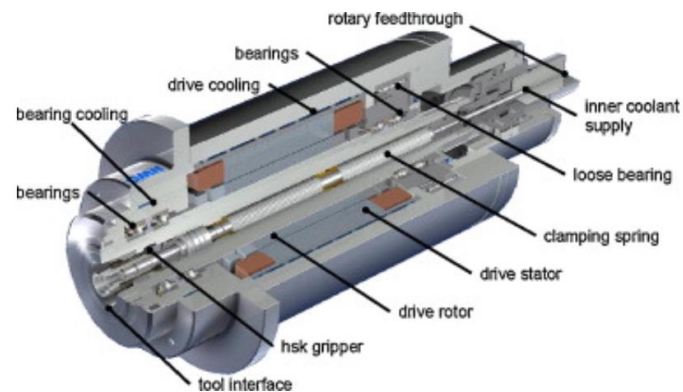

Figure 1. Appearance and layout of CNC spindle parts [5]

In milling operations, it is also possible for tools to be connected incorrectly and resulting in cutter run-out. Accordingly, it has been observed that unequal cutting forces loaded on the cutting edges shorten the tool life along with different wear rates on the cutting tool. Therefore, the variable cutting forces in the milling process were analyzed and a simulation was created. With the cutting parameters optimized as a result of the analysis of the variable cutting forces created by the epidemic, the epidemic is controlled and the factors related to the epidemic are prevented [9]. Cifuentes et al. In his study, it was observed that tool runout affected tool life and deteriorated the workpiece surface quality. In this study, actions that can be taken to reduce the effects of tool run-out are presented. The simulation and experimental results presented in this study demonstrate the effectiveness and benefits of this new tool runout correction procedure [10]. It is motivated by the fact that cutting forces are commonly calculated by mechanical or numerical models, which are considered time-consuming and impractical for various cutting conditions and workpiece-tool pairs, producing uneven distribution of cutting forces due to uneven cutting forces. Fu et al. The proposed analytical model of cutting forces has been validated with the obtained results and experimental data. While the effectiveness of the proposed analytical model is demonstrated, the importance of cutter runout on forces is emphasized [11]. The presence of cutter runout created a cutting force component at the spindle rotation frequency. The study used time-dependent spectral analysis of cutting force to estimate cutter runout characteristics of size and angular orientation; Given preliminary information about the part's material properties,

tool geometry, cutting parameters and machining configuration, the instantaneous runout characteristics are repeatedly updated from their previous values and the last measurements of the cutting force. The recursive nature of this approach facilitates in-process implementation of runout monitoring and provides opportunities for control and optimization [12]. Cutting tool runout occurs in two different ways: radial and axial (Figure 2). It is a phenomenon that affects geometry accuracy in the milling process and is neglected in most studies on tool path planning. In this study, a new approach is presented to integrate the cutter runout effect into envelope surface modeling and tool path optimization for five-axis side milling with a tapered cutter. The results show that geometry errors caused by runout can be significantly reduced using the proposed method [13]. These errors can be eliminated through periodic maintenance and their effects on the final product can be minimized [15].
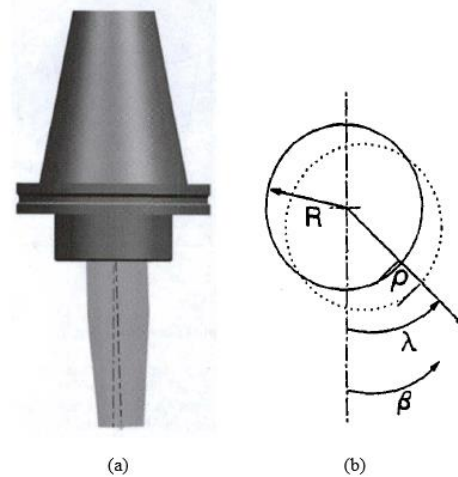

Figure 2. (a) cutting tool with axial runout [13] (b) cutting tool path with radial runout [14]

The study is about tool runout measurement in micro milling. Among the macro-to-micro effects of downscaling, tool runout plays an important role, affecting the cutting force, tool life, and surface integrity of the produced part. The results showed that the developed procedure can be used for tool runout prediction. The maximum measurement errors of tool run-out length and angle decrease as the spindle speed decreases [16] .

The purpose of this study is to reveal the effects of CNC spindle maintenance and health on the final product. In this context, the impact on consumable expenses and costs, in addition to the final product, will be examined. The study aims to present an innovative perspective that expresses the importance of periodic maintenance, which is constantly emphasized in companies, with numerical data. With this innovative perspective, new insights will be provided on various aspects such as labor costs, cutting tool costs, process times, and maintenance costs. The fact that this study is conducted experimentally and under real conditions, rather than mathematically, strengthens its innovative perspective. As a result of the study, it is aimed to contribute to the development of the literature by establishing a foundation for optimization in future research.

2. Materials and Methods

In the experimental study, 1.2379 steel (supplied by the Sağlam Metal Company)   , which is the most preferred steel in terms of its technical properties in die manufacturing in the metal sheet forming industry, was used. Technical properties of steel are given in Table 1. In the machining of steel, cutting operations such as surface treatment, outer contour and inner contour are applied. At this point, with the experimental study to be carried out, the effect of CNC spindle tool runout on the cutting tool life during surface processing was examined. At the same time, the effects of runout on surface roughness and dimensional accuracy in outer contour and inner contour operations were also examined. CMM (Coordinate Measuring Machine) device was used for dimensional accuracy. Mahr Brand MarSurf PS1 model roughness device was used for surface roughness. Spindle technical specifications of the HAAS VM3 CNC vertical machining center used are given in Table 2. Again, the HAAS machine was checked for runout before maintenance, and the measurement values are given in Figure 7. After the maintenance, along with bearing maintenance, drawbar spring maintenance and conical grinding, the runout from 45 µm was reduced to 8 µm and the machine was brought to optimum operating values. Cooling liquid was used in the experimental study. It is known that the effect of coolant and the water used in the coolant on cutting tool life, surface roughness and production efficiency is very important [17]. During the cutting operation, Oemeta brand coolant suitable for general and heavy machining was used. The properties of the coolant and the water used are shown in Table 3. At the same time, the cutting tool, tool holder and processing parameters to be used are given in Table 4. Cutting parameters are given based on optimum processing conditions, adhering to the values in the product catalogue.

Table 1. Technical specifications of 1.2379 steel

Carbon (C)	Chromium (Cr)	Molybdenum (Mo)	Vanadium (V)	Hardness (HRC)
1.55	12.00	0.80	0.90	55

First of all, in the surface processing operation, the effects of the cutting parameters prepared in accordance with the parameters of the cutting tool in terms of "m 3 / tool life" and the current runout in the spindle) on the cutting tool life and chip formation during the process were examined. For the operation, 1.2379 steel was used, cut into billets measuring 280x280x100mm. After spindle maintenance, the process was repeated and compared with the same teething parameters and material.

Table 2. Spindle specifications of the HAAS VM3 machine

Spindle	Metric
Maximum Speed	12000rpm
Maximum Torque	122.0 Nm @ 2000 rpm
Conical Type	CT/BT40

In the outer contour operation, the workpiece called cavity die is processed in die manufacturing. 1.2379 steel with dimensions 110x90x85mm was used for the test. In addition, the cavity die was processed by performing the process called pool emptying with the inner contour operation. The dimensional accuracy and surface roughness of the metal dies, which will fit into each other by machining the inner and outer contours, were checked and after maintenance, the same operations with the same cutting parameters were repeated and compared.

In line with the determined parameters, the experimental study was repeated 5 times and the average was taken to estimate the cutting tool life. For measurement accuracy, a comparison was made with the average of measurements taken from 5 different points. For surface roughness, the average of the measurements from 5 different points was taken and compared. Surface processing, outer contour and inner contour operations during the experimental study are shown in Figure 3. The tools and holders used during the study are also shown in Figure 4.

3. Findings and Discussion

As a result of the studies and experiments carried out, when the cutting tool life is examined after the conical, drawbar springs and bearing maintenance, which may cause run-out before and after run-out, as seen in Table 5, run-out affects the cutting tool life by 40%. In the surface machining operation, 3 cutting inserts are connected to the tool holder. The wear images of the cutting tools as a result of the operation when there is tool run-out are given in Figure 5.
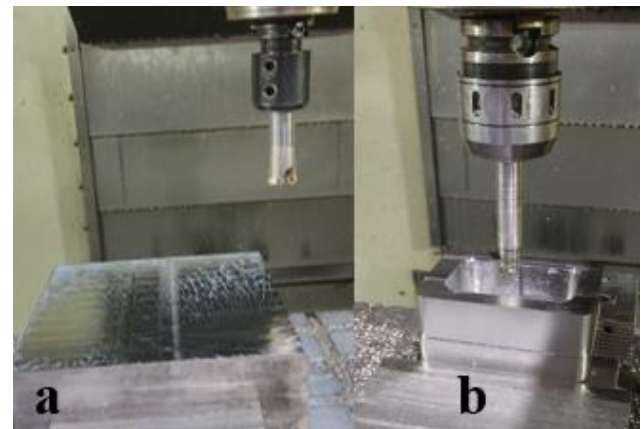
Figure 3. Cutting operation pictures (a) surface processing operation (b) Inner contour and outer contour operation

It is seen that the run-out creates different wear in the 3 cutting inserts on top of the tool wear. Figure 6 shows the wear resulting from machining before and after maintenance. Here (Figure 6a) is the cutting tool used with run-out, and (Figure 6b) is the image of the cutting tool that removes 40% more metal without run-out after maintenance.

Table 3. Coolant used and its properties

Brand	Product Code	Emulsion Rate (% refractometer)	Use Area	Product Type	Properties of Water
OEMETA	Unimet 227	5%	*General Machining *Heavy Machining	Semi Synthetic	*Hardness = 15 °dH *Chloride = 55 ppm *pH = 7.8 *Conductivity = 655 µs/cm

Table 4. Cutting parameters

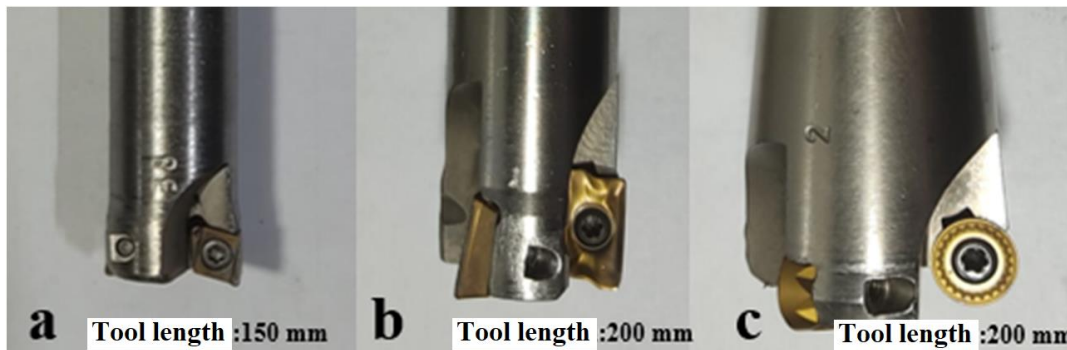| Operation	F (mm/min)	Ap (mm)	Vc (m/min)	Brand code	Tool Holder	Team Brand
Surface Treatment	1250	1	150	RYMX 1205-M	Ø40 Ball	TaeguTec
Outer Contour	1000	0.5	125	APKT 1705 PER-EM	Ø32 Ball	TaeguTec
Inner Contour	2000	0.5	125	4NKT 060308R-M	Ø20 Ball	TaeguTec

Figure 4. Insert and holders (a) Inner contour operation (b) Outer contour operation (c) Surface treatment operation

Table 5. Cutting tool life results

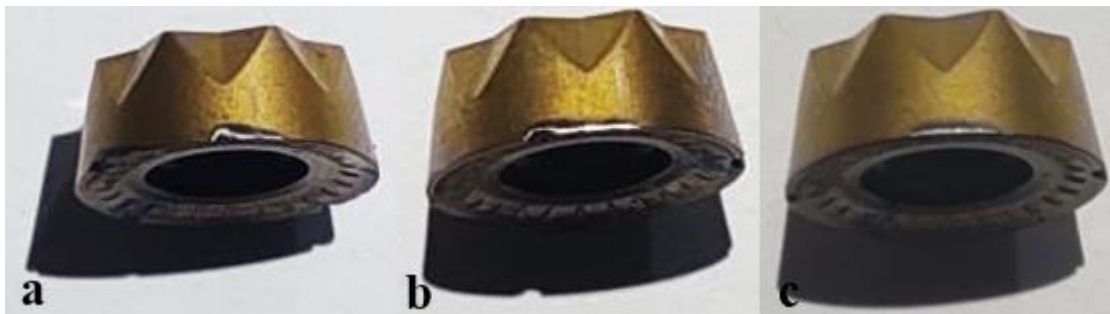|	Cutting tool life before maintenance (m^3/tool life)	Cutting tool life after maintenance (m^3/tool life)	% Difference
HAAS VM3	0.000131 m^3/tool life	0.0001834 m^3/tool life	40%

Figure 5. Different wear forms of the inserts in the tool holder when the tool is run-out

Dimensional analysis was carried out with the run-out effect of the CNC machine programmed to the specified dimensions in the inner contour and outer contour operations, and the studs in the machining dimensions were detected in the CMM (Coordinate Measuring Machine) device. After the maintenance was done in the same way, the steel processed with the same parameters was checked and compared on the CMM device. In terms of dimensional accuracy and precision in the inner contour and outer contour, the run-out loom showed an average deviation of 0.2 mm. Test results are shown in Table 6.
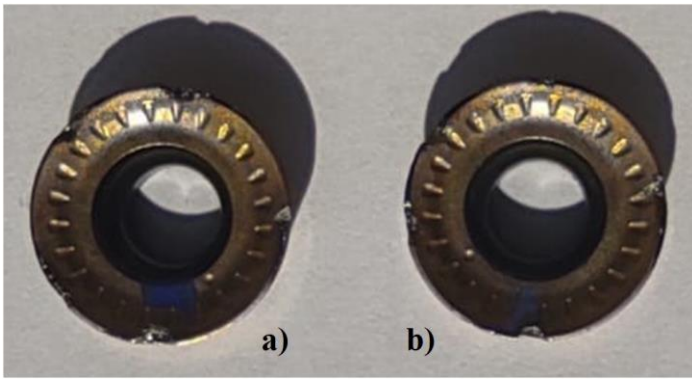
Figure 6. Tool wear during machining (a) before maintenance (b) after maintenance

Table 6. Effect of the epidemic on measurement accuracy

	Measuring range before maintenance (mm)	Measuring range after maintenance (mm)
Outer Contour	+0.25 +0.20	+0.05 +0.00
Inner Contour	- 0.10 - 0.15	+0.05 +0.00

The effects of run-out on the chips formed in machining and post-running operations are also discussed, and as seen in Figure 7, the chips produced by the tool working with and without run-out are seen. When working with a spiral operating spindle tool, there is no serious change in chip shapes, but the heat generated during chip processing reaches $300\square C$ and above and suddenly oxidizes, forming different iron compounds on the surface. These compounds are of three types: Wüstite (FeO), hematite (Fe_2O_3) and magnetite (Fe_3O_4).Under normal conditions, during processing, the first layer formed is FeO (wüstite) due to the high oxygen density, and immediately afterwards a new layer forms as magnetite (Fe_3O_4). In the last stage, the final colour is given with Fe_2O_3 (hematite). The presence of a layer that gives a dark brown and blue colour in the chips produced with the run-out tool is understood to be due to temper oxidation, where the cutting temperature during machining exceeds $300\square C$ (18, 19). The fact that the 2379 steel processed in the oscillating spindle set is alloyed suggests that it causes more heat generation because the steel is harder than normal steels. The change in chip color due to the high amount of heating occurring in the chip is seen very little or not at all in machining performed after maintenance. Since the physical values of the cooling liquid remain the same, the slight or no colour change indicates that the generated heat is absorbed by the cooling liquid and removed from the environment, unlike the situation in the gland tool.

While the machine axial loading varied between 45-50% before maintenance, the machine loading after maintenance varied between 40-45%. With the maintenance, a 10% improvement was observed in the machine axial load read on the machine monitor.

Surface roughness was measured as a result of the experiments and measurements were made from 5 different points before and af-ter runout and their averages were taken. According to the experimental results, the surface roughness before and after the maintenance has a serious effect on the surface roughness, as shown in Figure 8.
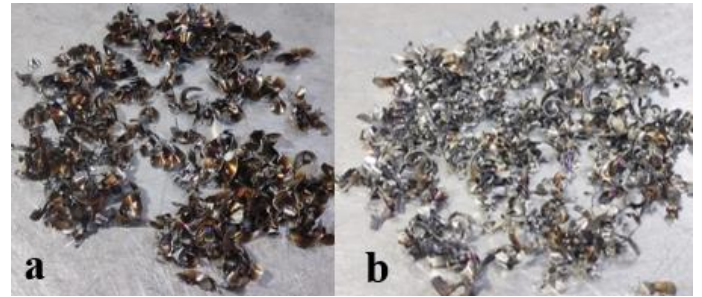

Figure 7. Chip structures formed during surface processing (a) chip before maintenance (b) chip after maintenance, (f=1250 rpm, ap=1mm, V=150m/min)
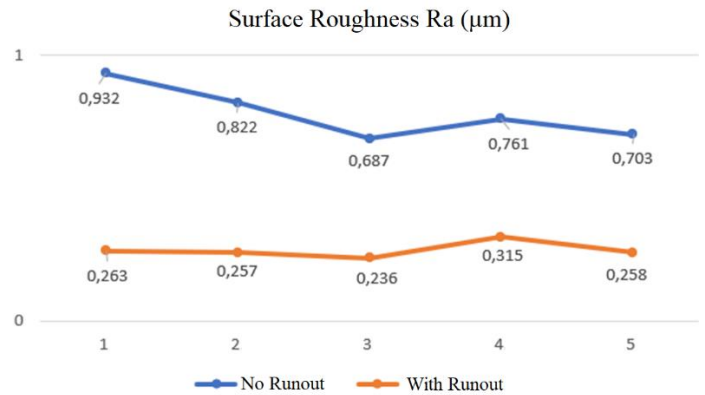

Figure 8. Surface roughness graphs before and after maintenance

4. Conclusions

CNC tool runouts are of great importance for machining. In metal forming dies, it is an opportunity to adapt and adapt the dies to each other and to prevent excessive hand levelling. It prevents cutting tool life and frequent replacement of cutting tools, and at this point, it is important to increase efficiency in terms of cost. At this point, it is very important to carry out periodic maintenance and controls on time and increase production efficiency.

After the maintenance has been carried out and the tool runout has been eliminated and the machine has been brought to optimum values:

•Cutting tool life was measured by the volume of chip removed in m3/tool life, and tool life increased by 40%.

•The dimensional accuracy improved by 0.2 mm after the maintenance for the outer contour operation compared to before.

•Dimensional accuracy improved by 0.15 mm after maintenance for the inner contour operation compared to before.

•Surface roughness improved by approximately 35% for Ra (μm) after maintenance compared to before.

•After the machine spindle was maintained and its runout was removed, the axial load of the machine, read on the machine monitor during the cutting process, decreased by 10%.

•Improvements in surface roughness and cutting tool life have yielded positive results in terms of reducing production costs.

Conflict of Interest Statement

The authors declare that there is no conflict of interest in the study.

Author Statement

M. Kubilay Askerden: Conceptualization, Supervision, **Mustafa Yazar:** Conceptualization, Writing-original draft, **Şükrü Talaş:** Data curation, Validation

References

1. Aydın, M. (2022). Parmak frezeleme sırasında takım salgısının etkisi dahil edilerek kesme kuvvetlerinin tahmini ve analizi. Politeknik Dergisi, 25(1), 157-167.

2. Kline, W. A., & DeVor, R. E. (1983). The effect of runout on cutting geometry and forces in end milling. International Journal of Machine Tool Design and Research, 23(2-3), 123-140.

3. Caixu, Y. U. E., Haining, G. A. O., Xianli, L. I. U., Liang, S. Y., & Lihui, W. A. N. G. (2019). A review of chatter vibration research in milling. Chinese Journal of Aeronautics, 32(2), 215-242.

4. Morales Méndez, J. D., & Rodriguez, R. S. (2017). Total productive maintenance (TPM) as a tool for improving productivity: a case study of application in the bottleneck of an auto-parts machining line. The International Journal of Advanced Manufacturing Technology, 92, 1013-1026.

5. Abele, E., Altintas, Y., & Brecher, C. (2010). Machine tool spindle units. CIRP annals, 59(2), 781-802.

6. Zhang, X., Zhang, J., Zhang, W., Li, J., & Zhao, W. (2018). A non-contact calibration method for cutter runout with spindle speed dependent effect and analysis of its influence on milling process. Precision Engineering, 51, 280-290.

7. Li, H. Z., & Li, X. P. (2005). A numerical study of the effects of cutter runout on milling process geometry based on true tooth trajectory. The International Journal of Advanced Manufacturing Technology, 25, 435-443.

8. Soshi, M., Ishii, S., & Yamazaki, K. (2012). A study on the effect of rotational dynamic characteristics of a machine tool spindle drive on milling processes. Procedia CIRP, 1, 319-324.

9. Matsumura, T., & Tamura, S. (2017). Cutting force model in milling with cutter runout. Procedia CIRP, 58, 566-571.

10. Cifuentes, E. D., García, H. P., Villaseñor, M. G., & Idoipe, A. V. (2010). Dynamic analysis of runout correction in milling. International Journal of Machine Tools and Manufacture, 50(8), 709-717.

11. Fu, Z., Yang, W., Wang, X., & Leopold, J. (2016). An analytical force model for ball-end milling based on a predictive machining theory considering cutter runout. The International Journal of Advanced Manufacturing Technology, 84, 2449-2460.

12. Hekman, K. A., & Liang, S. Y. (1997). In-process monitoring of end milling cutter runout. Mechatronics, 7(1), 1-10.

13. Li, Z. L., & Zhu, L. M. (2014). Envelope surface modeling and tool path optimization for five-axis flank milling considering cutter runout. Journal of Manufacturing Science and Engineering, 136(4), 041021.

14. Wang, J. J. J., & Liang, S. Y. (1996). Chip load kinematics in milling with radial cutter runout. Journal of Manufacturing Science and Engineering, 118(1): 111-116.

15. Usop, Z., Sarhan, A. A., Mardi, N. A., & Abd Wahab, M. N. (2015). Measuring of positioning, circularity and static errors of a CNC Vertical Machining Centre for validating the machining accuracy. Measurement, 61, 39-50.

16. Attanasio, A. (2017). Tool run-out measurement in micro milling. Micromachines, 8(7), 221.

17. Isik, Y. (2010). An experimental investigation on effect of cutting fluids in turning with coated carbides tool. Journal of Mechanical Engineering, 56(3), 195-201.

18. Andrews, J. (1977). Edge of the anvil: a resource book for the blacksmith. Intermediate Technology Publications, 147-153.

19. Tominaga, J., Wakimoto, K. Y., Mori, T., Murakami, M., & Yoshimura, T. (1982). Manufacture Of Wire Rods With Good Descaling Property. Transactions of the Iron and Steel Institute of Japan, 22(8), 646-656

ENGINEERING PERSPECTIVE

Research Paper
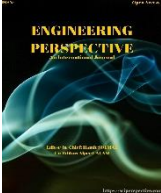
Multivariate Insights into SDIM: Understanding the Effects of Different Elements in Slope Analysis

Edson da Graça M.Cumbe[1,2] (iD), Crimildo Maria A. Sitoe[2] (iD) Marc Nshimiyimana [1] (iD),

Angelo A. Pascoal[3] (iD) , Joel Kironde[4] (iD), Philemon Niyogakiza[1] (iD)

[1]School of Civil Engineering / Southeast University, Nanjing,210096, China-China
[2] Department of Civil engineering, Université saad Dahaleb, Blida- Algeria
[3]Civil Engineering research team, S-Soiltech Consultoria & Services,Lda, Maputo-Mozambique
[4]School of transportation engineering at Southeast University, Jiangsu province, Nanjing – china

ABSTRACT

Slope stability analysis is a critical component of geotechnical engineering, with its implications reaching far and wide, from infrastructure development to environmental management. This study delves into the innovative Stress Deviator Increasing Method (SDIM) and its implications for slope analysis, focusing on the interaction of various components in this intricate process. This study acknowledges the evolution of slope stability analysis, transitioning from traditional methods such as the Limit Equilibrium Method (LEM) to modern approaches, and introduces SDIM as a promising alternative. Bouzid's SDIM combines the Finite Element Method (FEM) with Mohr's circles to offer a comprehensive understanding of slope behavior, particularly under complex stress conditions. The study meticulously examines SDIM's application through the S4DINA (soil stability study by Stress Deviator Increasing using Numerical Analysis) program, highlighting parameter sensitivity and the significance of considering specific conditions. The results underscore the sensitivity of SDIM to certain parameters, including the associated flow rule, finite element number, and embankment with or without foundations. Careful application of SDIM enhances the accuracy of slope stability assessments, allowing for more reliable results. This study represents a significant step in the field of geotechnical engineering, offering a dynamic and comprehensive approach that can address a wide range of scenarios and enhance the reliability of slope stability assessments.

Keywords: Condition Number; FEM; Parameter Sensitivity; SDIM; Slope Stability Analysis; S[4]DINA

1. Introduction

Slope stability analysis stands as a cornerstone within the field of geotechnical engineering, marked by its continuous evolution and the development of diverse analytical methodologies. Over time, methods such as Bishop's circular slip analysis, the limit equilibrium (LE) approach, and the comprehensive framework introduced by Morgenstern and Price have significantly advanced our understanding of slope behavior [1-4]. In this dynamic landscape of analytical techniques, the Stress Deviator Increasing Method (SDIM) emerges as an innovation, proposed by Djillali Amar Bouzid. SDIM represents a novel integration of the Finite Element Method (FEM) with the geometric elegance of Mohr's circles. In contrast to traditional methods, SDIM transcends mere

numerical computation; it orchestrates a comprehensive analysis of stress evolution within a slope. Guided by Mohr's circle principles, SDIM iteratively increases the mobilized principal stress deviator, affording a nuanced understanding of the progression from equilibrium to failure.

SDIM is an innovative approach for slope stability analysis, particularly in calculating the Factor of Safety (FOS)[5]. Unlike traditional methods, which rely on simplifications and predefined failure surfaces, SDIM employs an incremental stress deviator increase to model slope behavior more realistically. This dynamic approach accounts for complex geometries and varying soil conditions, resulting in a more accurate assessment of slope stability. SDIM, as a dynamic and comprehensive method for

slope stability analysis, considers factors like stress deviator increment and material properties continuously it is well-suited for complex slopes and offers a more realistic assessment of stability compared to traditional LEM, which relies on simplified assumptions and predefined failure surfaces. LEMs may provide conservative estimates of stability but may not capture complex conditions as effectively. The choice between SDIM and LEMs depends on specific analysis needs and available resources.

A novel approach SDIM for slope stability analysis, offers a mechanistic, comprehensive, and adaptable method that emphasizes a continuous evaluation of stress and deformation within the slope. This approach contrasts with traditional methods like SRM and is well-suited for complex, heterogeneous soil conditions[6]. However, other techniques like FEM, FELA, and FDEM have their strengths, with varying capabilities to handle complexity and parameter interactions[7,8]. SDIM behaves uniquely by incrementally increasing the stress deviator within the slope, continuously monitoring failure development without predefined surfaces, and dynamically identifying critical slip surfaces. FEM is applied to analyze slope stability problems and serves as the foundation for Bouzid's new method. FEM breaks down the problem domain into discrete elements, uses polynomial functions within each element, and leverages functional analysis to ensure optimal solutions within finite-dimensional sub-spaces[9-11]. This versatile technique is crucial for tackling complex differential equations in various fields, including slope stability analysis.

This study introduces the innovative SDIM, which combines FEM with Mohr's circles to provide a more detailed and precise understanding of slope behavior under complex stress conditions. The research meticulously examines the sensitivity of SDIM to critical parameters and highlights the importance of considering specific conditions in its application. Furthermore, the study emphasizes that the careful use of SDIM can significantly enhance the accuracy and reliability of slope stability assessments. By integrating SDIM with advanced software tools like S^{4}DINA, this research offers a versatile and dynamic approach to slope stability analysis, capable of addressing a wide range of scenarios and enhancing the precision of geotechnical engineering practices. Overall, this study's findings mark a substantial advancement in the field, promising to revolutionize our approach to understanding and predicting slope behavior while contributing to safer and more reliable construction practices.

2. Materials and methods

2.1. Materials

Table 1 functions as a detailed inventory of the carefully chosen materials essential to our study's execution. These materials constitute the bedrock of our research, serving as the basis for our investigations and analyses. This table offers clarity and a convenient reference for comprehending the core components central to our research endeavors. Each material has a specific purpose, whether as input parameters, analytical tools, or data sources and is pivotal to achieving our research objectives. Through Table 1, readers can gain insights into the diverse array of materials that underlie our study, enabling a deeper grasp of our

methodology, processes, and the diverse elements contributing to our research findings.

Table 1. Soil Parametric

Parametric	Symbol
Friction Angle	φ °
cohesion	C'
Dilatancy Angle	Ψ'
Young Modulus	E'
Poisson ratio	ν'
Volumic weigh	γ'

Our research harnessed a suite of carefully chosen software tools, each serving a specific purpose in our comprehensive analysis of slope stability. Rocscience Slide 6.0 established a traditional benchmark for the factor of safety assessments using LEM [12,13]. Tecplot visually depicted plastic zones and stress contours, enriching our comprehension of slope behavior [14]. S^{4}DINA took center stage, conducting finite element analyses with the Stress Deviator Increasing Method (SDIM), introducing a modern and nuanced approach to slope stability assessment. Origin Pro facilitated data visualization and interpretation [15]. These software tools collectively formed the basis of our research, allowing for a thorough analysis of slope stability, encompassing traditional LEM assessments and innovative SDIM applications. Through their integration, we conducted a comprehensive exploration of slope stability, offering analytical flexibility and compatibility with established techniques. The model profile used for evaluation was precisely represented, ensuring fidelity to the configurations integrated into the S^{4}DINA framework, and eliminating potential discrepancies in model depiction.

Case 1: we conducted an in-depth examination of a profile characterized by the presence of sliding surfaces within its foundation. The profile's comprehensive description is visually presented in a pictorial representation, highlighting the key measurements and parameters that have been meticulously taken into account for this analytical investigation.
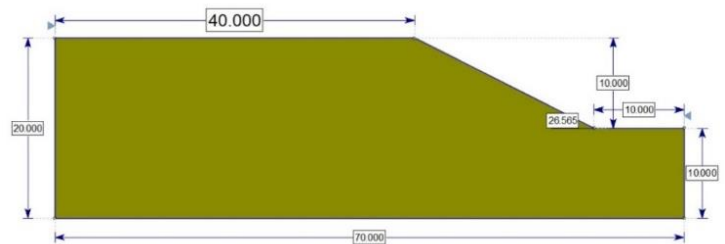
Figure 1. Embankment with foundation layer.

Case 2: In Case 1, a pivotal phase involves the deliberate exclusion of the foundation, thereby facilitating a focused investigation into the inherent characteristics of the slope itself. The selected profile for this analytical segment has been thoughtfully chosen to serve as a guiding framework for our analyses. This strategic selection ensures a comprehensive exploration of the disassembled constituents within the project,

thereby enhancing our grasp of the complex interplay among various elements.
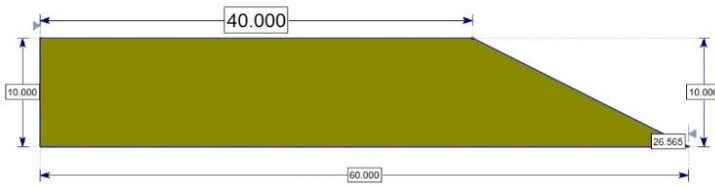
Figure 2. Embankment without foundation Profile.

We aim to gain a comprehensive understanding of the complex factors affecting slope stability by breaking it down into its fundamental components. This refined approach offers nuanced insights and robust assessments of stability conditions. In the context of S⁴DINA, we'll employ two separate input files for the slope profiles—one with a foundation and one without. Analytical tasks within S⁴DINA will be executed using the MSDV COMPILER, accommodating both associated and non-associated studies based on the parameter psi.

2.1.1. Analysis of input parameter influence

The comparative analysis between the LEM and the SDIM involves assessing calculation and deformation parameters to understand their impact on the actor of safety values. While Slide 6.0 yields consistent results, S⁴DINA exhibits variability due to parameter sensitivity. The analysis aims to uncover the interaction among these parameters, shaping computed factor of safety values and enhancing our understanding of both methodologies. Two categories are examined: Calculation Parameters, including Interaction Number and Number of Finite Elements, and Deformation Parameters. The Interaction Number dictates convergence iterations, and the Number of Finite Elements defines spatial discretization. This analysis is crucial for robust stability assessments.

2.1.2. Iteration number slope with foundation and without foundation.

Table 2, Table 3, Table 4, and Table 5 provide insights into the influence of iteration count on the factor of safety within the context of the three primary methods highlighted in this research. These tables present valuable data illustrating how variations in iteration count affect the stability assessment outcomes, shedding light on the performance of each method. The analysis of these tables underscores the significance of iteration count as a critical parameter in slope stability assessments, offering a clearer understanding of the sensitivity and behavior of the methods examined in this study.

Table 2. Associated flow rule with foundation

N⁰ Interaction	Bishops	Morgenstern and Price	Bouzid (SDIM)
100	0.999	0.997	0.957
200			0.979
300			0.989
400			0.990
500			0.991
600			0.991
700			0.991
800			0.991
900			0.991
1000			0.992
1100			0.992
1200			0.992
1300			0.992
1400			0.992

Table 2 conducts a comprehensive analysis of the impact of the number of iterations on a factor of safety values in three methods: LEM, Bishop's method, Morgenstern and Price's method, and SDIM. The study explores the intricate relationship between convergence behavior and the factor of safety through systematic experimentation. It highlights that more iterations enhance result precision but should be balanced with computational efficiency to avoid unnecessary analysis duration.

Table 3. Non -Associated flow rule without foundation

N⁰ Interaction	Bishops	Morgenstern and Price	Bouzid(SDIM)
100	0.999	0.997	0.914
200			0.914
300			0.938
400			0.949
500			0.951
600			0.953
700			0.954
800			0.955
900			0.956
1000			0.957
1100			0.958
1200			0.959
1300			0.959
1400			0.959
1500			0.959

Table 3 subtle change in the factor of safety when considering plasticity assumptions, demonstrating the effectiveness of SDIM method under specific conditions. Both methods show promise, with Bouzid's method standing out. The study emphasizes the importance of iteration count in SDIM, suggesting a higher count for stability. In contrast, the Limit Equilibrium Method produces consistent results. The findings emphasize the need for careful parameter selection in geotechnical analysis and offer practical insights for real-world engineering applications, enhancing our understanding of these methods.

2.1.3. Iteration count and slope analysis without foundation

The study explores the impact of the iteration count on the factor safety in slope stability analyses. Starting with 100 iterations, a consistent trend of underestimating factor of safety values is observed due to the complex geometry. Limited iterations can hinder convergence, leading to imprecise results, evident in non-convergence indicators. Additionally, when assuming an associated flow rule, SDIM and LEM yield similar factors of safety values, indicating convergence towards comparable outcomes under this rule.

Table 4. Associated flow rule without foundation

N⁰ Interaction	Bishops	Morgenstern and Price	Bouzid (SDIM)
100	0.989	0.984	0.949
200			0.969
300			0.978
400			0.982
500			0.983
600			0.985
700			0.985
800			0.986
900			0.986
1000			0.986
1100			0.987
1200			0.987
1300			0.987
1400			0.987
1500			0.987

Table 5. Non-Associated flow rule without foundation

N⁰ Interaction	Bishops	Morgenstern and Price	Bouzid (SDIM)
100	0.989	0.984	0.914
200			0.924
300			0.928
400			0.929
500			0.931
600			0.933
700			0.936
800			0.938
900			0.938
1000			0.938
1100			0.938
1200			0.938
1300			0.940
1400			0.940
1500			0.940

In contrast, using a non-associated flow rule results in a distinct pattern. SDIM's factor of safety significantly differs from that of LEM, indicating the substantial impact of the flow rule choice. The non-associated flow rule appears to reduce soil resistance, leading to a notable deviation in the factor of safety from LEM.

This study emphasizes the critical role of iteration count and flow rule assumptions in shaping factors of safety outcomes. It underscores the need for a careful approach when determining iteration counts and considering flow rule assumptions, essential for accuracy and reliability in slope stability analysis. The findings highlight the intricate relationship between numerical parameters and geotechnical behavior.

2.2. Iterative method

Iterative methods are numerical techniques used for approximating solutions to mathematical problems, particularly in solving linear systems of equations or finding equation roots. They work by starting with an initial guess and iteratively refining it using specific algorithms until predefined termination conditions are satisfied. These methods are widely applied in mathematics, physics, engineering, and computer science, particularly for large-scale problems and systems of equations, offering advantages in memory efficiency and computational speed over direct methods. They are memory-efficient as they rely on matrix-vector and vector-vector products, reducing memory usage compared to direct methods. The choice of iterative method depends on the properties of the matrix[16]. Preconditioners, like Richardson's method, are often used to improve convergence by introducing a matrix B into the equation. Optimal preconditioners, known as multi-level preconditioners, ensure convergence independently of mesh resolution by creating a hierarchy of matrix A representations and accelerating convergence using coarser representations and interpolation and prolongation operations.

To enhance convergence, preconditioners are commonly used. In Richardson's method, a preconditioner matrix B is introduced, and the equation becomes[17]:

$$x_{k+1} = x_k + B^{-1}(b - Ax_k). \tag{1}$$

Ideally, B should be a good approximation to A, and computing B^{-1} should be more efficient than computing A^{-1}.

2.2.1. Stress deviator increasing method

SDIM, or the Stress Deviator Increasing Method, is a remarkable approach to slope stability analysis. It sets itself apart by gradually increasing the mobilized principal stress deviator within the soil mass, replicating the progressive loading and deformation of slopes under changing stress conditions. This method offers a more realistic and comprehensive insight into slope behavior, particularly in complex scenarios, enhancing the accuracy of slope stability assessments. SDIM introduces an innovative finite element procedure for assessing slope stability in geotechnical engineering. It focuses on calculating the critical factor of safety, utilizing Mohr's circles uniquely to broaden the consideration of stress conditions. SDIM capitalizes on the linearity of the Mohr-Coulomb criterion, incrementally increasing the stress deviator to simulate slope failure conditions based on a non-convergence criterion. This approach integrates stress analysis, numerical iteration, and linearity, offering the potential to provide deeper insights into slope behavior and failure mechanisms under varying stress scenarios. In essence, SDIM has

the promise to advance our understanding and prediction of slope behavior in geotechnical engineering.

Bouzid's perspective introduces a foundational equation that is central to the analytical evaluation of the Factor of Safety (FOS) in geotechnical engineering. This equation serves as a fundamental framework for assessing slope stability and allows geotechnical engineers to calculate the FOS, a critical parameter for ensuring the safety and stability of earth structures

$$FOS_{SDIM}^{sp} = \frac{2c}{D_0 cos\phi} + tan^2\phi \left(\frac{S_0}{D_0 sin\phi} - 1\right) \qquad (2)$$

For a purely cohesive soil, the analytical expression of FOS_{SDIM}^{sp} is

$$FOS_{SDIM}^{sp} = 2c/D_0 \qquad (3)$$

where c and ϕ are the effective soil strength parameters, S_0 and D_0 stand respectively for the mobilized principal stress deviator and principal stress sum, FOS_{SDIM}^{sp} is the factor of safety at stress point[18].

2.2.2. Evolution of slope stability analysis

SDIM is a ground-breaking numerical technique revolutionizing slope stability assessment by gradually increasing the stress deviator until failure occurs, capturing dynamic slope failure. It marks a significant shift from traditional LEM to the more versatile FEM [19]. Bouzid's recent research marks a significant advancement in applying the Finite Element Method (FEM) to handle complex stress distributions with enhanced detail and accuracy. This pioneering work led to the development of the Stress Deviator Increasing Method (SDIM), a transformative approach in slope stability analysis. A notable aspect of SDIM is the Mohr's circle expansion factor, which serves as a global indicator of slope stability, particularly valuable when convergence is not achieved. Detailed equations for this factor are provided, and the S[4]DINA program is introduced for the or SDIM application. The reliability and accuracy of SDIM are rigorously assessed through comprehensive comparisons with established methods such as the Simplified Bishop's Method (SRM) and LEM [20]. This work signifies a transformative advancement in slope stability analysis, offering a more dynamic and precise approach.

2.2.3. Condition number

The condition number in numerical analysis measures a mathematical function's sensitivity to changes in its input data, indicating how much the output varies with small input perturbations [21,22]. A low condition number signifies a well-conditioned problem, where input errors have minimal impact on output accuracy. Conversely, a high condition number indicates an ill-conditioned problem, making it challenging to find accurate solutions due to heightened sensitivity to input variations. This concept applies not only to linear algebra but also to nonlinear

functions, as seen in areas like linear regression. In computational fields like FEM[23], where matrices governing discretized systems can exhibit poor conditioning, understanding the condition number is crucial for selecting appropriate solvers and preconditioners to ensure numerical stability and precision in simulations.

A general theory of condition numbers was developed by Rice (1966). The most well-known example of a condition number is the condition number of a non-singular square matrix A, which is

$$cond(A) = \| A \| \cdot \| A - 1 \| \qquad (4)$$

2.2.4. Use of finite element method

Bouzid's Stress Deviator Increasing Method (SDIM) employs the Finite Element Method (FEM). Unlike Bishop and Morgenstern-Price methods, SDIM leverages FEM's capability to handle complex stress distributions and interactions in a more comprehensive manner [24,25].

2.2.5. Factor of safety determination

The Bishop method calculates a global factor of safety for the entire slope failure surface. Morgenstern and Price Method Similar to Bishop's method, Morgenstern and Price's approach also calculates a global factor of safety, but with variations in inter-slice forces accounted for [26,27]

2.2.6. Mohr's circle expansion factor

SDIM introduces the cons of Mohr's circle expansion factor, which controls the expansion of Mohr's circles and represents the slope stability factor [5,18]. This factor is utilized when SDIM's iterative process fails to converge.

2.2.7. Precision and accuracy

The Stress Deviator Increasing Method (SDIM), employs the Finite Element Method (FEM) for more precise and detailed stress distribution analysis in slope stability assessments. This approach offers a more comprehensive understanding of slope behavior under varying stress conditions compared to the simplified assumptions of traditional methods like Bishop and Morgenstern-Price. The key distinction lies in the methodological approach, with SDIM using FEM to provide a more accurate analysis of slope stability, especially regarding stress distribution and failure mechanisms [28]. This method aims to maintain consistent stress levels and local factors of safety throughout the analysis by keeping mobilized normal stress and slip orientation identical in equilibrium and failure states. This is achieved by incrementally bringing the mobilized Mohr's circle to the point of failure through alignment with the failure envelope.
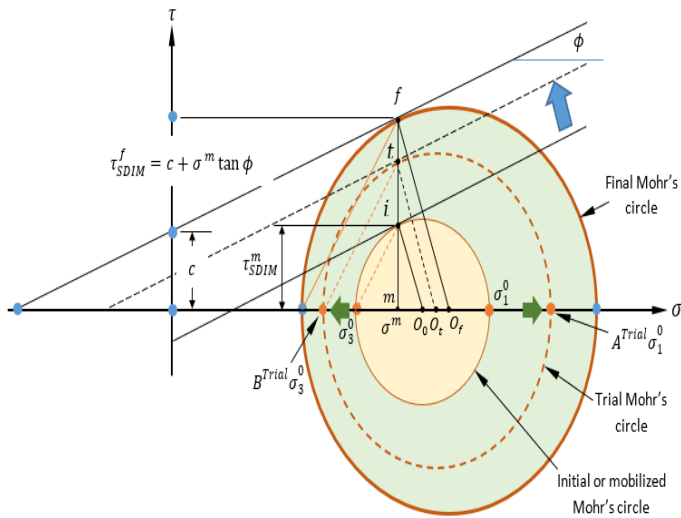
Figure 3. Evolution of principal stresses in the Stress Deviator Increasing Method (SDIM)[18].

Bouzid's method is significant as it provides a clear representation of stress distribution and safety considerations throughout the analysis, aiming for an accurate portrayal of slope behavior under varying stress conditions. It focuses on the mobilized principal stress deviator, enhancing our understanding of slope failure mechanisms. The efficacy of SDIM was confirmed through a comprehensive comparison with established slice methods, evaluating slope stability and safety. The results indicated that Finite Element Analysis closely matched results from the traditional LEM for slope stability assessment, including both associated and non-associated cases. Bouzid's work has the potential to advance geotechnical engineering practices and contribute to the field's development. Therefore, the accuracy of FOS_{SDIM} depends obviously on the accuracy of FOS_{SDIM}^{sp} as can be seen in Eq. (5).

$$F^{Trial} = \min(FOS_{SDIM}^{SP}) \qquad (5)$$

3. Results and Discussion

3.1. Analysis of plastic zones and stress contours

This section shifts its focus towards an examination of plastic zones and stress contours in the context of slope stability, utilizing the innovative SDIM. The visualization and analysis are facilitated by Tecplot, a versatile data visualization tool[29]. The primary goal is to scrutinize the plastic zones and stress contours resulting from SDIM while considering various input parameters. These parameters are used in conjunction with data extracted from the S⁴DINA report file, which is then transformed into a compatible format for Tecplot. The visualization involves two scenarios: slopes with and without foundations, providing insights into how foundations impact plastic deformation and stress distribution. By comparing these scenarios, the study seeks to uncover the nuanced dynamics of plastic deformation zones and stress distribution in slope stability assessment. This analysis not only enhances comprehension of the SDIM method but also

contributes to a broader understanding of geotechnical factors governing slope behavior and stability.

At this point, it becomes clear that the subtle slip lines are beginning to appear near the base of the slope, and there's an initial deformation pattern emerging. However, it's important to emphasize that this early deformation might lead engineers to a premature conclusion that the failure process has been initiated. In actuality, this perception can be misleading, mainly because there is no convergence at this particular stage of the analysis. The ongoing deformation process has not yet reached a critical and significant state.
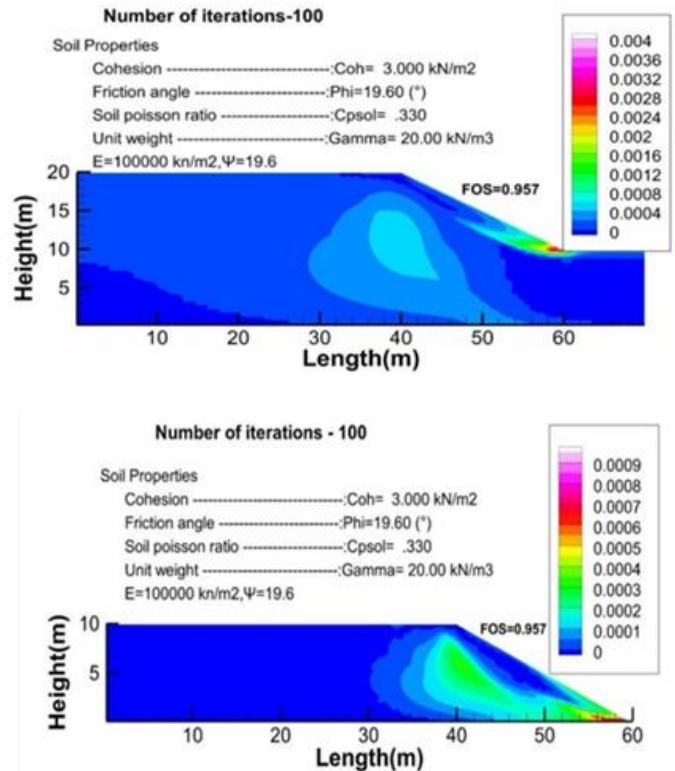

Figure 4. Strain contours corresponding to the step of failure for 100 iterations. With associated flow rule.

Upon reaching the 1000th iteration, a notable achievement was made: convergence was attained. At this stage, the calculated factor of safety reached an acceptable level, signifying a stable and reliable outcome. It's important to emphasize that even with a subsequent increase in the iteration count, negligible alterations were expected in the results. The reason for this lay in the fact that the failure process had already been initiated and was well underway. Therefore, beyond this point, there was no compelling need to continue escalating the number of iterations. The convergence achieved at the 1000th iteration ensured that the analysis had appropriately captured the critical dynamics of the slope stability scenario. Further increasing the iteration count would have yielded diminishing returns in terms of result accuracy, as the significant phase of failure progression had already commenced. This underscored the importance of selecting an appropriate number of iterations to strike a balance between

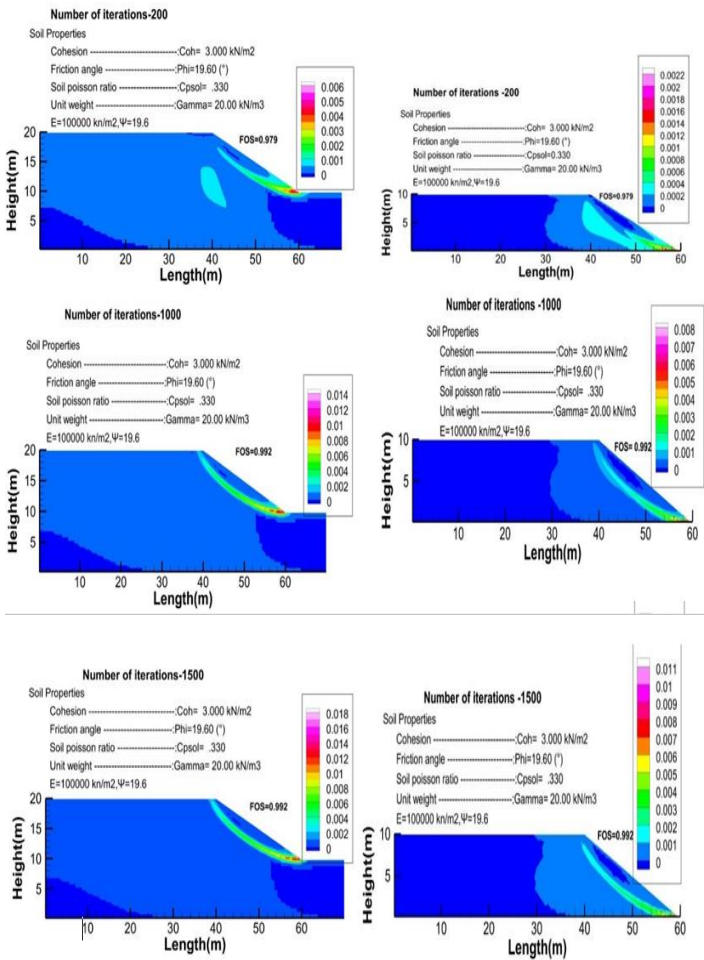computational efficiency and capturing accurate deformation behavior.

Figure 5. Strain contours corresponding to the step of failure for 200 to 1500 iterations.

In the realm of the non-associated flow rule, early iterations reveal a lack of resistance in the slope, emphasizing the importance of considering the dilatancy angle in these analyses. However, as iterations progress, stress concentration around the slope's toe increases, and slip lines become more defined. This highlights the effectiveness of SDIM, with clear and smooth contours showcasing its capabilities. When combined with other approaches, it provides geotechnical engineers with enhanced judgment and insight into slope analysis, facilitating a deeper understanding of slope behavior and informed decision-making in geotechnical engineering.
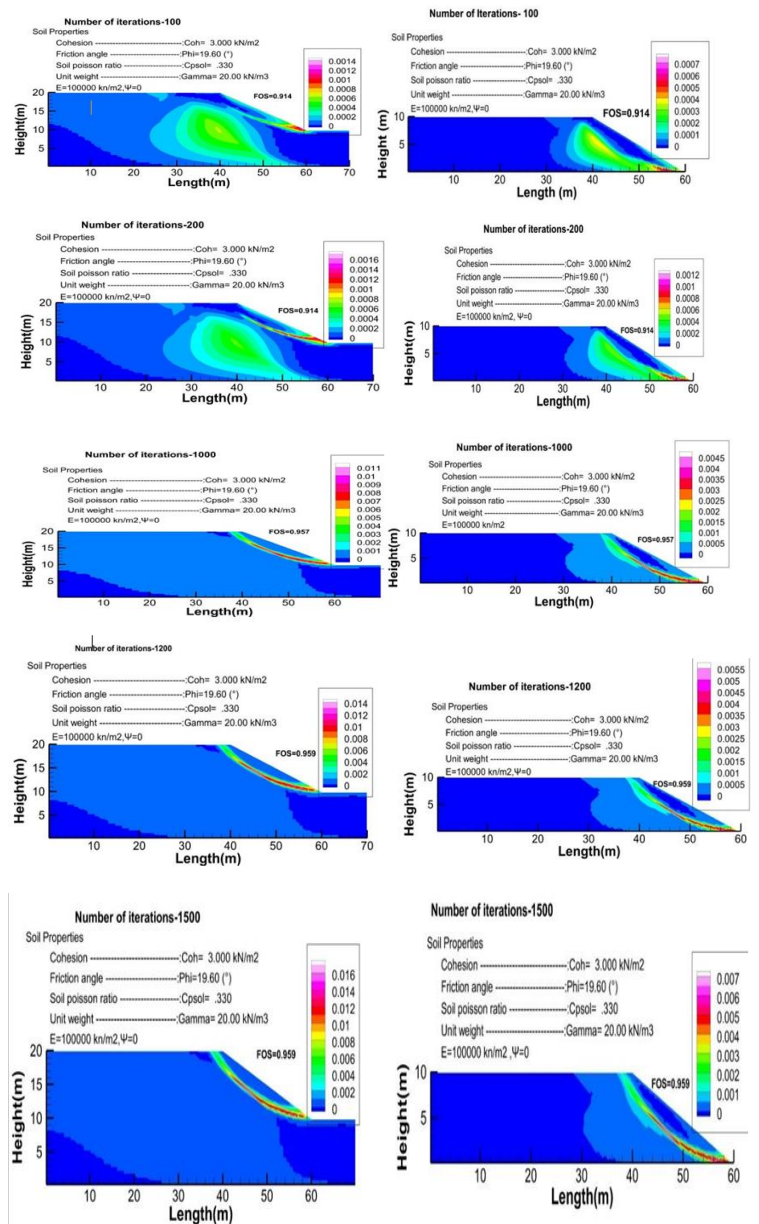

Figure 6. Strain contours corresponding to the step of failure for 100 to 1500 iterations, with Non-associated flow rule.

3.2. Evaluation of the influence of finite element count

In this study, we've investigated the impact of varying the number of finite elements on a factor of safety calculations. Finite elements are crucial in numerical simulations, breaking down complex domains into manageable segments. Adjusting the number of finite elements refines the analysis granularity. More elements create a finer mesh, improving accuracy in stress and deformation predictions, and directly influencing the factor of safety. However, a balance is needed to avoid excessive computational demands or oversimplification. Systematically varying element counts helped identify a convergence point, indicating stable and consistent results. This analysis provides valuable insights into the reliability and robustness of our numerical approach.

It becomes evident that with a lower number of finite elements, the factor of safety is prone to overestimation. Ensuring an appropriate and adequate number of finite elements becomes pivotal in achieving a factor of safety values that faithfully represent the true state of the studied case. Striking the right balance in selecting the number of finite elements is crucial for a reliable and precise analysis outcome. This equilibrium ensures that the numerical solution captures the intricate interactions and behavior within the slope system while avoiding unnecessary computational complexities or oversimplifications that might skew the results."
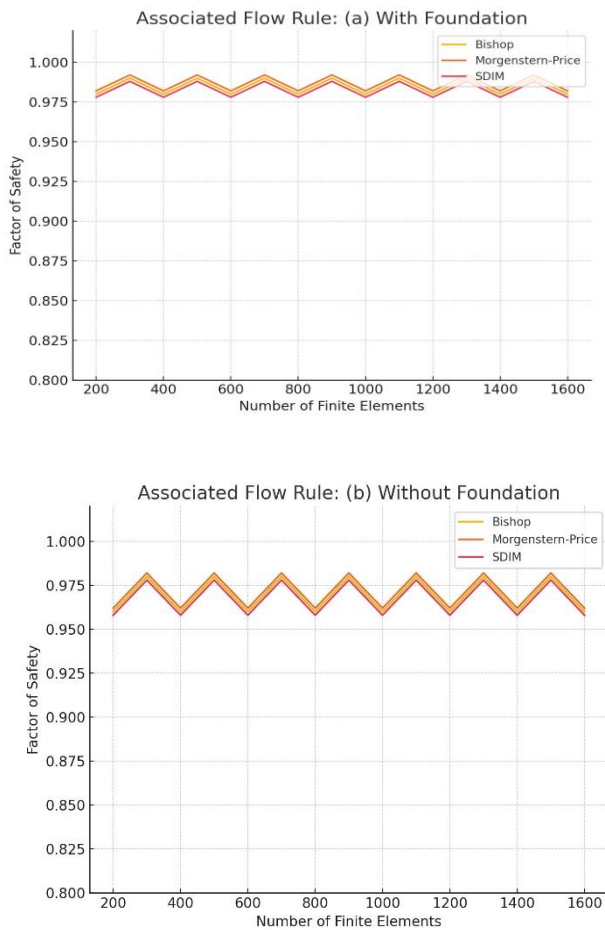

Figure 7. Comparison of factor of safety versus the number of finite elements for the associated flow rule. (a) With foundation and (b) without foundation. (Parameters: γ = 20 KN/m², φ = 19.6°, c = 3 KPa, Poisson ratio = 0.33, E = 100000 KN/m², ψ = 19.6°)
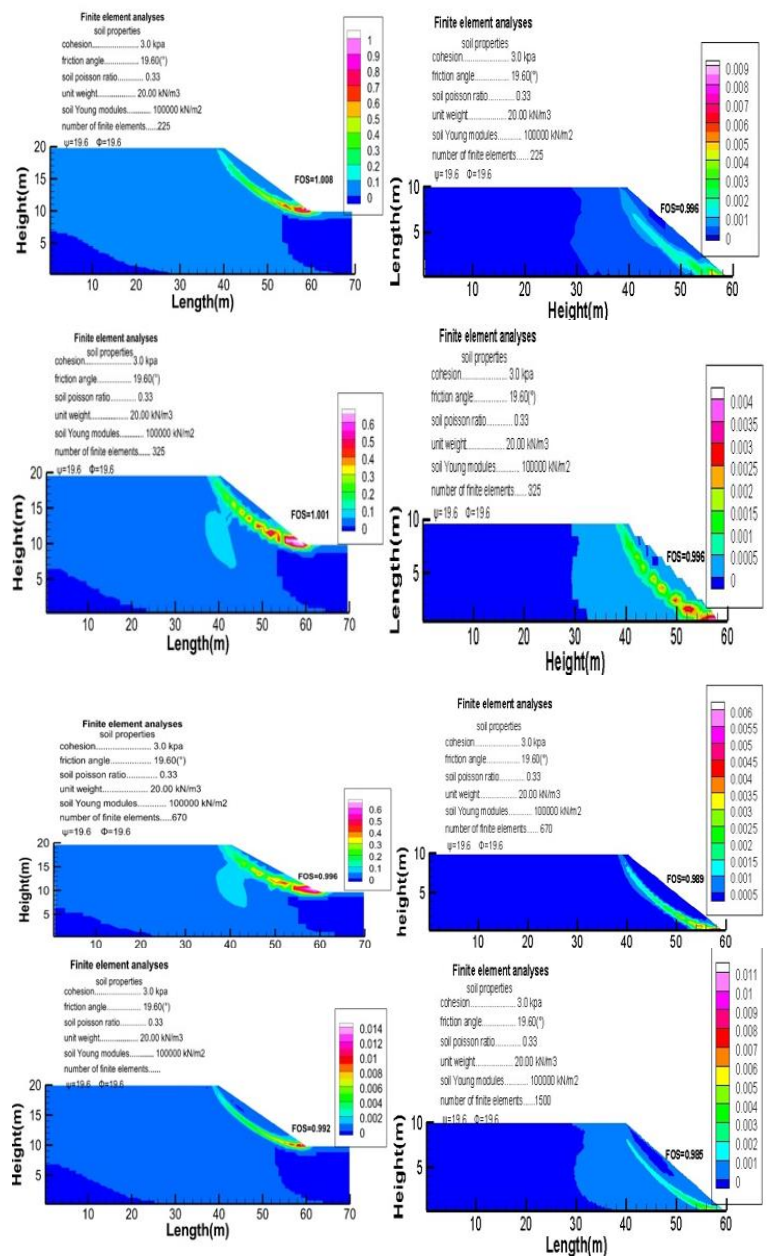

Figure 8. Strain contours corresponding to the step of failure for 225 to 1000, with the foundation

At the 1000th iteration, a significant milestone is reached: convergence is achieved, and the calculated factor of safety becomes stable and reliable. Importantly, further increasing the iteration count is not expected to substantially alter the results because the failure process is already in progress. Therefore, there's no need to continue increasing the number of iterations beyond this point. Convergence at the 1000th iteration ensures that the analysis accurately captures the critical dynamics of slope stability. Selecting the right number of iterations is crucial to balance computational efficiency with accurate deformation behavior, as additional iterations would provide diminishing returns in terms of result accuracy once the significant phase of failure progression has begun.
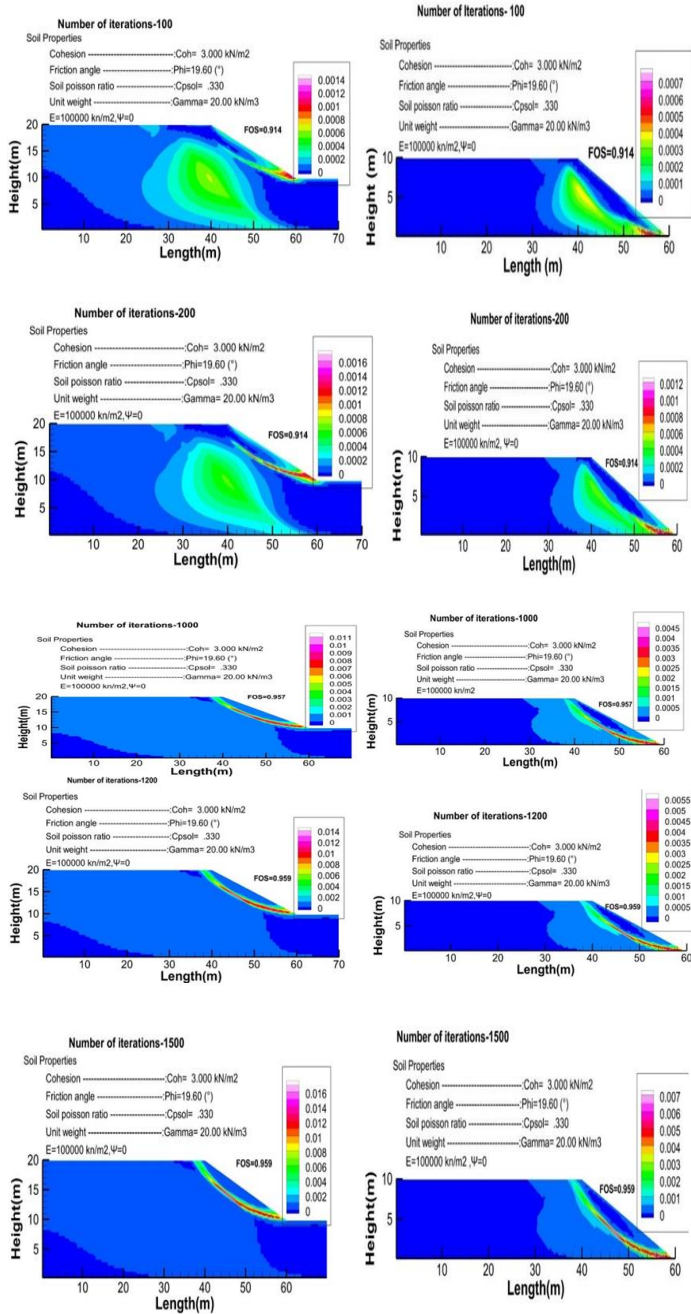
Figure 9. Strain contours corresponding to the step of failure for 100 to 1500 iterations, with non-associated flow rule.

In the non-associated flow rule context, early iterations reveal a lack of slope resistance, emphasizing the role of the dilatancy angle in these analyses. As iterations progress, stress concentration at the slope toe increases, and the slip line becomes more defined, showcasing the effectiveness of Bouzid's method. Clear and smooth contours highlight the approach's capabilities. Integrated with other methods, it enhances geotechnical engineers' judgment and insight for more informed slope analysis. This approach fosters a deeper understanding of slope behavior, aiding decision-making in geotechnical engineering.

This study was conducted under similar conditions, setting ψ (psi) to zero results in a significant decrease in system resistance, leading to distinct deformation that suggests unstable conditions. This highlights the sensitivity of this parameter and its substantial influence on slope behavior. Additionally, varying the number of finite elements during the examination reveals its significant impact on the analysis. A lower count tends to overestimate the factor of safety due to limited detail capture. Incrementally increasing finite elements leads to a convergence of the point, enhancing the factor of safety accuracy and overall precision in slope stability analysis.

4. Conclusion

Slope stability analysis has undergone a significant transformation, transitioning from traditional methods like LEM to modern approaches like SDIM. SDIM, developed by Bouzid, integrates FEM with Mohr's circles to provide a more detailed and precise understanding of slope behavior, particularly under complex stress conditions. This study, which evaluated SDIM's application using the S^{4}DINA program, emphasizes enhancing the potential reliability of slope stability assessments. By addressing the critical need for earth slope stabilization, this research introduces an innovative approach that has the power to revolutionize slope stability analysis and contribute to safer geotechnical engineering practices.

1.   The field of slope stability analysis has witnessed a notable evolution, with traditional methods like the Limit Equilibrium Method (LEM) and modern approaches such as the Stress Deviator Increasing Method (SDIM) playing significant roles.

2.   DIM, integrating the Finite Element Method (FEM) and Mohr's circles, offers a dynamic and comprehensive approach to slope stability analysis. It has the potential to enhance the precision and adaptability of assessments under varying conditions.

3.   Our study underscores the sensitivity of SDIM to specific parameters, such as the associated flow rule, the number of finite elements, and the presence of foundations. These factors significantly influence the outcomes of slope stability analyses.

4.   Careful application of SDIM enhances the accuracy of slope stability assessments, allowing for more reliable results. The consideration of various factors and conditions is pivotal in this process.

5.   The integration of SDIM with S^{4}DINA represents a substantial advancement, providing geotechnical engineers with a valuable and adaptable tool. It enables more precise and reliable slope stability assessments under diverse conditions, ultimately contributing to the safety and reliability of geotechnical engineering projects.

6.   The study's evaluation of SDIM and its integration with the S^{4}DINA software underscores its potential as a game-changing technique for slope stability analysis. This paper contributes to the evolving landscape of geotechnical engineering by offering a fresh perspective and a new tool that can address slope stability concerns with increased precision and reliability.

This study, while valuable, has limitations, focusing on the theoretical aspects of SDIM and S^{4}DINA without field testing or

comprehensive sensitivity analysis. Future research should include real-world testing, broader parameter sensitivity analyses, and integration with advanced geotechnical tools to refine and enhance SDIM's applicability, fostering collaboration between geotechnical engineers and software developers.

Acknowledgment

Conflict of Interest Statement

The authors must declare that there is no conflict of interest in the study.

CRediT Author Statement

Edson da Graça M. Cumbe: Conceptualization, Methodology, Visualization, Writing - original draft, Writing - Review & Editing. **Crimildo Maria A. Sitoe:** Conceptualization, Methodology, Visualization, Writing - original draft, Writing - Review & Editing. **Marc Nshimiyimana:** Writing - review & Methodology. **Philemon Niyogakiza:** Review & Editing. **Joel Kironde:** Review & Editing. **Angelo A. Pascoal:** Review & Editing.

References

1. Krahn, J. (2003). The 2001 RM Hardy Lecture: The limits of limit equilibrium analyses. Canadian Geotechnical Journal, 40(3), 643-660.
2. Rawat, S., & Gupta, A. (2016). Analysis of a nailed soil slope using limit equilibrium and finite element methods. International Journal of Geotechnical Engineering, 2, 1-23.
3. Morgenstern, N. U., & Price, V. E. (1965). The analysis of the stability of general slip surfaces. Geotechnique, 15(1), 79-93.
4. Leshchinsky, B., & Ambauen, S. (2015). Limit equilibrium and limit analysis: Comparison of benchmark slope stability problems. Journal of Geotechnical and Geoenvironmental Engineering, 141(10), 04015043.
5. Bouzid, A., & Djillali, J. (2022). Finite element analysis of slope stability by incrementally mobilizing the mobilized principal stress deviator. International Journal of Geotechnical and Geoenvironmental Engineering, 17(5), 1554-1574.
6. Schermelleh, L., Ferrand, A., Huser, T., Eggeling, C., Sauer, M., Biehlmaier, O., & Drummen, G. P. J. (2019). Super-resolution microscopy demystified. Nature Cell Biology, 21(1), 72-84.
7. Mitchell, J. K., & Kelly, R. J. (2013). Addressing some current challenges in ground improvement. Proceedings of the Institution of Civil Engineers - Ground Improvement, 166(3), 127-137.
8. Ji, J., Zhang, Z., Wu, Z., Xia, J., Wu, Y., & Lü, Q. (2021). An efficient probabilistic design approach for tunnel face stability by inverse reliability analysis. Geotechnical Frontiers, 12(5), 101210.
9. Pranic, M., & Spalević, M. (2019). ETNA25 Recent Advances in Scientific Computation Conference.
10. Martin, S. (2011). Flexible, unified and directable methods for simulating deformable objects. ETH Zurich.
11. Miller, C. T. (2016). Matthew W. Farthing. In The Handbook of Groundwater Engineering (p. 313).
12. Cui, H., Ji, J., Song, J., & Huang, W. (2022). Limit state line-based seismic stability charts for homogeneous earth slopes. Computers and Geotechnics, 146, 104749.
13. Ji, J., Zhang, C., Gui, Y., Lü, Q., & Kodikara, J. (2017). New observations on the application of LS-SVM in slope system reliability analysis. Journal of Computing in Civil Engineering, 31(2), 06016002.
14. Mulahasan, S. (2016). Hydrodynamics of large-scale roughness in open channels. Cardiff University.
15. Moberly, J. G., Bernards, M. T., & Waynant, K. V. (2018). Key feature updates for Origin 2018. Journal of Chromatography, 10, 1-2.
16. Dravins, I. (2023). Preconditioning for block matrices with square blocks. Acta Universitatis Upsaliensis.
17. Benzi, M., Olshanskii, M. A., & Wang, Z. J. (2011). Modified augmented Lagrangian preconditioners for the incompressible Navier–Stokes equations. International Journal for Numerical Methods in Fluids, 66(4), 486-508.
18. Bouzid, A., & Djillali, J. (2022). Finite element analysis of slope stability by expanding the mobilized principal stress Mohr's circles – Development, encoding, and validation. Journal of Rock Mechanics and Geotechnical Engineering, 14(4), 1165-1179.
19. Abramson, L. W., Lee, T. S., Sharma, S., & Boyce, G. M. (2001). Slope stability and stabilization methods. John Wiley & Sons.
20. Chen, Z., & Ugai, K. (2008). Limit equilibrium and finite element analysis—a perspective of recent advances. In Proceedings of the Tenth International Symposium on Landslides and Engineered Slopes. Balkema, Christchurch.
21. Chen, S. (2023). Advanced Computational Methods and Geomechanics. Springer Nature.
22. Cucker, F., Ergür, A. A., & Tonelli-Cueto, J. (2022). Functional norms, condition numbers, and numerical algorithms in algebraic geometry. Forum of Mathematics, Sigma.10; 103.
23. Bonnet, M. (2021). Lecture notes on numerical linear algebra.
24. Bouzid, A., & Djillali, J. (2022). Finite element analysis of slope stability by expanding the mobilized principal stress Mohr's circles – Development, encoding, and validation. Journal of Rock Mechanics and Geotechnical Engineering, 14(4), 1165-1179.
25. Ryan, R. (1996). Working on the boundaries: Philosophies and practices of the design process (Vol. 3642). NASA, Marshall Space Flight Center.
26. Cheng, Y. M., & Yip, C. J. (2007). Three-dimensional asymmetrical slope stability analysis extension of Bishop's, Janbu's, and Morgenstern–Price's techniques. Journal of Geotechnical and Geoenvironmental Engineering, 133(12), 1544-1555.
27. Wright, S. G., Kulhawy, F. H., & Duncan, J. M. (1973). Accuracy of equilibrium slope stability analysis. Journal of the Soil Mechanics and Foundations Division, 99(10), 783-791.
28. Ho, I.-H. (2014). Parametric studies of slope stability analyses using three-dimensional finite element technique: Geometric effect. Journal of Geotechnical and Geoenvironmental Engineering, 9(1), 33-43.
29. Wang, R.-X., Wang, R., Fu, P., & Zhang, J.-M. (2020). Portable interactive visualization of large-scale simulations in geotechnical engineering using Unity3D. Advances in Engineering Software, 148, 102838.

ENGINEERING PERSPECTIVE

Research Paper
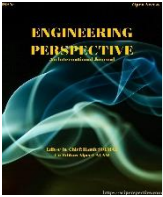
Lightweighting of a Vehicle Steering Uprights via Structural-Based Design and FEA Analysis

Sk Al Nahian Samin[1]*, Sazzad Hossen[1], K M Mahfuzur Rahman[1], Ustab Gosh[1]

[1] *Mechanical and Production Engineering Department, Ahsanullah University of Science and Technology, 141 & 142, Love Road, Tejgaon Industrial Area, Dhaka-1208*

ABSTRACT

In FSAE formula student vehicles, the steering upright connects the wheel and the steering mechanism. Thus, an optimized upright shape is essential for enhancing vehicle efficiency and wheel performance. This study compares aluminum 6061-T6 with titanium alloy 6Al-4V (aged and treated) for upright development, considering materials science, engineering, and innovative design to optimize component weight. The Topology solver optimizes the geometry, such as a vehicle's upright, by considering other design elements. The safety factor of the topology-optimized titanium alloy Ti 6Al-4V model was 2.6237, compared with 1.554 for aluminum 6061-T6. The safety factor for the topology-optimized model improved by 68.737%. The comparison between 6061-T6 and Ti 6Al-4V alloy, where Ti alloy provides the best optical properties and optimizes the design for weight reduction as well as structural integrity. The upright validation aligns with prior efforts, exhibiting a difference of less than 1% from the previous findings. ANSYS Workbench was used to analyze the topology and structure, whereas SolidWorks selected and designed the materials. Simulations revealed only 0.0438% deformation and 0.1272% stress variance from the experimental results. 2D plots, contours, and streamlines show these findings. For the automobile industry and motorsport community, the optimized upright model will reduce the car's weight by 2.56 kg and improve its performance.

Keywords: Stress; Deformation; Weight reduction; Upright; Topology.

1. Introduction

Structural design and upright optimization are necessary to satisfy the requirements of high-performance Formula SAE vehicles. The driving performance, safety, and efficiency depend on the upright role of the suspension system. The structural design allows the upright to handle vertical vehicle weight, lateral cornering forces, and braking loads [1]. Structural analysis helps predict how the upright will perform in real-world situations, including high-speed turning, rapid braking, and rugged terrain. Engineers can model the stress distribution, deformation, and failure locations under specified load situations by using the Finite Element Method [2]. Structural optimization allows engineers to optimize an upright design for performance. Topology optimization, for instance, uses load routes to determine where the material is required and where it can be deleted, making the design more efficient. This is crucial in racing, as every gram of weight reduction improves performance. Advanced materials, such as aluminum alloys and titanium with high strength-to-weight ratios, can be explored using structural analysis [3]. The structural analysis optimizes the material choice to make the upright operate well, manufacturable, and cost-effective. Structural design must also include integrating the upright with suspension components, such as control arms, brake calipers, and wheel hubs [4]. The uprights must sustain these connections without weakening under the strain. The structural analysis confirmed this result[5]. Weight reduction, vibration reduction, and enhanced performance are the key objectives of FSAE project. The Formula Student is a student-driven racing vehicle developed by the Formula Society of Automotive Engineers (FSAE) race. The upright position is a critical

component of the tire assembly through which the suspension components are attached. This portion is crucial because it is perceived as an undisturbed body, despite being subjected to extremely high stress. The equilibrium equation and Hooke's law are vital for mathematically modeling an upright position because they allow for force and stress analyses under loads (Iha et al., n.d.). The equilibrium equation balances all forces and moments on the upright, making it stable and non-accelerating. This is essential for understanding how a Formula SAE (FSAE) car's upright response to turning, braking, and accelerating forces. These requirements must be met in static and dynamic circumstances to distribute the internal stresses equally in an upright position and prevent movement or distortion. However, Hooke's law predicts upright deformation under load by relating the stress and strain in the material [6]. So, σ = E. ε Let σ represent stress, E represent Young's modulus a material property, and ε represents strain. This rule helps engineers to calculate the upward stretch or compression when forces are applied. Hooke's law shows a linear connection between stress and strain up to the yield point of the material for upright-design materials, such as aluminum or titanium. The equilibrium equation balances all forces on the upright, whereas Hooke's law quantifies deformations. To anticipate the stress concentrations and failure locations in FEA models, these two notions are essential. Without these basic rules, upright mechanical behavior cannot be reliably modeled, resulting in faulty designs. Weight reduction is a critical concern in the automotive manufacturing industry. A substantial weight reduction will influence fuel efficiency, emission reduction initiatives, and consequently environmental conservation [7]. Several technological advancements, including developments in materials, methods of design and FEA analysis, fabrication processes, and optimization techniques, can be utilized to reduce weight Manufacturers can decrease fuel consumption by reducing vehicle weight. The properties of a suspension system are contingent on the design specifications and competitive conditions; therefore, automobile design must incorporate an optimized variable-density topology. This may entail modifying the safety factor to reduce mass. The optimized process presented and surmounted engineering obstacles that underscore the significance of adaptability and resilience in the realm of problem solving. The steering upright in a high-performance FSAE vehicle is subjected to dynamic stresses and deformations that mirror the unpredictability of obstacles encountered in numerous engineering endeavors [8]. Design, analysis, and testing exemplify a more comprehensive problem-solving methodology that places importance on perseverance, adaptability, and readiness to acquire knowledge from setbacks. Titanium-6AL-4V was selected for this analysis because of its extensive application in the extrusion of aluminum bars, pipelines, rods, and other similar objects. Additionally, metal extraction from the regions of the components with lower fatigue can potentially result in weight reduction. The results of this study indicate that the redesigned upright position enhances efficiency and reduces tension concentration. To fulfill the requirements, an endeavor was undertaken to substitute Al 6061-T6, steering upright with Titanium-6AL-4V, which features an enhanced upright sign to achieve a superior strength-to-weight ratio. The material possesses sufficient capacity to satisfy the increasing need for robust components in the automotive sector

while undergoing substantial weight reduction compared to conventional methods[9]. This research endeavor was undertaken to redesign the steering upright for the FSAE competition using a material composition consisting of 89.3% Ti, 5.5% Al, Vanadium 4.5% and carbon 0.08%. The primary purpose of upright steering is to facilitate suspension and attachment to the brake caliper, hub, rack, and pinion tie rod and to establish a connection between the chassis and tire via the wishbone. Suspensions for the brake lever, hub, rack, pinion tie rod, and wishbone-assisted connection between the chassis and tire are functions of the upright steering. A computer-aided upright design was fabricated using SolidWorks, and ANSYS was employed to conduct the structural and fatigue analyses.   In recent years, upright steering methods have experienced lap time checks [10].   Wheels and uprights were optimized for stability and performance in racing cars. The upright position of a (FSAE) car must be optimized to achieve perfect vehicle wheels and steering. An exhaustive literature review shows that topological techniques are seldom used in upright design, particularly to improve efficiency [11]. This work uses a topological technique to optimize the upright position of a Formula Student car, meeting a significant gap. To achieve the highest possible stress and low deformation output, this study aimed to optimize the upright position by using the topology method [12]. Additionally, this study aims to ensure high-strength material for optimal wheel performance on a variety of skid pads and racetracks, as well as to improve the strength of the upright and reduce its mass by incorporating high-performance upright designs [13]. With a particular focus on the delicate equilibrium that must be maintained between performance, manufacturing feasibility, and material usage, this research will investigate the challenges that are faced, the concerns that need to be considered, and the adjustments made to achieve these objectives [14].

2. Numerical Analysis

Aluminum 6061-T6 consists mostly of aluminum, with the presence of magnesium, silicon, copper, chromium, zinc, titanium, and ferrous elements, and it has a yield strength of 276 MPa, These materials increase the hardness and enhance the load–absorption capacity. The weight of the car is distributed among the four wheels. An upright system should be able to withstand a load and transmit it to the wheel [15]. To design this system, computer-aided design software, specifically Solid Works, was used. Mesh and node analyses were then performed. Stress analysis was also performed on the upright assembly using the ANSYS Workbench to identify the approximate solutions for the given boundary conditions and constraints. This design analysis has been primarily centered on the optimization of lightweight properties and incorporation of shock-absorbing capabilities, which necessitates the use of rigid materials [16]. Various modifications and alterations, including the implementation of diverse mesh sizes such as 2mm, 3mm, 4mm, 5mm, 6mm and 7mm have been employed to ensure the acquisition of precise data and the development of superior designs for future manufacturing endeavors. Through the strategic deployment of these techniques, the resultant output will undoubtedly yield enhanced outcomes and significantly to the advancement of design methodologies in the industrial landscape

[17]. This facilitates the examination of the upright force absorption capacity, which is briefly illustrated in this design. The forces exerted on the contact surfaces were transmitted through the five nodes of the driver to the corresponding mating surfaces, as shown in. This research evaluates the interconnectedness of various regions. The active presence and formation of contacts within the system were described in detail. The Titanium Alloy -6AL-4V consisted mostly of titanium, with the presence of aluminum, vanadium, and ferrous elements, and had a yield strength of 827.37MPa. This is harder than that of aluminum 6061-T6. The first upright model Z design was completed using aluminum 6061-T6, but the upright design was optimized using titanium 6AL-4V. Titanium is very effective in uprights because of its lightweight and hardness. Titanium can absorb more heat than aluminum and its fatigue failure range is lower [18]. Compare both elements for future development in the car industry to produce high-quality FSAE cars. This study focuses on material strength and design optimization [19]. Depending on the force, component material qualities, and design system, the impact force may have multiple impacts on the upright system.

Mathematical modeling, mechanical behavior and governing Equations:

This section investigates the mathematical modeling of the steering upright, focusing on its load-bearing behavior, stress distribution, and deformation characteristics. The steering upright serves as a crucial structural element that conveys loads from the suspension system to the wheel assembly [20]. The steering upright can be represented through mathematical modeling that draws on the foundational concepts of continuum mechanics, with particular emphasis on linear elasticity theory and finite element analysis (FEA). The fundamental equations that govern the modeling of stress and deformation behavior are established based on principles of equilibrium, relationships between strain and displacement, and the laws governing material properties[21].

Equilibrium Equations:

The equilibrium equations for a three-dimensional solid structure, such as the upright, are derived from the balance between internal stresses and external forces. These may be articulated as Eq. (1), (2) and (3) where,$\partial\sigma_{xx}$, $\partial\sigma_{xy}$, $\partial\sigma_{xy}$ are the components of

$$\frac{\partial\sigma_{xx}}{\partial x} + \frac{\partial\sigma_{xy}}{\partial y} + \frac{\partial\sigma_{xz}}{\partial z} + f_x = 0 \qquad (1)$$

$$\frac{\partial\sigma_{yx}}{\partial x} + \frac{\partial\sigma_{yy}}{\partial y} + \frac{\partial\sigma_{yz}}{\partial z} + f_y = 0 \qquad (2)$$

$$\frac{\partial\sigma_{zx}}{\partial x} + \frac{\partial\sigma_{zy}}{\partial y} + \frac{\partial\sigma_{zz}}{\partial z} + f_z = 0 \qquad (3)$$

the stress tensor and f_x, f_y, f_z are the body forces acting in the x, y, and z directions, respectively.

Constitutive Law (Hooke's Law for Linear Elasticity):

To link the stresses with the strains, applying Hooke's Law, which outlines the behavior of linear elastic materials such as

6061 aluminum and Ti-6Al-4V. In a three-dimensional context, the formulation of Hooke's Law is expressed as

$$\sigma_{ij} = C_{ijkl}\epsilon_{kl} \qquad (4)$$

Eq. (4) σ_{ij} are the components of the stress tensor, ϵkl are the components of the strain tensor and C_{ijkl} are the components of the elasticity tensor, which depends on the material properties like Young's modulus E and Poisson's ratio v.

Hooke's Law simplifies to:

$$\sigma_{xx} = \lambda\left(\epsilon_{xx} + \epsilon_{yy} + \epsilon_{zz}\right)2\mu\epsilon_{xx} \qquad (5)$$

$$\sigma_{xy} = 2\mu\epsilon_{xy} \qquad (6)$$

For Eq. (5) and (6) the materials considered in this study: 6061 Aluminum: E=68.9GPa v=0.33 and Ti-6Al-4V: E=113GPa v=0.34

Formulation of FEA:

This mathematical model of the steering upright uses the finite element technique (FEM) which discretizes the structure into tiny components to approximate stresses and strains under load.

Using linear equations to relate nodal displacements u to applied forces F.

$$ku = F \qquad (7)$$

Eq.(7) Where u is the displacement vector at the nodes of the mesh and F is the force vector representing external forces applied to the upright.

Boundary Conditions and Load Application:
- The finite element analysis model integrates boundary conditions to replicate actual constraints in real-world situations. Regarding the steering upright:
- Boundary conditions are established at the mounting points, where the upright is fastened to the suspension system with bolts.

Analyses of braking, turning, and vertical loads are achieved by applying forces derived from the usual loads seen in Formula Student racing.

2.1. Methodology

The upright of a vehicle function as an essential structural element that links the control arm of the connecting rod to the axle. Alongside the operational design of the connection hole, the emphasis is also placed on the lightweight design of the front upright the upright encountered typical loads linked to Formula Student racing, including braking forces, cornering forces, and vertical loads due to the vehicle's weight. In Table 1 the forces applied were based on empirical data collected from previous Formula Student events, ensuring that the analysis truly represents real-world conditions[22]. Figure 1 describes the FEM methodology with graphical circle.

Table 1. Model Z Material Properties

Property	6061- T6 Aluminum
Density (g/cm³)	2.7
Tensile Strength (MPa)	310
Yield Strength (MPa)	276
Young's Modulus (GPa)	68.9
Poisson's Ratio	33

Figure 1. FEM Method optimization approach and steps

2.2. Upright position geometry

A Formula SAE car's upright links the wheel assembly to the suspension arms and is crucial. Its geometry holds the hub, bearings, brake caliper, upper and lower control arms, tie rod, and occasionally the shock absorber. The upright is compact and asymmetric to save weight and increase strength. The geometry Figure 2. must align the wheel and maintain camber, toe, and caster angles for optimal handling. It includes vertical and lateral load channels for equal stress distribution. For lightweight, high-performance designs materials are employed with topology optimization to eliminate unnecessary material.

2.3. Mesh and grid independency test

To make sure the FEA findings are valid and not affected by the mesh size, Figure 3. a mesh independence test is necessary for the steering upright. While a finer mesh enhances the solution's correctness in finite element analysis (FEA), going overboard with the fineness might increase processing expenses without enhancing the results at all. A mesh independence test may help find the sweet spot for mesh size when more refinement has no effect on important metrics like stress and displacement[23].
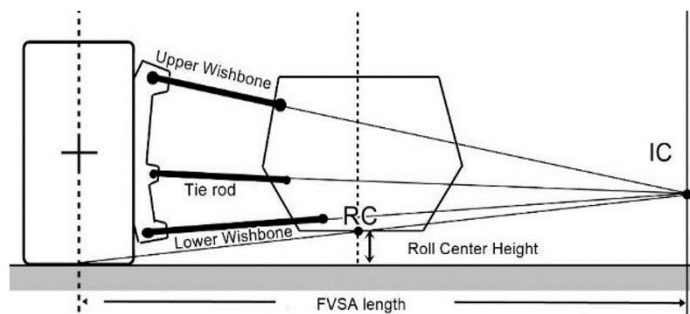

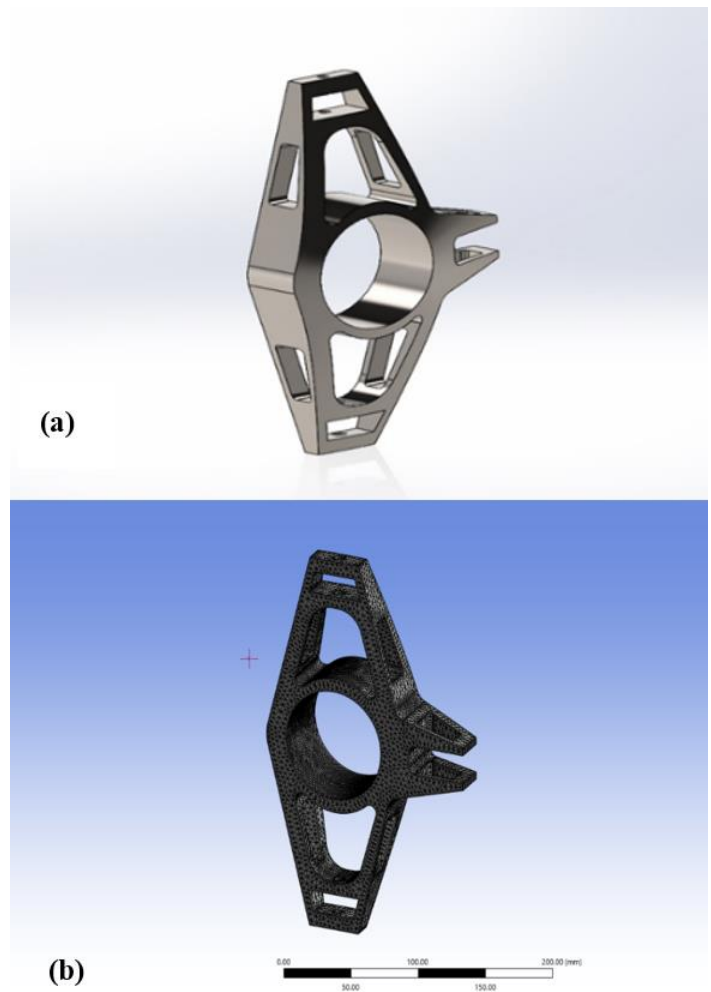Figure 2. Front View of Upright Geometry

Figure 3. (a) Isometric View Model Z; (b) Mesh grid section view of Model Z

Because its boundary conditions are established here to the body surface, Model Z makes use of a range of mesh types, including Figure (mesh independence test) 2mm, 3mm, 4mm, 5mm, 6mm, and 7mm. Most of it is coarse mesh. It is sufficient to use a finer mesh of 4 millimeters in areas of the structure that have simpler geometry and smaller stress gradients, such as those that are located far away from regions where the load is applied. The number of elements in this model is 67767, which is the average standard for this representation. The use of larger element sizes in these locations helps to reduce the cost of computation without affecting accuracy. This is because the stress distribution is typically more uniform in these areas.

2.4. Acting forces on upright

When constructing an upright, it is essential to take into consideration the forces that are applied to it. In Figure 4 the beginning, the forces that are applied to the uprights are measured in Newtons.

After that, the value is converted into values by dividing it by the mass of the vehicle. With the help of this conversion, it is possible to use these values in the design of an upright for another similar vehicle. The upright is subjected to a wide variety of forces, which may be broken down into the following categories.

Table 2 displays the results of the forces acting on the uprights while the student formula cars race around the track. This is the result of analyzing the Formula Student car circuit in a simulation. The accuracy of the numerical simulation determines the credibility of the results, and this validity is determined by the size and structure of the grid. Using unstructured tetrahedral cells, discretizing domains may be accomplished in Figure 5. A grid test must be carried out before conducting a comprehensive analysis to guarantee error-free findings that are impacted by mesh size. Within the context of this instance, the (Von-mises) stress is selected as the parameter to analyze the influence of the grid size. To evaluate the stress behavior of the upright throughout a range of different numbers of mesh elements, a graph is constructed by taking a total of seven different sets of mesh elements. The accuracy of the numerical simulation determines the credibility of the results, and this validity is determined by the size and structure of the grid. Using unstructured tetrahedral cells, discretizing domains may be accomplished. A grid test must be carried out before conducting a comprehensive analysis to guarantee error-free findings that are impacted by mesh size. Within the context of this instance, the (Von-mises) stress is selected as the parameter to analyze the influence of the grid size. To evaluate the stress behavior of the upright throughout a range of different numbers of mesh elements, a graph is constructed by taking a total of seven different sets of mesh elements.
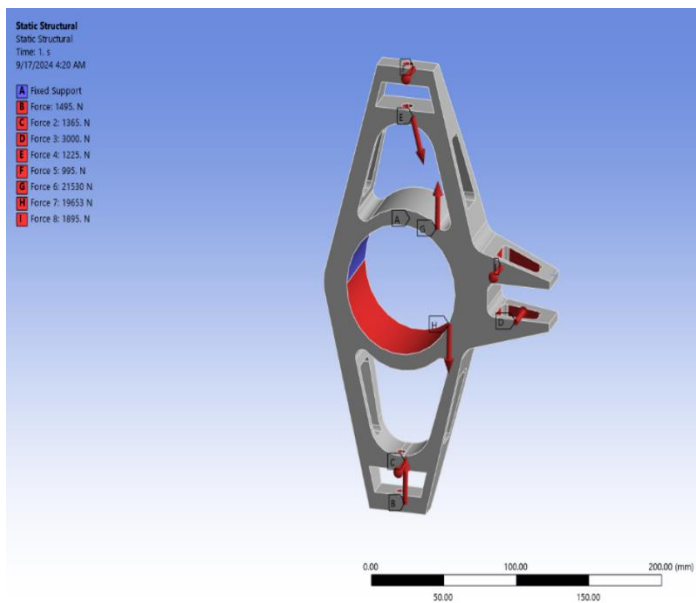

Figure 6. Acting forces on upright

A lack of convergence is shown by the graph even though it initially displays variances up to 50 thousand cells. On the other hand, the variation in the Von-mises stress value does not surpass 4% for mesh sizes that include 95,985 and 99,680 elements. Considering this, any value that falls within this range is allowed. Because the Topology technique acts on every node, the surface curve becomes smoother as there are more nodes. The complexity of this geometry may be more accurately represented by a mesh that is finer and has a higher element count, which will result in

more accurate calculations. Even though having an excessive number of tiny mesh pieces would be time-consuming. Therefore, for further investigation, a mesh consisting of 95,985 elements has been chosen. For computational investigation, a personal computer equipped with an AMD Ryzen 5 3500X CPU, 24 gigabytes of random-access memory (RAM), a Zotac GeForce GT1030 graphics processing unit (GPU), and a 6-core processor were used. Each example had an average runtime of close to one hour.

Table 2. forces on upright

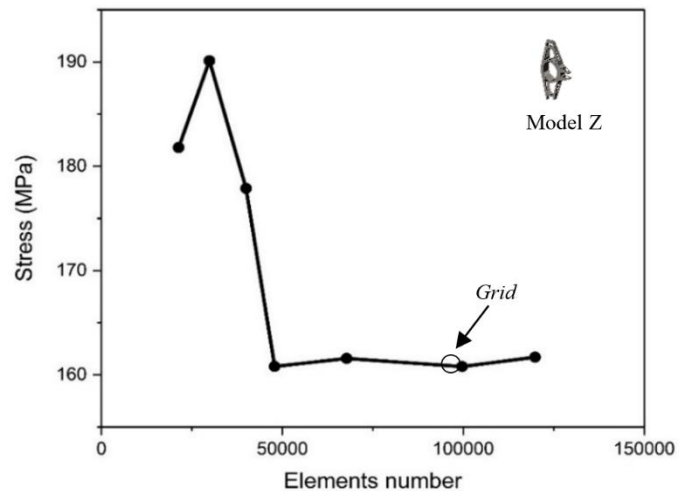| Force	Value (N)
Upper Wishbone Left	1225
Upper Wishbone Right	995
Tie Rod	1225
Lower Wishbone Left	1365
Lower Wishbone Right	1495
Pull/Push Rod	4500

Figure 5. Mesh independence test

2.5. Simulating model Z for FEA analysis

A mesh of tetrahedral elements was utilized to construct the finite element model, with suitable boundary conditions implemented to replicate the attachment points to the wheel hub and suspension members. The finite element analysis model was addressed through a linear static analysis to ascertain the stress distribution throughout the upright. The highest von Mises stress and displacement values were obtained, acting as performance metrics. The aim was to minimize the peak stress concentrations and the weight of the component via iterative optimization processes. It is necessary to do an initial Finite Element Analysis (FEA) of the model to get an understanding of the performance of the upright at a baseline before optimizing the design. This method is helpful for determining the distribution of stresses, deformation, and potential weak points in the original design when the load conditions that are predicted are taken into consideration. Using this research

able to assess whether the initial model exceeds the required criteria for safety, stiffness, and strength. The FE model and the selection of element types are subject to a number of factors, some of which are discussed below.

In consideration for the balance between computer complexity and accuracy. In order to meet the aim of striking a balance between the accuracy of the calculation and the efficiency of the computation, it is possible to accomplish this goal by selecting the appropriate element type and size, such as linear or higher-order. The use of smaller, finer pieces leads in enhanced accuracy, particularly in circumstances where there are significant stress gradients. On the other hand, the utilization of bigger components in regions with low stress results in a decrease in the cost of computing. The selection of the proper finite element model guarantees that the outcomes of the simulation are not dependent on the size of the mesh. This is because convergence and mesh independence enable the model to be independent of the mesh. When optimizing

the upright, it is essential to make use of a well-chosen finite element model in order to prevent over-refinement without sacrificing the dependability of the findings. This is because over-refinement might undermine the accuracy of the results. By using a three-dimensional finite element model (FE model), which ensures that these loads are thoroughly captured in all directions, it is able to create more accurate predictions of stresses and deformations. Table 3 depicts the data of model Z This is because the FE model records the loads in every direction. Using finite element analysis (FEA), it is able to develop more accurate predictions about how the upright will function in real operational circumstances. This is because FEA allows for more precise modelling of systems. Choosing appropriate parts not only helps to avoid unnecessarily intricate geometries that may be difficult or expensive to manufacture, but it also offers a better understanding of the constraints of manufacturability, such as the thickness of the material. This is because the selection of acceptable pieces helps to avoid unduly complicated geometries.

Table 3. 6061 T-6 Aluminum Martials upright nodes, element size, stress, strain and deformation model Z

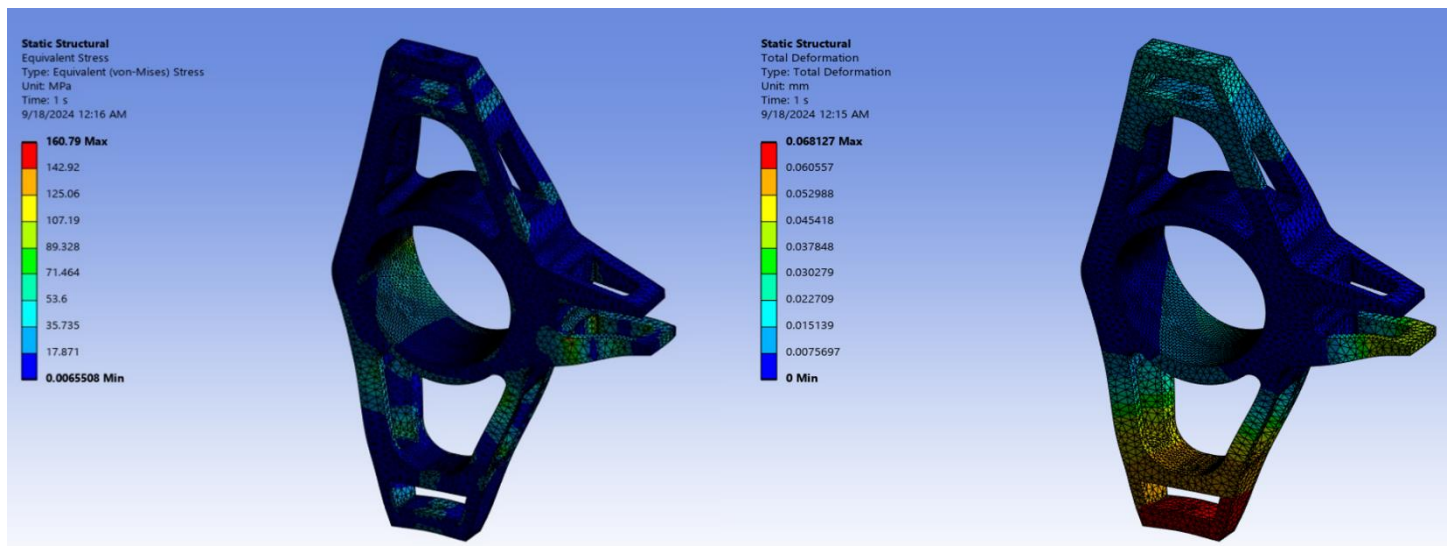| Mesh Sizing (mm)	2	3	4	5	6	7	8
Nodes	187956	159832	109428	79144	58822	41236	35893
Elements	119868	99680	95,985	67875	39969	29861	21325
Strain (mm)	0.00075	0.00075	0.00076	0.00079	0.00081	0.00089	0,00089
Deformation (mm)	0.0690	0.0688	0.0688	0.0697	0.0697	0.0567	0.0587
Stress (MPa)	160.58	159.81	160.79	139.04	145.01	129.45	126.89

Figure 7. Model Z Stress and Deformation

The use of mesh element sizes of 2, 3, 4, 5, 6 and 7 millimeters shown in Figure 6. Results in an increase in both the quality and accuracy of the model when it comes to the steering upright model Z. This improvement is a consequence of the usage of these mesh element sizes. When these mesh sizes are used, the orthogonal quality range for upright model is between 0.20 and 0.65, which is considered to be a level that is acceptable. Skewness is considered to be of acceptable quality for model Z if it falls between 0.55

and 75. This is the other end of the spectrum from the previously mentioned quality. Power-to-weight ratio very high One of the most well-known alloys is 6061-T6, which is distinguished by its remarkable equilibrium between the weight and the strength of the material. Weight reduction is of the utmost importance in racing situations such as Formula SAE, and 6061-T6 offers appropriate strength while yet maintaining a lightweight component when used in these environments. Furthermore, the strength that

is necessary for preliminary testing is enough. However, despite the fact that it is probable that 6061-T6 does not contain the increased strength of titanium alloys such as Ti-6Al-4V, it is strong enough
to endure the early stress and load simulations that are carried out in finite element analysis (FEA). The end result of this is that it is now feasible for designers to evaluate the entire performance of the device before moving on with further optimization. The simplicity with which 6061-T6 can be machined makes it a good material for use in the production of prototypes. This allows for the prototypes to be manufactured in a short amount of time and at a cheap cost. This is the strategy that need to be used in the event that a design is still in its earliest stages and may require a significant number of modifications. The capacity to weld and the capacities of fabrication During the process of developing the prototype, it is feasible to weld it in a short amount of time, which gives flexibility for making alterations to the design or connecting it with other components. Since 6061-T6 has specific limitations when it is subjected to extreme loads or stress concentrations, it is

probable that the final design may need a switch to more durable materials, such as titanium alloys. This is because they are more resistant to the effects of stress. On the other hand, when it comes to the initial material for the 3D model, it is an ideal choice since it strikes a good mix between performance.

Figure 7 elucidate the strain values and safety factor of model Z, where a load is applied to the upright in the simulation. The contour of model Z element, nodes stress, deformation, strain, and the factor of safety are all described. The safety factor is 1.5549, the strain is around 0.00089, the greatest stress it can take is 160.79, and the final factor is deformation, which is ap-proximately 0.0681. The material used for the upright is 6061 T6 aluminum, and this is the original model Z data available in Figure 8. The purpose of this is to reflect all the data and emphasize that this model will be subjected to the FEM technique and topology solver to achieve accuracy and change the design. The contour colors represent the values corresponding to the upright's behavior regarding maximum and lowest strain, as well as the safety factor of model Z.
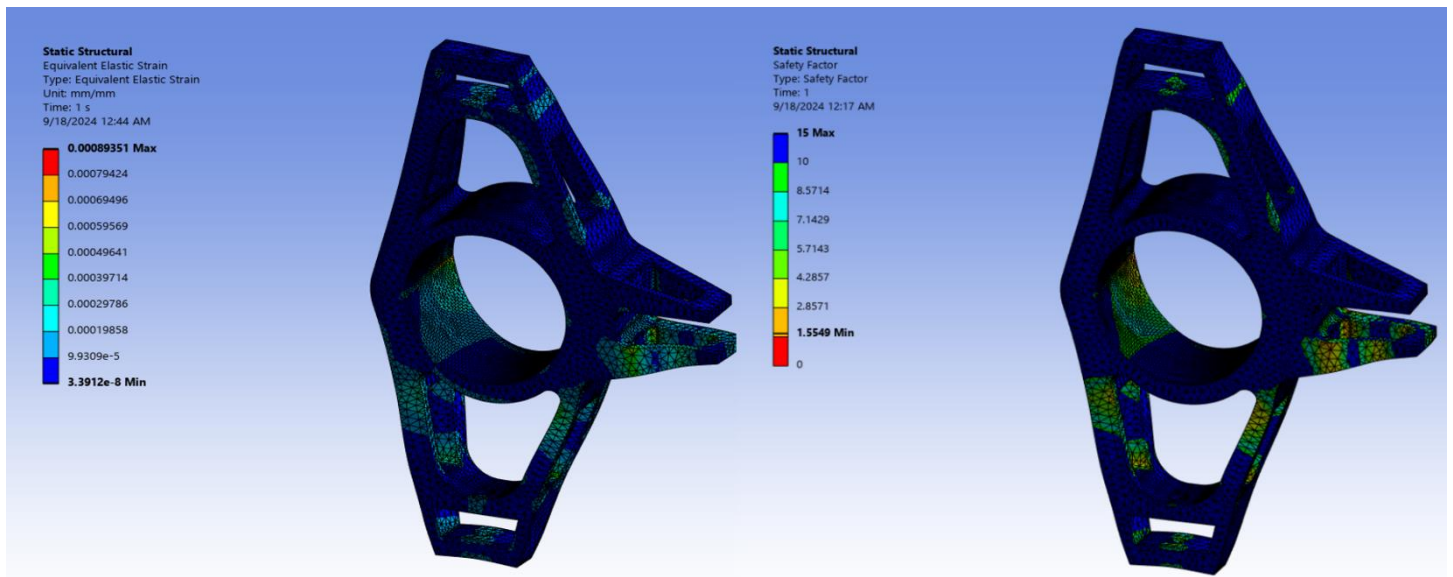

Figure 8. Model Z Strain and safety factor

2.6. Validation

A finite element analysis of a structural rigid body was performed to validate the accuracy of the method used for analyzing the steering upright. The boundary condition and model parameters derived from the literature, Figure 10. particularly concerning the FEA analysis of force application on structural uprights, were utilized for the analysis, Table 4 as presented by Ammarul Hasan et al[24].

Although this is the case, the model may have gaps due to assumptions and simplifications. Using finite element analysis (FEA), one may approximate the behavior of materials and structures when they are subjected to stress in the actual world. If validation is not carried out, it is possible that the predicted stress distribution deformations, and failure modes will not accurately

portray the actual performance. Considering that there is no validation, the possibility of harm is there[24].Despite this Figure 9, assumptions and simplifications in the model might lead to gaps.

Finite element analysis (FEA) approximates the behavior of materials and structures under stress in the real world. The projected stress distribution, deformations, and failure modes may not correctly represent in Figure 11. actual performance if validation is not performed. This risk exists because of the absence of validation.

Table 4. Validation Deviation present work and previous author work

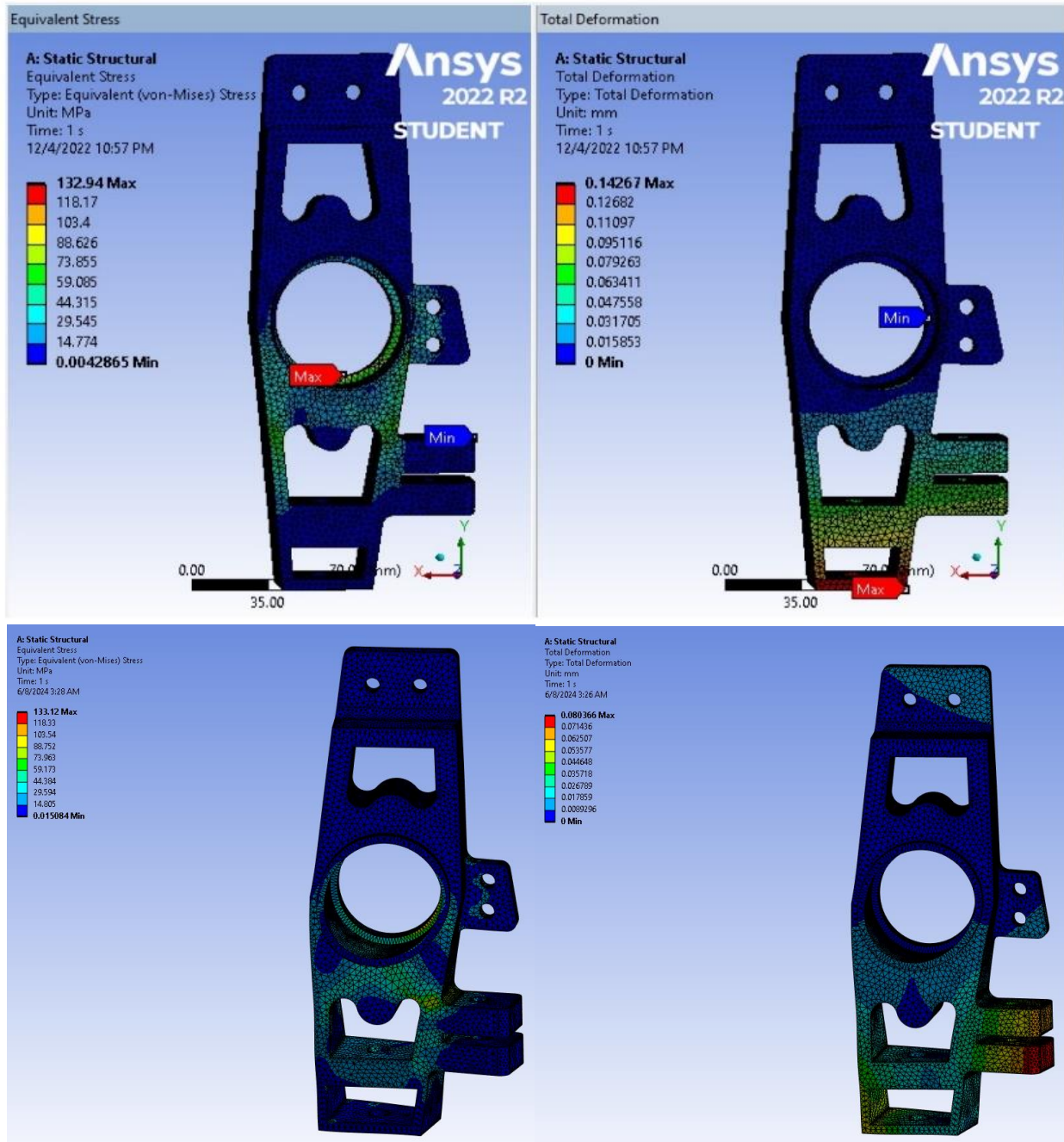| Contour	Ammarul Hasan	Present Work
Deformation (mm)	0.142	0.080
Equivalent Stress (MPa)	132.94	133.12 MPa

Figure 8. (a) Previous work and (b) Present work

2.7. Topology optimization

Topology optimization was utilized to minimize the mass of the steering upright while ensuring structural integrity was kept. This Figure 12. approach enhances the allocation of materials throughout the design area by eliminating material from regions that undergo reduced stresses, thereby decreasing weight while maintaining the ability to support loads[25][26][27]. The Topology optimization problem was formulated as Eq. (8).

$$min \ C(\rho, u) = min \int_\Omega \sigma \ C(\rho, u): \epsilon(u) \, d\Omega \qquad (8)$$

Where, C (ρ, u) is the compliance, representing the stiffness of the structure, k (ρ) is the global stiffness matrix, a function of the density distribution ρ and F represents the applied forces

3. Result and Discussion

Design Optimization:

After the topology optimization, a structural optimization was conducted to enhance the design and confirm that the component could withstand actual loads encountered in practical applications. The aim was to enhance rigidity while reducing mass through precise adjustments Eq.(9), (10) to the thickness of the load-bearing components and fillets, thereby ensuring that stress concentrations were kept to a minimum.
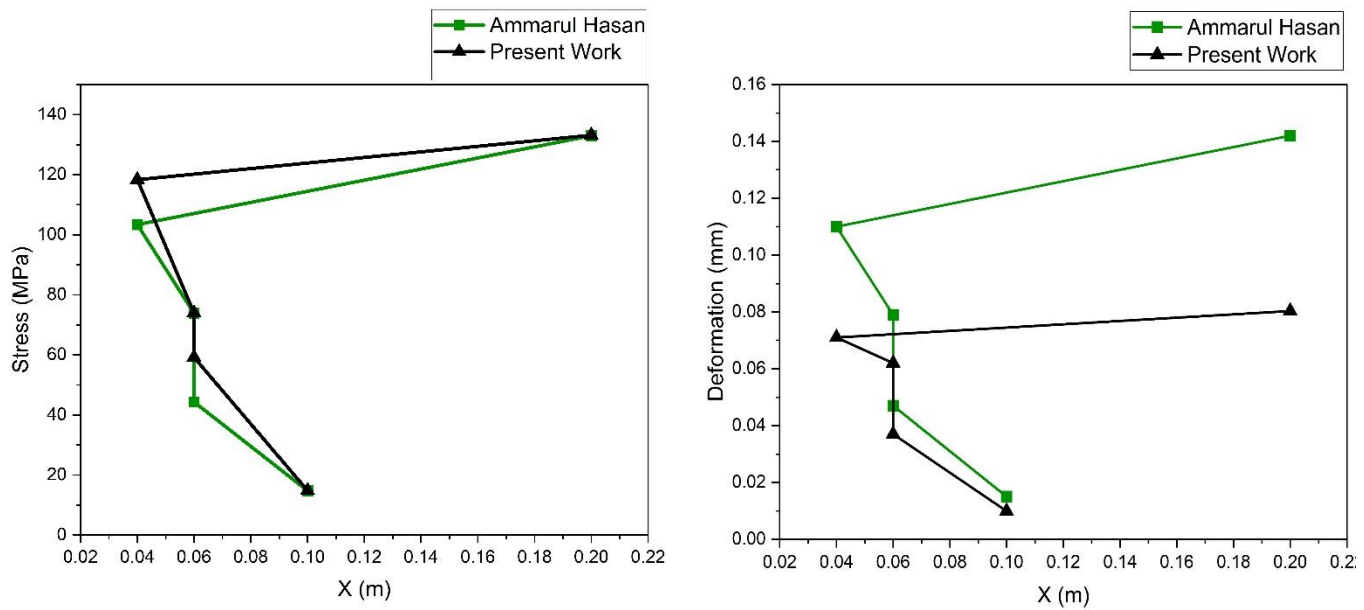
Figure 9. Stress plot; Deformation Plot of Present work and previous author Ammarul Hasan work

(a)

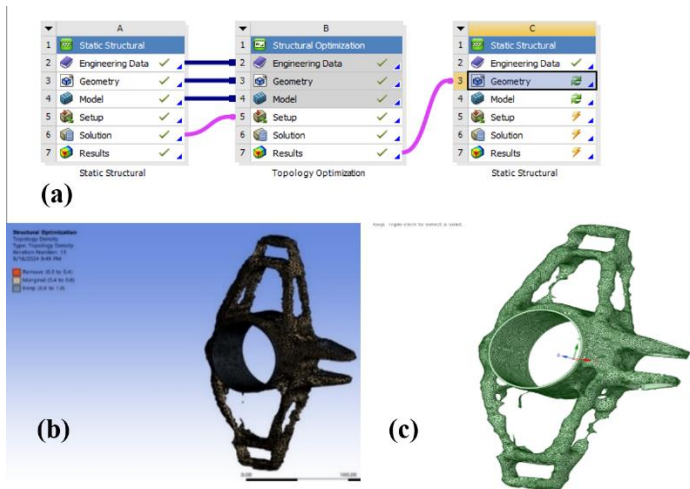**(b)**   **(c)**

Figure 10. (a) topology optimization (b)Process in Work-bench; (c)Topology optimization structural

The Structural optimization problem was formulated as;

$$minf(x) = Weight(X): g_i(X) \leq o \forall i \in \{1, \dots N\} \qquad (9)$$

$$\sigma_{max} \leq \sigma_{allowable} \qquad (10)$$

The bending stress is determined using Eq.(11) of pure bending moment, while the direct stress is determined using Eq. (12)

$$\frac{\sigma}{y} = \frac{M}{I} \qquad (11)$$

$$\frac{P}{A} = \sigma \qquad (12)$$

Following completing the topology optimization processes on the upright model, Figure 13 kept 70% of the upright body while simultaneously reducing 30%t of the upright's mass. After that, redesigned it and transferred it to the geometry section of Ansys.

Also recovered the edges and the reduction part by using cut extrude from the materials. Modified the design with new parameters that were fully defined and certified by the topology optimization method. Finally, made sure that the new material Ti6Al – 4V (aged and treated) had high strength and could withstand more stress and deformation than 6061 T-6 aluminum. Additionally, Table 6, this material has a high degree of legibility. It can carry any bearing load, bolt hole load, brake caliper load, and wishbone load and force constantly perceptively, as well as endure stress, strain and deformation, and it also reduces the bulk of the upright in comparison to the original model Z upright, which is constructed of 6061 T6 aluminum.
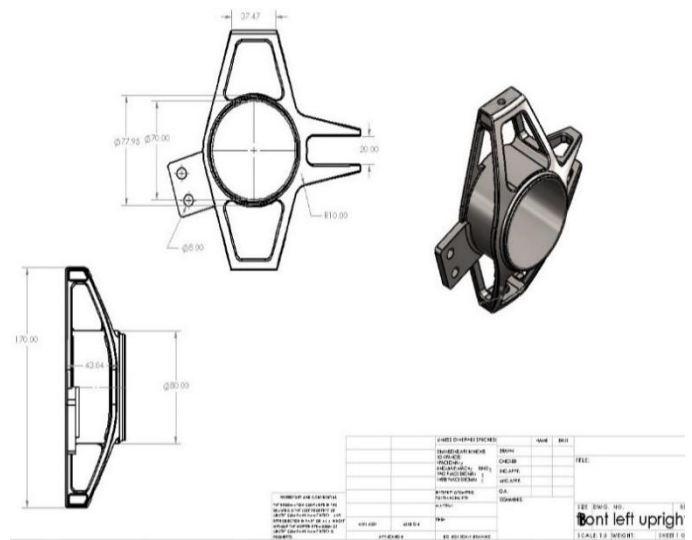

Figure 10. Modify optimized design

The maximum stress it can withstand is 342.32MPa Figure 18. with a deformation of 0.1128 mm, and the factor of safety is 2.6237, which is considered an acceptable standard within the range of 1.5 to 4 Table 7. The application of the Topology solver

in Ansys Structural facilitated an enhanced Upright configuration Figure 14. The optimization led to a notable reduction in mass, with the refined upright demonstrating a decrease of approximately 41.58% when compared to model Z, which weighed 1.232 kg, and the optimized model, which weighed 0.604 kg Figure 14. The structural design technique underwent evaluation, Figure 16. followed by the development of a rigorous mathematical model aimed at enhancing the topology of the steering knuckle for optimal performance. Selecting various element sizes such as 2, 3, 4, 5, 6, and 7 mm for meshing in the finite element analysis (FEA) of a steering upright fulfils numerous significant objectives. Each size is chosen to optimize accuracy, computing efficiency, and to guarantee the convergence.
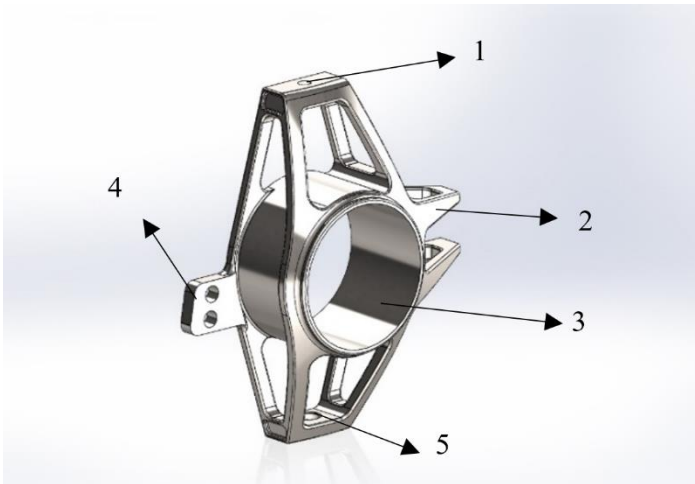

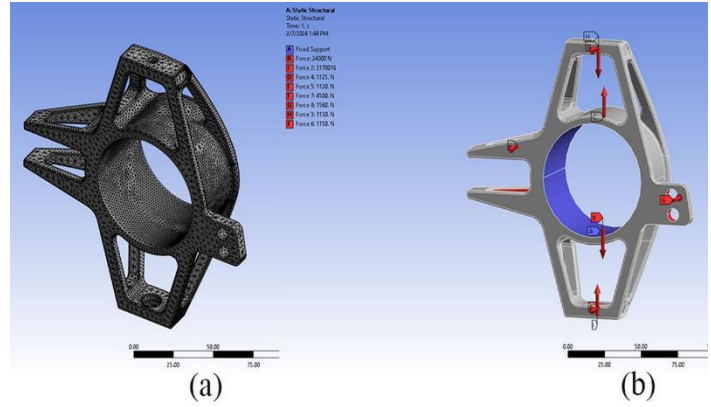Figure 11. Optimized Structural Design

Figure 12. Mesh Domain Optimized model; (b) Action force on Optimized Model

Table 5. Contact surface

Constrains point	Locations
1	Upper wishbone rod mount
2	Tie rod mount
3	Half shaft and bearing
4	Brake caliper mount
5	lower wishbone rod mount

Table 6. Ti-6Al-4V Material properties of Optimized model

Property	Ti-6Al-4V (aged and treated)
Density (g/cm³)	4.43
Tensile Strength (MPa)	1100
Yield Strength (MPa)	973
Young's Modulus (GPa)	113
Poisson's Ratio	0.34

Table 6. Titanium Alloy Ti-6AL-4V Martials optimized upright nodes, element size, stress, strain and deformation data

Mesh sizing (mm)	2	3	4	5	6	7	8
Nodes	156262	13524	106292	95044	89850	82331	71123
Elements	107897	95481	71753	64552	51287	47086	41235
Strain (mm)	0.00159	0.00166	0.00167	0.00171	0.00171	0.00172	0.00178
Deformation (mm)	0.11994	0.12837	0.12841	0.11284	0.11280	0.10984	0.10284

Refinement in critical areas (2-3 mm): Smaller elements (2-3 mm) are often used in areas of the structure where significant stress concentrations or intricate geometries are anticipated, such as next to bolt holes, fillets, and other acute transitions.

Moderate Refinement in Medium-Stress sections (4-5 mm): Moderately stressed vertical sections with simple geometry are refined using a medium-sized mesh (4-5 mm). These components balance precision and computational efficiency.

Coarser Mesh in Low-Stress Areas (6-7 mm): In low-stress, simple-geometry zones, coarser mesh (6-7 mm) is employed. Using a coarse mesh in these places decreases the number of elements and speeds up processing without affecting accuracy. Time and computing resources are saved using this method.

Mesh Convergence study: Using a range of element sizes (2 to 7 mm) facilitates the execution of a mesh convergence investigation. This requires performing simulations with varying mesh sizes to examine the changes in outcomes (e.g., stress, strain, deformation)

due to mesh refinement. When further refinement (e.g., from 3 mm to 2 mm) yields few changes in the solution, the mesh is deemed "converged," indicating that the solution is independent of the mesh size. This guarantees the reliability of the findings. Figure 15. It is often believed that titanium alloy (Ti-6Al-4V) is one of the best materials to use when making a Formula SAE (FSAE) steering upright, especially in the latter stages of design when performance is key. Among the several options, Ti-6Al-4V is superior for the reasons listed below Figure 17. The "Optimized Model" of the steering upright Figure 16. uses mesh element sizes of 2, 3, 4, 5, 6, and 7 millimeters', which improves the model's quality and accuracy. The usage of these mesh element sizes allowed for the completion of this upgrade. If use these mesh sizes, our upright model's orthogonal quality ranges from 0.22 to 0.65, which is well within the acceptable range. A skewness value between 0.25 and 45 indicates that the "Optimized Model" is of good quality. This condition is really satisfying, and the model Z isn't

even close. Superb power-to-weight capacity with a higher strength-to-weight ratio, Ti-6Al-4V outperforms 6061-T6 Table 5. Higher loads and strains may be absorbed by the upright without increasing its weight, leading to improved vehicle dynamics and less unsprang bulk. Given the high loads applied to an FSAE car's upright during acceleration, braking, and turns, Ti-6Al-4V is a superior material over 6061-T6 aluminum. The high tensile strength of the material, which increases to 900 MPa Table 6. after treatment and ageing, allows the upright to resist deformation under severe loads. Because Ti-6Al-4V is stronger, engineers may use it to produce lighter uprights that are more optimized without compromising safety or performance by reducing material in low-

stress areas. Important for weight-minimizing topology-optimized designs. Suitability for high-performance and safety-critical components like Formula SAE steering uprights is attributed to Ti-6Al-4V's strength, stiffness, fatigue resistance, and lightweight properties. Despite being more expensive and complicated to build, it is the best option for the last FSAE upright since its racing advantages outweigh the drawbacks.

Formula SAE cars secure the wheel with the hub and bearing assembly in the upright assembly. Finally, Figure 19.all components must be torqued precisely for safety, alignment, and vehicle handling.
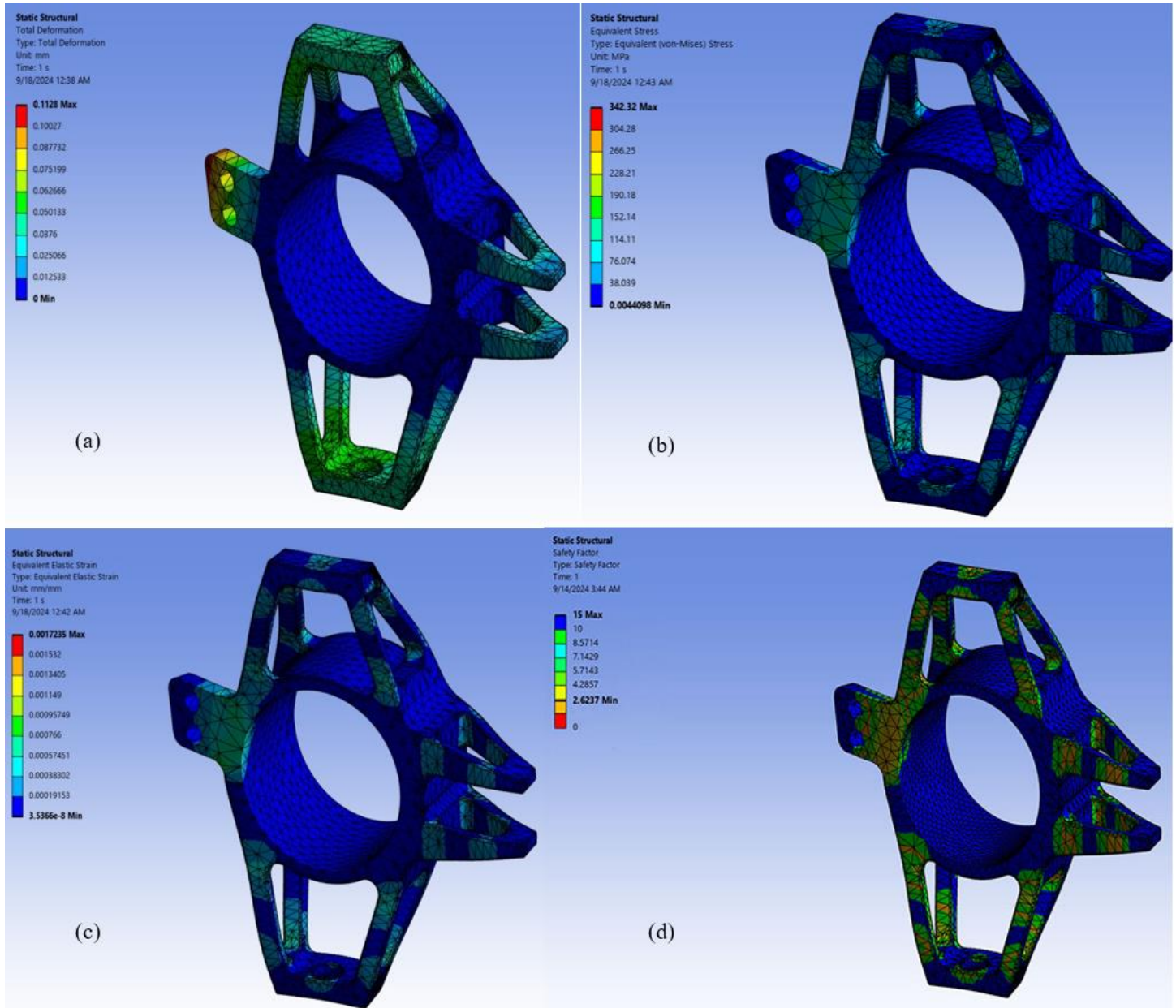

Figure 13.Optimized model (a) Deformation; (b) Stress (c) Strain and (d) Safety of factor
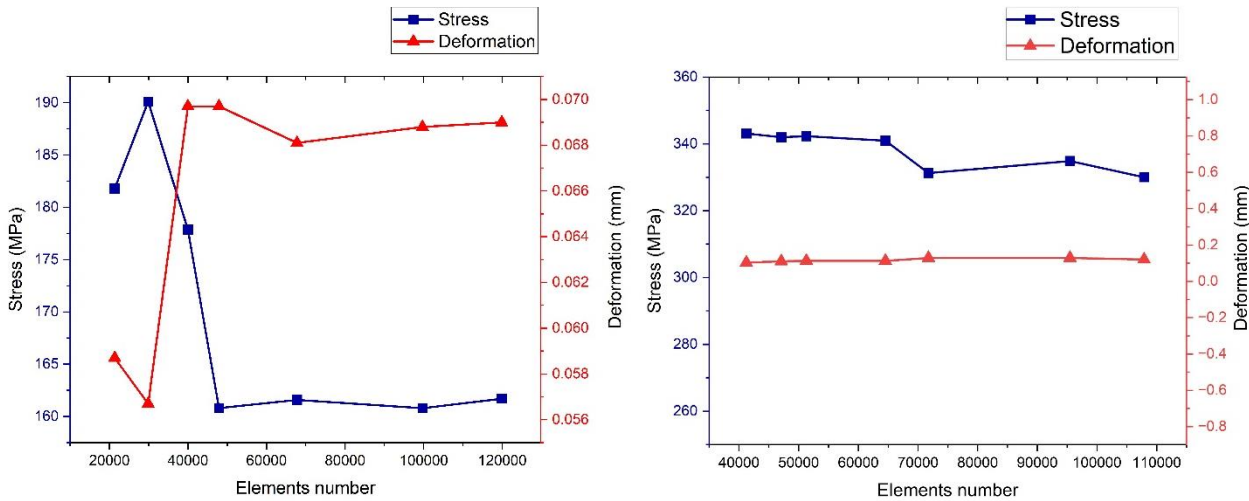
167

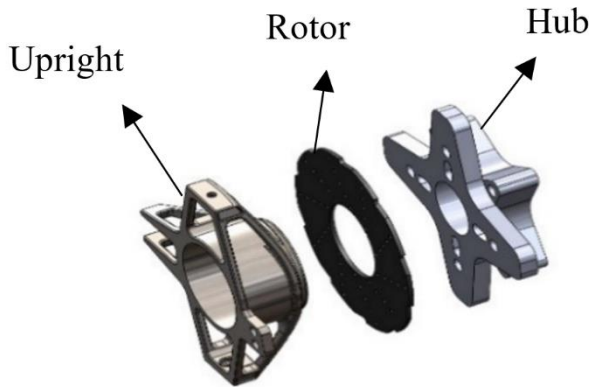Figure 14. Model Z and Optimized Model Stress and deformation vs elements number

Figure 16. Assembly of Upright

4.Conclusion

This investigation focused on improving weight reduction and enhancing performance in a Formula Student car by optimizing the upright design. Steering upright made of Titanium-6AL-4V solution treated and aged (SS) was found to be the best option because of its more compact geometrical properties. This accomplishment was realized by integrating the topology approach with foundational structural principles. The FEM methodology was validated using an upright design by Ammarul Hasan, achieving a deviation of merely 0.0438% for deformation and 0.1272% for stress. The main conclusions of this research are outlined as follows

- Utilizing the Topology solver in Ansys Structural enabled an optimized Upright configuration. This optimization resulted in a significant decrease in mass, with the optimized upright showing a reduction of nearly 41.58% compared to model Z at 1.232 kg and the Optimized model at 0. 604 kg.
- The structural Design technique was evaluated, and then a rigorous mathematical model was developed to improve the topology of the steering knuckle for optimal performance. To conform to the requirements for the suspension at the IMechE FSUK Competition in

2023, the geometry of the upright was precisely optimized.

- In the first model, the stress reached a maximum of 160.79 MPa, while Model 2 exhibited a stress of 342.32 MPa. A comparison of these models reveals significant differences in stress levels. 47% of stress will be enhanced in model 2.
- Performance analysis indicated that the optimized upright has a lower mass compared to the model Z upright. This analysis revealed that the optimized Model upright will result in an approximate 2.56 kg reduction in the car's overall weight.
- The safety factor of Model Z and the optimized model is compared, with the standard value ranging from 1.5 to 4. The optimized model's value is 2.6237, which meets the standard.

The development of this project sets the foundation for numerous practical recommendations that can inform upcoming efforts in this field. The following suggestions include

- Comprehensive analysis of complete full-car wheel balance and skid pad track layout.
- Physical testing and manufacturing can be perfectly integrated into CNC machining or forging processes in the near term.

This continuous improvement process highlights a dedication to quality and creativity, where each design iteration acts as a building block to reach peak performance and remain competitive. The expected recommendations are essential for progressing the area of Formula Student, improving vehicle performance, and will assist in ending the divide between computational simulations and practical, real-world performance, thereby increasing the importance and reliability of the research findings.

Acknowledgment

Abbreviation

FSAE	Formula Society of Automotive Engineeres
IMechE	Institutions of Mechanical Engineers
FOS	Factor of Safety
FEA	Finite Element Analysis
LW	Light Weight
BSPD	Brake System Plausibility Device
DOF	Degree of freedom
DSS	Design Spec Sheet
SAE	Society of Automotive Engineers
TO	Topology optimization
SW	SolidWorks

Conflict of Interest Statement

The authors declare that there are no conflicts of interest in the study.

CRediT Author Statement

Sk Al Nahian Samin played a key role in developing the design and conducting FEA analysis for the topology optimization methodology, writing the original draft, Visualization, Validation, Software, Methodology, Investigation, Formal analysis, Data curation and Conceptualization. Additionally, **Sazzad Hossen** contributed to writing the original draft, Visualization, Formal analysis and Data curation. **K M Mahfuzur Rahman** writing and editing the manuscript. **Utsab Ghosh** review & editing and Visualization. **Sk Al Nahian Samin** played a crucial role in overseeing the development of this research and offered valuable feedback on the work. All authors have read and approved the final manuscript by ethical standards.

Funding Statement

References

1. Kopec, M., Liu, X., Gorniewicz, D., Modrzejewski, P., Zasada, D., Jóźwiak, S., Janiszewski, J., & Kowalewski, Z. L. (2024). Mechanical response of 6061-T6 aluminium alloy subjected to dynamic testing at low temperature: Experiment and modelling. International Journal of Impact Engineering, 185, 104843.
2. Kumar, Y., Siddiqui, R. A., Upadhyay, Y., & Prajapati, S. (2022). Kinematic and Structural Analysis of Independent type suspension system with Anti-Roll bar for Formula Student Vehicle. Materials Today: Proceedings, 56, 2672–2679.
3. Cherenda, N. N., Basalai, A. V., Shymanski, V. I., Uglov, V. V., Surface and Coatings Technology, 355, 148–154.
4. Astashynski, V. M., Kuzmitski, A. M., Laskovnev, A. P., & Remnev, G. E. (2018). Modification of Ti-6Al-4V alloy element and phase composition by compression plasma flows impact.
5. Milliken, W. F., Milliken, D. L., & Metz, L. D. (1995). Race car vehicle dynamics . Warrendale: SAE international.
6. Raj, P., Battula, K., & Pradeep Kumar, V. (2021). modelling and analysis of an automobile steering knuckle component. International Research Journal of Modernization in Engineering Technology and Science, 03(12); 1416.-1435
7. Rajput, H. S., Agrawal, Y., & Tiwari, N. (2019). Design and Analysis of Steering Knuckle for Electric ATV. International Research Journal of Engineering and Technology, 6(12), 528-531.
8. Babu, T. N., Nair, R. S., Bhadade, R., Garg, R., Rathod, A., Chandel, A. S., & Prabha, D. R. (2022). Simulation and analysis of an fsae wheel upright using finite element methods. Journal of Pharmaceutical Negative Results, 1241-1257.
9. Bendsøe, M. P., & Kikuchi, N. (1988). Generating optimal topologies in structural design using a homogenization method. Computer Methods in Applied Mechanics and Engineering, 71(2), 197–224.
10. Tsai, C. J., & Wang, L. M. (2014). Improved mechanical properties of Ti–6Al–4V alloy by electron beam welding process plus annealing treatments and its microstructural evolution. Materials & Design, 60, 587–598.
11. Garde, K., Shinde, P., & Jirage, R. (2014). Design and optimization of hub and knuckle for Formula SAE car. International Journal of Engineering Research and Development, 10(10); 65-69.
12. Aage, N., Nobel-Jørgensen, M., Andreasen, C. S., & Sigmund, O. (2013). Interactive topology optimization on hand-held devices. Structural and Multidisciplinary Optimization, 47(1), 1–6.
13. Sigmund, O., & Maute, K. (2013). Topology optimization approaches: A comparative review. Structural and multidisciplinary optimization, 48(6), 1031-1055.
14. Nikhil, R., & S, D. N. (2018). Tensile Stress Analysis of Steering Knuckle of an Automobile under Static Load. International Journal of Applied Engineering Research, 13(11); 9241-9244.
15. Mutha, A., Thosar, S., & Ghodmare, N. (2016). Design and optimization of a steering knuckle of FSAE car. In Innovative Design and Development Practices in Aerospace and Automotive Engineering: I-DAD, February 22-24, 2016 (pp. 463-472). Singapore: Springer Nature Singapore.
16. Jin, Z., Li, J., & Chen, Z. (Eds.). (2020). Computational modelling of biomechanics and biotribology in the musculoskeletal system: biomaterials and tissues. Woodhead Publishing.
17. Swain, I., & Khan, S. N. (2021). Design Improvement of Steering Upright by Investigating Static and Dynamic Analysis. International Journal of Engineering Sciences, 13(4).
18. Gupta, H., Shan, Rajvardhan, & Singh, N. K. (2021). Design and analysis of steering knuckle of hybrid metal matrix composite for the fsae vehicle. Materials Today: Proceedings, 46, 10551–10557.
19. Bi, M., Tran, P., Xia, L., Ma, G., & Xie, Y. M. (2022). Topology optimization for 3D concrete printing with various manufacturing constraints. Additive Manufacturing, 57, 102982.
20. García-Manrique, J. A., Peña-Miñano, S., & Rivas, M. (2015). Manufacturing to Motorsport by Students. Procedia Engineering, 132, 259–266.
21. Jiang, X., Zhang, W., Liu, C., Du, Z., & Guo, X. (2023). An explicit approach for simultaneous shape and topology optimization of shell structures. Applied Mathematical Modelling, 113, 613–639.
22. Moudi, M., & Othman, M. (2017). Mathematical modelling for TM topology under uniform and hotspot traffic patterns. Automatika, 58(1), 88–96.

23. Hunar, M., Jancar, L., Krzikalla, D., Kaprinay, D., & Srnicek, D. (2020). Comprehensive view on racing car upright design and manufacturing. Symmetry, 12(6); 1020.

24. Zach, T.-F., & Dudescu, M.-C. (2021). The Topological Optimization and the Design for Additive Manufacturing of a Steering Knuckle for Formula SAE Electric Vehicle. MATEC Web of Conferences, 343, 04011.

25. Hasan, A., Lu, C., & Liu, W. (2023). Lightweight Design and Analysis of Steering Knuckle of Formula Student Car Using Topology Optimization Method. World Electric Vehicle Journal, 14(9), 233.

26. Wang, M. Y., Wang, X., & Guo, D. (2003). A level set method for structural topology optimization. Computer Methods in Applied Mechanics and Engineering, 192(1–2), 227–246.

27. Mesicek, J., Richtar, M., Petru, J., Pagac, M., & Kutiova, K. (2018). Complex view to racing car upright design and manufacturing. Manuf. Technol, 18, 449-456.

28. Kang, P., & Youn, S. K. (2016). Isogeometric topology optimization of shell structures using trimmed NURBS surfaces. Finite Elements in Analysis and Design, 120, 18–40.

ENGINEERING PERSPECTIVE

Research Paper
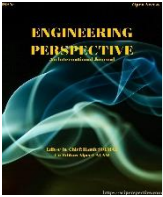
Classification of Zinc Recovery Quality from EAF Dust Using Machine Learning: A Waelz Process Study

Didem Özcan [iD], Kürşat Mustafa Karaoğlan [iD], Mehmet Çelik[*] [iD]

[1]*Mechanical Engineering Department, Faculty of Engineering, Karabük University, Karabük, 78050, Turkey*
[2]*Computer Engineering Department, Faculty of Engineering, Karabük University, Karabük, 78050, Turkey*
[3]*Mechanical Engineering Department, Faculty of Engineering, Karabük University, Karabük, 78050, Turkey*

ABSTRACT

Zinc recovery from Electric Arc Furnace (EAF) dust represents a significant challenge in the iron and steel industry. This study aims to classify zinc quality in slag produced through the Waelz process, where zinc is reduced and volatilized at high temperatures (>1000°C) in rotary kilns, using machine learning techniques. The classification of zinc quality in slag is crucial for process optimization and environmental sustainability, as it directly impacts both resource recovery efficiency and waste management strategies. The dataset utilized for developing classification models was obtained from chemical analyses of Waelz process raw materials and slag samples. Four distinct classification algorithms (Support Vector Machine SVM, Decision Tree - DT, Naive Bayes - NB, and Random Forest - RF) were evaluated on the data labeled by experts according to zinc content in slag. The reliability of the models was assessed through 10-fold cross-validation. In experimental studies, the DT algorithm demonstrated superior performance with 100.0% accuracy, precision, sensitivity, and F1 score. The RF algorithm achieved second-place performance with 96.0-98.0% accuracy and 100.0% precision, followed byNB with 91.0-94.0% accuracy, and SVM with 84.0-88.0% accuracy. The results indicate that the DT algorithm can serve as a reliable tool for quality classification in the zinc recovery process. These findings contribute significantly to the advancement of automated quality control systems in metallurgical processes, potentially enabling real-time monitoring and optimization of zinc recovery operations.

Keywords: Zinc Recovery, Electric Arc Furnace Dust, Waelz Process, Machine Learning Classification, Slag Quality.

1. Introduction

The extraction of metals worldwide produces a range of goods and services that underpin modern society. This practice has been critical to human survival since the Bronze Age. Later in the 20th century, metals evolved from basic building materials to a versatile resource that influenced many aspects of modern industry and technology [1]. Zinc is a silvery bluish-gray metal with a low melting and boiling point of 420°C and 907°C, respectively. Although zinc is brittle at average temperature, it can be formed at 100°C and rolled quickly. Typically found in brittle form, it transforms into a malleable metal when heated. Globally, zinc is the third most widely used non-ferrous metal after iron, aluminum, and copper, and the most used metal [2]. Zinc can be combined with aluminum to produce the alloy used in die casting. Die cast-

ing forces molten metal into a mold cavity by applying high pressure [3]. Zinc demand in global markets includes use in galvanizing steel and iron (50%), alloys (17%), brass and bronze (17%), semi-manufacturing (6%), chemicals (6%) and other applications in various sectors (4%) [2].

2016-2017, overall zinc consumption worldwide increased by approximately 2%. However, there are significant variations from region to region. 2020 global refined zinc production increased to 13.8 million tons. Zinc production is predominantly based on primary resource mining [3-5]. In order to reduce CO_2 emissions by 80% from current levels by 2050 (i.e., to reduce emissions below 2.13 million tons of CO_2 equivalent), the increased demand must be met by recovering zinc from waste, i.e., from secondary sources. Recovering zinc from secondary sources is essential in the current circular economy. Zinc production and consumption

are increasing globally, and primary sources of zinc from ore are rapidly depleted. Therefore, effectively extracting zinc from secondary sources can bring several advantages. These advantages include savings in raw resources and fossil resources used to power primary mining processes, increased resource efficiency, reduced resource loss to landfills and dumps, avoided loss of zinc or any metal to landfill, waste treatment, mitigation of environmental and health impacts, and improved economic performance of existing infrastructure. Secondary sources of zinc from waste include zinc in spent batteries, in e-waste, in wastewater, in construction and demolition waste, in scrap steelmaking dust, and in municipal waste [3].

The electric arc furnace (EAF) method is used to recycle scrap. However, recycling these wastes and iron by-products using EAF is associated with the emission of dust particles, which, according to the United States Environmental Agency, are considered hazardous solid waste. Due to its chemical and physical properties, EAF dust is classified as hazardous waste according to the European Waste Catalogue, where hazardous substances are present above a threshold concentration. EAF dust is produced from the evaporation of heavy metals and silica particles during the melting of steel scrap. During the melting of scrap, volatile components are removed by smoke and collected together with particulate matter in the waste gas cleaning system. During the metal melting process, the EAF can reach temperatures of 1600°C or higher, and many components of the charge, including iron, zinc, and lead, vaporize and enter the gas phase. When the vapor is cooled and collected, a large amount of dust is generated [6-7]. This dust is produced at a rate of 10-20 kg per ton of steel, which could mean that as much as 5-7 million tons of high dust is produced worldwide each year. However, this dust contains a fair amount of heavy metals such as zinc, which contains 20-30 wt% zinc oxide. Given the low production cost, recovering zinc at such a high percentage is an attractive option. Two main technological processes extract zinc from EAF dust: pyrometallurgical and hydrometallurgical methods. The pyrometallurgical method is costly due to the enormous energy consumption and the need for reductants to produce zinc oxides with low commercial value. The hydrometallurgical method is more advantageous than the pyrometallurgical method in terms of process economics and environment [6]. The chemical composition of EAF powder depends mainly on the quality of the steel scrap processed and the type of steel produced. Table 1 shows the chemical composition of EAF powder.

This study aims to make a scientific contribution to the improvement of zinc recovery processes in rotary kilns by using classification methods of the Waelz process. In the study, zinc recovery was performed with the Waelz process, and Support Vector Machines (SVM), Decision Tree (DT), Random Forest (RF), and Naive Bayes (NB) machine learning models were evaluated to classify the zinc quality in the slag and make accurate quality determination using supervised machine learning techniques.

2. Materials and methods

The Waelz process, implemented for zinc recovery from EAF dust in rotary kilns, was utilized to obtain the labeled data for this study. This process is widely employed worldwide, including multiple facilities in Turkey, specifically in the provinces of Izmir,

Kayseri, Karabük, and Hatay. The primary equipment in the Waelz process is a rotary kiln with dimensions of 65 meters in length and 4.4 meters in diameter. The kiln operates at a 2% inclination with a rotation speed of 1.1 rpm. Due to operational temperatures exceeding 1200°C, the kiln requires protection against potential structural damage. High-alumina refractory bricks line the inner wall of the rotary kiln for this purpose. The chemical composition of these refractory bricks varies by zone, corresponding to the temperature gradient along the kiln length. In the slag exit zone, where temperatures can reach 1200°C, the refractory bricks contain approximately 70% alumina, while other zones utilize varying brick compositions based on their specific thermal requirements. Figure 1 illustrates the temperature distribution along the kiln's outer shell, with regions 8, 9, and 10 representing the slag zone. The classification data were obtained through chemical analyses of Waelz process raw materials and slag samples, with expert labeling for quality assessment. Four machine learning algorithms - Support Vector Machine (SVM), Decision Tree (DT), Random Forest (RF), and Naive Bayes (NB) - were employed for slag zinc quality classification. Model reliability was ensured through cross-validation techniques and hyperparameter optimization. The experimental results demonstrated that the DT model achieved superior classification performance exceeding 99% accuracy, with other models showing comparable performance levels. [8].

Table 1. Chemical composition of EAF powder [7]

Oxides	Weight (%)
SiO_2	1.145
Al_2O_3	0.519
Fe_2O_3	24.780
CaO	18.600
MgO	3.949
K_2O	1.804
Na_2O	2.440
SO_3	3.214
Cr_2O_3	0.194
PbO	6.016
ZnO	25.290
MnO	2.452
CoO	0.240
CuO	0.454
Cl	3.622
LOI	6.450

The Waelz process starts with adding raw materials (EAF powder, anthracite coal, coke, and lime) to the rotary kiln. However, the rotary kiln temperature must be sufficient for chemical reactions before this process. When the rotary kiln system is commissioned after the planned shutdown (the period determined for periodic maintenance of the rotary kiln), natural gas is used for an average of 3 days to reach sufficient temperature inside the kiln. When the furnace reaches sufficient temperature, raw material is charged, and anthracite and coke coals are used to maintain this temperature until the next shutdown. For this temperature and heat balance, the furnace temperature should be approximately 1200°C.
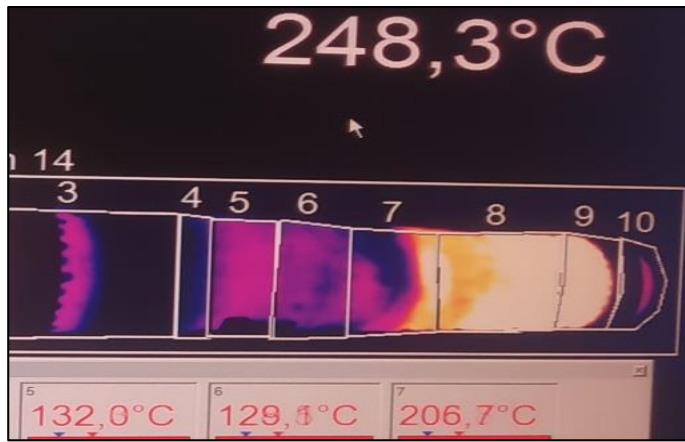
Figure 1. Rotary kiln slag zone outer sheet temperature.

When necessary, in addition to the coals, the flame pipe system is used to provide temperature support and manage the process. Samples are taken regularly from all raw materials to determine the ratio and content of raw materials to be charged into the furnace system. These samples are taken from belt spills or directly from stored raw materials. These raw materials are charged to the preheating zone of the furnace with the help of conveyors in the quantities determined as the final process. At this stage, the primary expectation from the preheating zone of the furnace is to prepare the raw materials for the reduction zone, where chemical reactions take place intensively. Figure 2 schematically shows the Waelz process rotary kiln zones. As a result of the chemical reactions in the furnace, one of the process outputs is slag with high iron content, and the other is zinc oxide. The negative suction system draws the evaporated zinc oxide into the dust chamber unit. The purpose of this unit is to separate the impurities in the zinc oxide drawn from the furnace by density difference. Zinc oxide turns into powder form in this unit. Powders with low zinc content (average 44% and below) are charged back to the rotary kiln, while powders with high zinc content (average above 44%) are sent to other stages of the process.
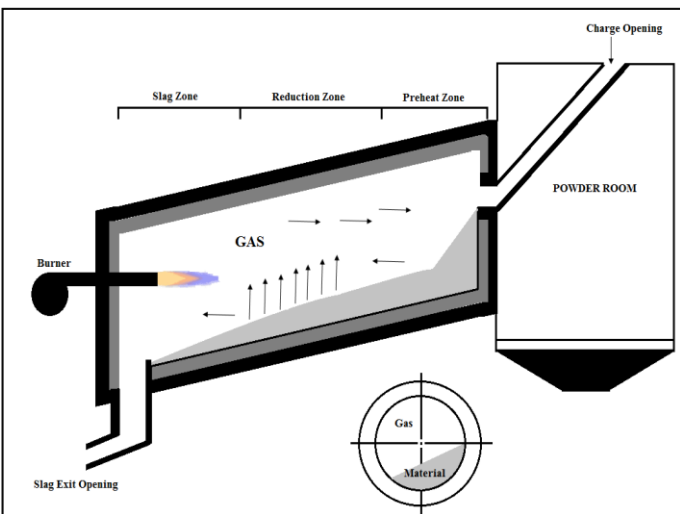

Figure 2. Waelz processes rotary kiln zones

Chemical analyses of raw materials charged to the furnace and furnace outputs are carried out simultaneously. Samples taken

from raw materials and outputs are subjected to specific tests and analyses in the factory's accredited laboratory. Since it is the output of the rotary kiln in terms of recovery and does not contribute to production, one of the main targets is to keep the amount of zinc in the slag below 1%. The higher the amount of zinc in the slag, the more zinc recovery in the rotary kiln cannot be done correctly, and the more zinc that can be obtained is lost in the slag. Failure to recover zinc properly can be caused by low zinc content in the raw material charged to the furnace, insufficient temperature and sufficient air for reactions, ring formations, and insufficient oxidation.

2.1. Dataset

In this study, the chemical analysis values of the materials used before the Waelz process and obtained as a result of the process of a zinc recovery company were used and turned into a dataset. These analysis values are the results of the samples given to the accredited laboratory. Therefore, this thesis verifies experimental studies with the machine learning method. The reliability of the numerical verification needs to be addressed in the thesis. Table 2 shows the raw materials charged to the rotary kiln and some values of the labeled data. In the slag, which is the output of the rotary kiln, the data with an average zinc value below 1% is labeled A, and the data with an average zinc value of 1% and above is labeled B. The actual dataset is summarized in Table 2, consisting of 29 columns.

Table 2. Dataset

Dataset	EAF powder (tons)	Lime (tons)	Coal (tons) (anthracite+coke)	A label	B label
Mean	398.26	37.73	142.87	0.63	1.73
Max	458	66	203	0.99	5.34
Min	71	4	102	0.23	1.01
Standard Deviation	40.59	10.57	10.41	0.18	0.77

2.2. Performance Metrics

Different performance metrics are used to measure the classification success rate of machine learning models. More than one machine learning method can be used for the data under study, and each algorithm's performance is measured separately to select the most successful algorithm. Table 3 shows the Confusion matrix used to measure classification performance. Performance metrics are determined according to the values obtained from this matrix. Metrics A and B were used in this study. A represents the average zinc value in slag below 1%, and B represents the average zinc value above 1%.

According to this matrix:

TP: Both positive in actual value and positive predicted value by the model.

TN: The value that is negative both in reality and in the model's prediction.

FP: The value that is negative in reality but predicted positively by the model.

FN: The value that is positive in reality but negative in the machine value.

Table 3. Confusion matrix

Confusion Matrix		Actual	
		Positive (A)	Negative (B)
Prediction	Positive (A)	TP	FP
	Negative (B)	FN	TN

Performance metrics used for classification:
Accuracy, precision, sensitivity, and F1 score. Their formulas are given in Eq. 1-4.
Accuracy is the number of correct predictions divided by the number of all predictions made.

$$Accuracy = (TP+TN)/(TP+TN+FN+FP) \qquad (1)$$

Precision refers to how many of the positively predicted samples were correctly predicted.

$$Certainty = TP/(TP+FP) \qquad (2)$$

Sensitivity indicates what proportion of values that should be positively predicted are correctly predicted.

$$Sensitivity = TP/(TP+FN) \qquad (3)$$

The F1 score is a combination of precision and sensitivity values and is often considered a metric to measure the performance of classification algorithms [9].

$$F1\ score=(2*Accuracy*Sensitivity)/(Certainty + Sensitivity) \qquad (4)$$

Cross-validation is used to determine the performance of the models. One of these methods is the k-layer cross-validation method. This method divides the entire dataset into "k" equal parts. In the k-layer cross-validation method, the training set to be used in the training process is first shuffled and divided into k subsets of equal size. This process is repeated k times, and the subset in each split is removed from the training dataset and used as the test set. This method tests the model's generalization ability, and overfitting problems are minimized [10]. Accuracy is checked by adding data to each partition one by one. This method uses each data point at least once as validation data. If the dataset is decided to be divided into ten parts, the value of k becomes 10. Ten pieces of validation data are created, and the process is repeated 10 times. In each repetition, these ratios are averaged. Accordingly, the higher the value of k, the higher the model's performance and the lower the model's error margin.

3. Results and discussions

This study used four different classification models and four different performance metrics on labeled data, and the best-performing classification models were identified. The dataset was divided into ten equal parts using the k-layer cross-validation method to determine the performance of the models. The results obtained are given in Table 4. When Table 4 and the ROC curves of the models are analyzed, the classification performance of the DT model is 100% at all K-fold values; the NB model is 97% at K-fold 2, the RF model is 100% at K-fold 10, and the SVM model is 94% at K-fold 2. (The performance values given as 100% are accepted as 100% since they are more than 99%).

According to Figure 3, at K-fold 10, the models show similar classification performance. However, when other criteria are considered, the DT model performs better in classification. In the other models, RF, NB, and SVM have the highest classification performance, ranging from highest to lowest.
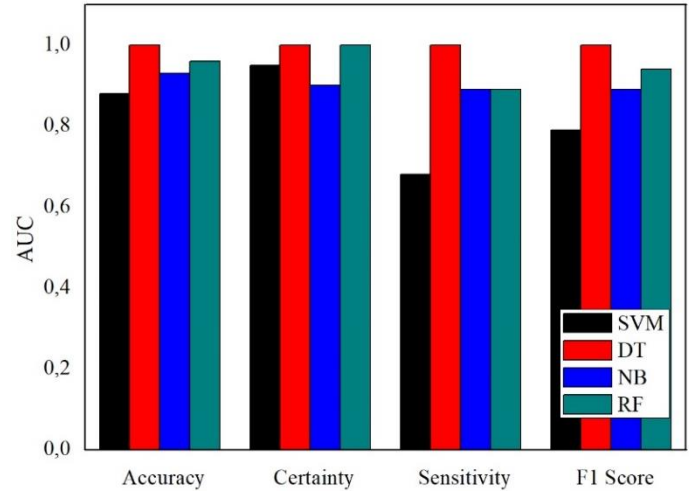

Figure 3. Classification performance comparison for k-fold 10
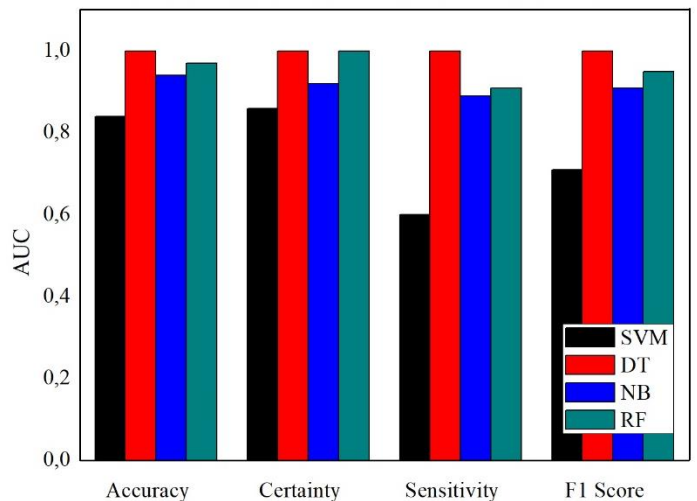

Figure 4. Classification performance comparison for K-fold 2

Considering Figure 4, the classification models perform close to each other according to the K-fold 2 value. However, when other criteria are considered, the DT model has a higher classification performance than the others. In the other models, RF, NB, and SVM have the highest classification performance, with the highest being the lowest, respectively. Figure 5-8 shows the ROC curves of the classification models.

Table 4. Results

K-fold	Performance Metrics	Models			
		SVM	DT	NB	RF
K-fold 2	Accuracy	0.84	1	0.94	0.97
	Certainty	0.86	1	0.92	1
	Sensitivity	0.6	1	0.89	0.91
	F1 Score	0.71	1	0.91	0.95
K-fold 3	Accuracy	0.87	1	0.93	0.97
	Certainty	0.92	1	0.9	1
	Sensitivity	0.67	1	0.89	0.91
	F1 Score	0.77	1	0.89	0.95
K-fold 4	Accuracy	0.88	1	0.94	0.96
	Certainty	0.94	1	0.90	1
	Sensitivity	0.67	1	0.90	0.88
	F1 Score	0.78	1	0.90	0.93
K-fold 5	Accuracy	0.88	1	0.94	0.97
	Certainty	0.94	1	0.91	1
	Sensitivity	0.68	1	0.90	0.90
	F1 Score	0.79	1	0.90	0.95
K-fold 6	Accuracy	0.88	1	0.92	0.98
	Certainty	0.95	1	0.89	1
	Sensitivity	0.66	1	0.89	0.94
	F1 Score	0.78	1	0.89	0.97
K-fold 7	Accuracy	0.88	1	0.92	0.97
	Certainty	0.96	1	0.89	1
	Sensitivity	0.67	1	0.89	0.91
	F1 Score	0.79	1	0.89	0.95
K-fold 8	Accuracy	0.87	1	0.91	0.96
	Certainty	0.93	1	0.87	1
	Sensitivity	0.65	1	0.88	0.90
	F1 Score	0.76	1	0.87	0.94
K-Fold 9	Accuracy	0.88	1	0.92	0.96
	Certainty	0.95	1	0.88	1
	Sensitivity	0.69	1	0.89	0.90
	F1 Score	0.79	1	0.88	0.95
K-fold 10	Accuracy	0.88	1	0.93	0.96
	Certainty	0.95	1	0.90	1
	Sensitivity	0.68	1	0.89	0.89
	F1 Score	0.79	1	0.89	0.94

ROC curves are one of the most valuable methods for evaluating and comparing the performance of classification models [11]. Figure 5 shows the ROC curve and the AUC area of the curve for the DT classification model. According to this curve, the DT classification model performed best at a K-fold ten value and an AUC value 1. K-fold ten means that the dataset is divided into ten equal parts. A high K-fold value in ROC curves is preferred because it can eliminate problems such as overfitting. An AUC value of 1 is considered as 100% performance. It means that a 100% correct classification is made for the values given for this model. This rate means that the model can distinguish the data well, and the accuracy rate is relatively high.
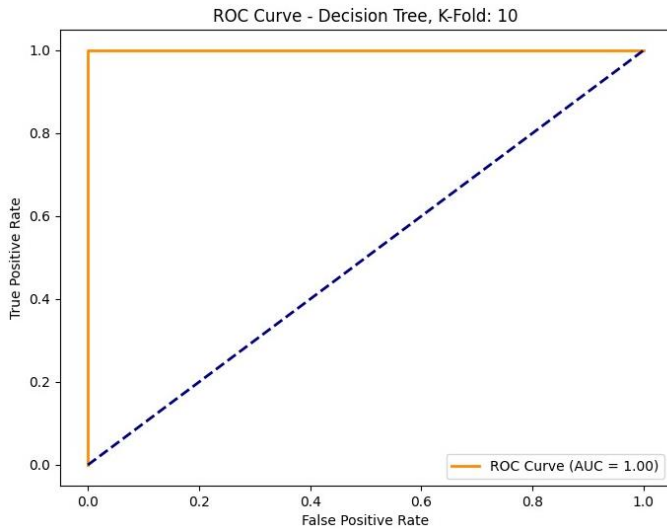
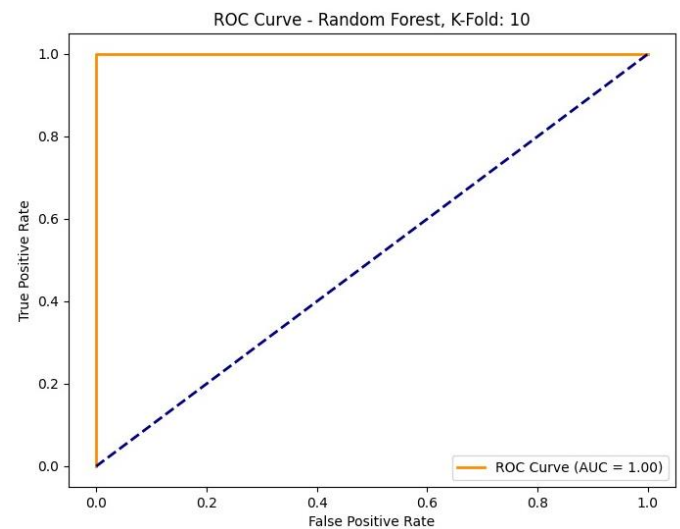Figure 5. ROC curve DT model

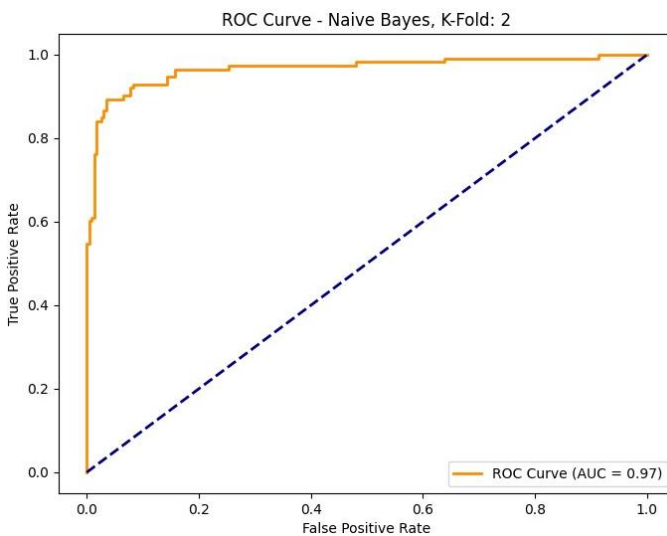

Figure 7. RF model of the ROC curve
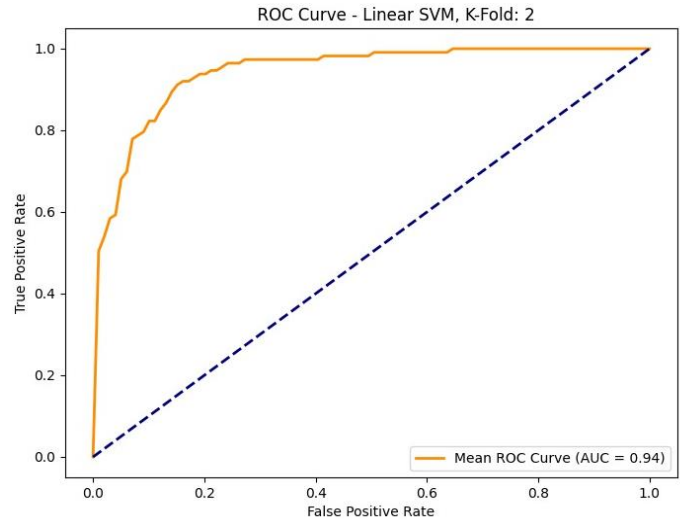

Figure 6. ROC curve NB model

Figure 8. ROC curve SVM model

Figure 6 shows the ROC curve and AUC area for the NB classification model. According to this curve, the NB classification model performed best at K-fold 2. The AUC value is 0.97. The higher the AUC value, the higher the classification success of the model [10]. For this reason, in the ROC curve divided into ten equal parts, the K-fold value closest to AUC 1 was taken as the basis. In this case, the only value close to AUC 1, i.e., 100%, is the K-fold 2 value. As a result of this curve, the NB model made 97% correct classification.

The ROC curve shown in Figure 7 was used to evaluate the performance of the RF classification model. The area under the curve, AUC, takes a value between 0 and 1. A value of 0.5 is equivalent to random guessing, while 1 indicates perfect prediction [12]. According to the ROC curve in Figure 7, the RF classification model gave the highest accuracy value with K-fold 10. The AUC value is 1. This indicates 100% correct classification and that the model works very well.

Figure 8 shows the ROC curve and the AUC area of the curve for the SVM classification model. If the AUC area is between 0.5 and 0.7, it indicates poor performance, between 0.7 and 0.9 indicates moderate performance, and above 0.9 indicates good performance of the model [13]. The best performance for the SVM classification model was obtained at K-fold 2, and the AUC value was 0.94. This value indicates that the model performs 94% correct classification. This shows that the model learns the dataset effectively and correctly classifies it.

4. Conclusion

This study explored the application of machine learning techniques to classify zinc quality in slag generated through the Waelz process, addressing a key challenge in the iron and steel industry. Among the algorithms evaluated, the Decision Tree (DT) model demonstrated exceptional performance, achieving

100% accuracy, precision, sensitivity, and F1 score, establishing itself as a highly reliable tool for quality control in zinc recovery. Other models, such as Random Forest (RF) and Naive Bayes (NB), also delivered high accuracy, highlighting the potential of machine learning in this domain. The findings of this study contribute significantly to advancing automated quality control in metallurgical processes by offering accurate and efficient classification models. Furthermore, integrating these models into real-time monitoring systems has the potential to optimize zinc recovery operations, improve resource efficiency, and support sustainable waste management practices.

Based on the experimental results and analyses, the following conclusions can be drawn:

- The proposed machine learning approach successfully classified zinc content in Waelz process slag, with the Decision Tree (DT) algorithm achieving 100.0% accuracy, precision, sensitivity, and F1 score across all validation sets.
- Cross-validation results demonstrated that the DT and Random Forest (RF) algorithms outperformed other tested methods, with RF achieving 96.0-98.0% accuracy and 100.0% precision. This confirms the robustness and reliability of tree-based methods for this classification task.
- The developed classification system enables rapid assessment of slag quality, thereby potentially optimizing the zinc recovery process through real-time monitoring and control.
- Chemical composition analysis of input materials combined with the classification model provides predictive insights for process optimization, potentially reducing operational variability and improving resource efficiency.
- The methodology demonstrates potential for industrial implementation, offering a data-driven approach to quality control in metallurgical processes.

Future Research Directions:

- Implementation of real-time monitoring systems
- Investigation of deep learning approaches for process optimization
- Development of integrated control systems based on classification outputs
- Extension of the methodology to similar metallurgical processes

This research contributes to the industrial application of machine learning in metallurgical processes, providing a systematic approach for zinc recovery optimization through accurate quality classification.

Acknowledgment

Conflict of Interest Statement

The authors declare that there is no conflict of interest in the study.

CRediT Author Statement

Didem Özcan: Conceptualization, Data curation, **M. Kürşat Karaoğlan:** Conceptualization, Data curation, Original draft writing, Validation, **Mehmet Çelik:** Original draft writing, Validation, Formal analysis, Supervision

References

1. Mudd, G. M., Jowitt, S.M., & Werner, T. T. (2017). The world's lead-zinc mineral resources: Scarcity, data, issues and opportunities. Ore Geology Reviews, 80, 1160–1190.
2. Avachat, H., Sabnavis, M., & Jagasheth, U. H. (2018). Zinc industry: the unsung metal of the economy-industry research report. CARE Ratings: Professional Risk Opinion, 1-11
3. Ng, K. S., Head, I., Premier, G. C., Scott, K., Yu, E., Lloyd, J., & Sadhukhan, J. (2016). A multilevel sustainability analysis of zinc recovery from wastes. Resources, Conservation and Recycling, 113, 88–105.
4. Goodwin, F.E. (2017). Current status anf future expectations for the zinc market. International Zinc Association for Presentation at Inter-ZAC 2017, Toronto.
5. Jia, Y., Zhang, T., Zhai, Y., Bai, Y., Ren, K., Shen, X., Cheng, Z., Zhou, X. & Hong, J. (2022). Exploring the potential health and ecological damage of lead–zinc production activities in China: A life cycle assessment perspective. Journal of Cleaner Production, 381(1), 135–218.
6. Shawabkeh, R. A. (2010). Hydrometallurgical extraction of zinc from Jordanian electric arc furnace dust. Hydrometallurgy, 104(1), 61–65.
7. Oustadakis, P., Tsakiridis, P. E., Katsiapi, A. & Agatzini-Leonardou, S. (2010). Hydrometallurgical process for zinc recovery from electric arc furnace dust (EAFD): Part I: Characterization and leaching by diluted sulphuric acid. Journal of Hazardous Materials, 179(1-3), 1-7.
8. Özcan, D. (2024). Classification and regression analysis of zinc recovery in rotary kilns using machine learning. Published Master's Thesis, Karabük Üniversitesi, Karabük.
9. Polatgil, M. (2023). Investigation of the effects of data scaling and imputation of missing data approaches on the success of machine learning methods. Duzce University Journal of Science & Technology, 11, 78–88.
10. Başer, B. Ö., Yangın, M., & Sarıdaş, E. S. (2021). Classification of diabetes mellitus with machine learning techniques. Süleyman Demirel University Journal of Natural and Applied Sciences, 25(1), 112–120.
11. Tomak, L., & Bek, Y. (2010). The analysis of receiver operating characteristic curve and comparison of the areas under the curve. Journal of Experimental and Clinical Medicine, 27(2), 58–65.
12. Yiğit, P. (2011). Yapay sinir ağları ve kredi taleplerinin değerlendirilmesi üzerine bir uygulama. Published Master's Thesis, İstanbul Üniversitesi, İstanbul.
13. Pintea, S., & Moldovan, R. (2009). The receiver-operating characteristic(roc) analysis: Fundamentals and applications in clinical psychology. Journal of Cognitive and Behavioral Psychotherapies, 9(1), 49–66.